Technical Design Report of the Forward Preshower Detector for the DØ Upgrade

A. Gordeev, J. Kotcher, M. Xiong Liu, P. Yamin
Brookhaven National Laboratory
Upton, New York 11973

M. Bhattacharjee, D. Chakraborty, P. Grannis, A. Lucotte, A. Patwa,
M. Rijssenbeek, D. Shpakov, J. Steffens, A. Talalevskii
State University of New York at Stony Brook
Stony Brook, New York 11794

M. Chung
University of Illinois at Chicago
Chicago, Illinois 60607

May 18, 1998

Abstract

The DØ Forward Preshower Detector, one of four inner-tracking subdetectors in the DØ Upgrade, is designed to enhance electron identification in the forward pseudorapidity region ($1.5 < |\eta| < 2.5$). The scintillator-based detector will provide particle discrimination by exploiting the difference between the energy loss mechanisms of electrons (and photons) and those of the dominant backgrounds. The increase in acceptance for both high- and low-p_T electrons and photons that the detector will provide is expected to measurably extend the physics reach for a variety of processes central to the physics program at the upgraded Tevatron. This paper contains a detailed description of the technical design of the detector. It is being submitted to the DØ Collaboration for review before final construction of the detector begins in early 1998.

Contents

1 Introduction

The DØ Forward Preshower Detector (FPS) is intended to enhance electron identification in the forward pseudorapidity region ($1.5 < |\eta| < 2.5$) in order to fully capitalize on the physics opportunities offered at the upgraded Tevatron. This document is a comprehensive review of the technical design of the detector. The physics motivation and conceptual design, detector design and construction, detector readout and calibration, and project organization are all discussed, in varying detail, in this report.

This document is intended to provide a sufficient amount of information to provide the basis for a review of the proposed detector. Anticipating any changes that may need to be implemented after this review, and in order to give a complete picture of the design to the committee, we have tried wherever possible to include a description of the basis for various design decisions, so that documentation exists to refer to as the design is finalized.

We acknowledge the significant amount of R&D done by the Scintillating Fiber Tracker (CFT) and Central Preshower (CPS) groups on the development of the scintillator extrusion and VLPC readout scheme that we have chosen to adapt for our use. In the interest of limiting the scope (and hence the length) of this report, we concentrate here on those aspects of these techniques that are unique to the Forward Preshower, and direct the reader toward the many already-existing write-ups and publications for descriptions of the more generic groundwork on which the detector is based.

The FPS group welcomes comments from our collaborators on any and all aspects of this document. Please feel free to contact any of the authors with your questions or concerns.

1.1 Physics Motivation

The Central and Forward Preshowers serve to enhance the electron and photon identification of the DØ detector and to increase the rejection of fakes of QCD origin; these consist mostly of jets which fragment with a leading energetic π^0 or a charged pion with subsequent early charge exchange. In addition, the Central Preshower (CPS), and parts of the Forward Preshower (FPS) sample energy after the solenoid coil, and thus serve as an additional calorimetric sample measurement.

The FPS collects information both before and after $2X_0$ of Pb radiator (or, at lower pseudorapidity, the magnet coil) and is able to measure MIPs upstream of the Pb radiator, and EM showers downstream. The energy resolution for showers is expected to be of the order of 20%. Coverage extends from a pseudorapidity $|\eta|$ of 1.5 up to 2.5, with the region between 1.5 and 1.65 lying in the shadow of the solenoid end wall and therefore equipped only with a shower layer. Extruded scintillator strips of triangular cross section (equilateral tringles of ≈ 6.0 mm on a side) are arranged in u and v stereo layers covering $22.5°$ sectors.

Several notes describe the early tests of mechanical and material details of the DØ preshower concept [3, 4], and described the concept and physics motivation of the Forward Preshower [5, 6]. The physics contribution of the FPS is twofold: at the trigger level, and in the offline reconstruction.

At the trigger level, the inclusion of the FPS at Level 1 will reduce backgrounds from QCD in the FPS region by a factor of between 2 and 4 (depending on p_T), thereby reducing the trigger rate to Level 2 or allowing lower trigger p_T thresholds. Upon spatially matching the FPS cluster to electromagnetic energy deposited in the end calorimeter – which is only possible at Level 2 – additional factors of 2 in rejection are expected. These reduction factors, relative to a calorimeter-only trigger, have been observed in early simulations [6] where scintillator strips with a square cross section of 5 mm arranged in a disk-like geometry were assumed. These numbers are the process of being confirmed by simulations discussed in this report, in which the current FPS design is implemented.

In all cases foreseen, the FPS trigger will be used in conjunction with calorimeter trigger at Level 1, and in combination with tracking and calorimeter triggers at the higher levels. Processes of particular interest are those with few other trigger handles and those where backgrounds are high – *e.g.*, semi-electronic B decays, and low-p_T electron or photon processes in general. In the case of semi-electronic B decays, a good fraction – about half – have an electron that is separated by more than 0.1 in r-ϕ from the associated c-jet. Such configurations can be triggered by using the low-p_T EM calorimeter trigger in conjunction with an associated FPS trigger. We note that B production at the Tevatron has a substantial cross section in the region of the FPS. Low-p_T electrons and photons are of interest in the study of Drell-Yan, J/ψ, Υ, and χ-state production, and in the production of W and Z bosons with associated jets. In addition, one of the more distinctive signals of Supersymmetry during Run II will be the tri-lepton final state resulting from gaugino pair production. At least one of the three final state leptons in this signature is often quite soft ($p_T \geq 5$ GeV) and produced at a forward pseudorapidity [6]. Any additional improvements for triggering on or reconstructing low-p_T electrons produced at high $|\eta|$ will provide an important capability in exploiting this important SUSY channel.

Rejection of converted photons from π^0s is non-trivial with the MIP layer of the FPS because of the uncertainty in the conversion rate upstream of the FPS introduced by the tails of the dE/dx distribution, and the spatial resolution that is required, particularly at high-p_T. Some discrimination, dependent on the conversion point, may be obtained from the lateral shape of the shower after the radiator; this is still under study but most likely will need the detailed information only available at Level 2 or 3. Additional rejection will come from isolation requirements that can be applied at the trigger levels. At Level 3 the separation will be enhanced by whatever tracking information can be extracted from both the fiber and silicon systems.

For "easy" signals such as electrons from W (and Z) bosons, the preshowers are expected to contribute the necessary ($\approx \times 2$) rejection of backgrounds at the on-line stage that we anticipate will be necessary in order to implement a non-prescaled W trigger. One could also envisage the use of the preshowers in the collection of various prescaled control samples where the tight electron trigger criteria on calorimeter and track match are relaxed in order to study their inefficiency and turn-on behavior. With increased signal statistics and the subsequent need for lowering the W mass resolution systematics with the goal of measuring the W mass in Run II to 40 MeV or better, such control samples will become progressively more important and will have to provide even more detailed information; *e.g.*, the correlations between cuts. Similarly, energy calibration samples will require more statistics, and preshower triggers may provide additional purity at low energy.

At the off-line stage, a more sophisticated preshower signal analysis will provide additional rejection of backgrounds in physics topics listed above. It will allow the lowering of the p_T threshold of the photon in the study of tri-linear intermediate vector boson couplings. As was demonstrated in Run 1, direct photons are also critical in the determination of the jet energy scale – lowering the photon p_T trigger threshold will allow us to extend the kinematic range of the jet calibration. The increased rapidity coverage for photons has been shown to be quite important in identifying and characterizing the predicted "radiation zero" in the W-γ coupling. It will improve the separation of photons from QCD and electron backgrounds in the study of single and di-photon QCD production. Of course, tracking information is crucial here, as is good quantitative knowledge of upstream material and its distribution.

For relatively rare signals (*e.g.*, top), and for searches for signals with associated isolated electrons or photons (*e.g.*, W', Z'), preshower confirmation provides additional confidence in electron identification and background subtractions.

For precision measurements – *e.g.*, the mass determination of the W boson, which depends crucially on the accuracy of the electron energy determination – the preshowers will provide an extra energy sampling measurement, which is strongly correlated with energy lost in the solenoid, radiator, and cryostat walls. The additional acceptance in $|\eta|$ will enhance our ability to distinguish between different parton distribution functions; limits in our understanding of proton structure may very well be one of the primary contributions to the error on the W mass in Run 2. The forward coverage provided by the FPS will also enhance the measurement of the forward-backward asymmetry in $Z \to ee$ decays, which will be used to extract a measurement of $\sin^2\theta_W$ in the light quark sector to an expected 0.001 or better.

1.2 Conceptual Design

The higher luminosities during Run 2 will diminish our ability to trigger on and identify electrons and photons using the calorimetry alone. The FPS is intended to aid us in more fully exploiting the hermetic electromagnetic (EM) coverage of the DØ calorimeters, and hence many of the physics processes of interest during Run 2. Such full acceptance for leptons and photons has always been an emblematic strength of the DØ design.

One FPS detector will be mounted on each of the heads of the end calorimeter cryostats, shadowing as much of the forward electromagnetic calorimetry as possible. The primary practical restrictions that limit the coverage to $1.5 < |\eta| < 2.5$ are the presence of other subdetectors at the inner (Level 0) and outer (Inter-Cryostat Detector) radii of the FPS. There is only partial electromagnetic coverage in the end calorimeter for $|\eta| < 1.5$; additional FPS coverage here would offer only marginal gains at best. It was shown during Run 1 that electron identification of any kind below $|\eta| > 2.5$ is, for all intents and purposes, impossible – and the situation will not get any better during Run 2. We have therefore developed a design that covers this known region of interest.

The FPS detectors will consist of two layers of thin, finely-segmented active elements that will provide charged particle detection. Two radiation lengths ($2X_0$) of lead absorber, intended to induce identifiable showers characteristic of electromagnetically-interacting particles (*i.e.*, electrons and photons) that traverse it, will be sandwiched between them. All charged particles that traverse the forward active detector – that closest to the interaction point – will register a hit in this layer, and therefore a space point. Electrons will shower readily in the lead, generating a collimated cluster of energy in the rear layer in a location consistent with the forward MIP deposit. Charged pions and muons will tend not to shower in the absorber, and therefore will produce minimum-ionizing tracks both before and after the lead. Photons, whether directly produced or resulting from π^0 decay, will be identified by the presence of an electromagnetic cluster behind the absorber, and the absence of a spatially-matched forward hit. These characteristic energy deposits of the signal and background provide the basis for particle identification with the FPS.

The dominant backgrounds for the electron signature are photons (from π^0 decays) that convert before the FPS, and hadrons that either shower in the converter or overlap spatially with a photon. It is therefore desirable to limit the amount of material upstream of the detector, in order to limit the photon conversion probability. The thickness of the absorber in nuclear interaction lengths (λ_I) must also be contained, in order to limit the likelihood that charged hadrons will shower in the converter, and hence mimic the electron signature.

Tracks that originate from the center of the detector have to traverse the beam pipe, the silicon vertex detector (SVX), and part of the CFT before reaching the FPS. Tracks with $|\eta| < 1.65$ also have to traverse the cryostat and coil of the superconducting magnet. The amount of material traversed in radiation lengths and nuclear interaction lengths for tracks at different pseudorapidities η [2] is shown in Fig. 1. Outside the region of the magnet coil ($|\eta| > 1.65$), the amount of upstream material is minimal. The coil itself, however, introduces as much as $3X_0$ ($0.7\lambda_I$) at $|\eta| \approx 1.5$. We note that the additional material due to cables, fibers, and other inner-tracking services are not included in these plots, and that they therefore represent a best-case scenario. The full simulation awaits a complete description of the inner detectors in the DØ Upgrade Monte Carlo program DOGSTAR.

The basic features of the proposed geometry of the detector are shown in Fig. 2. We have opted for a 16-wedge design, with the active volume of the detector in each wedge segmented into u and v stereo strips. Each of the 16 ϕ-wedges will subtend $22.5°$, and will consist of a u and v stereo layer both before and after the lead, allowing the determination of a space point in each plane of strips. The u strips will be perpendicular to one radial edge of the ϕ sector, and the v strips perpendicular to the opposite edge, yielding a $22.5°$ crossing angle between them. The set of sectors furthest from (closest to) the interaction point in z will subtend the region $1.5 < |\eta| < 2.5$ ($1.65 < |\eta| < 2.5$). The large amount of material in the magnet coil in the region $1.5 < |\eta| < 1.65$, which will readily induce showers, would make a MIP determination in the forward layers of no value here. The presence of the coil also obviates the need for lead absorber in this region, which has led to our decision to limit the radial extent of the converter as shown.

A detailed series of Monte Carlo studies has been performed for the geometry shown in Fig. 2, using 5 mm scintillator strips [6]. We direct the reader to this reference for a complete discussion

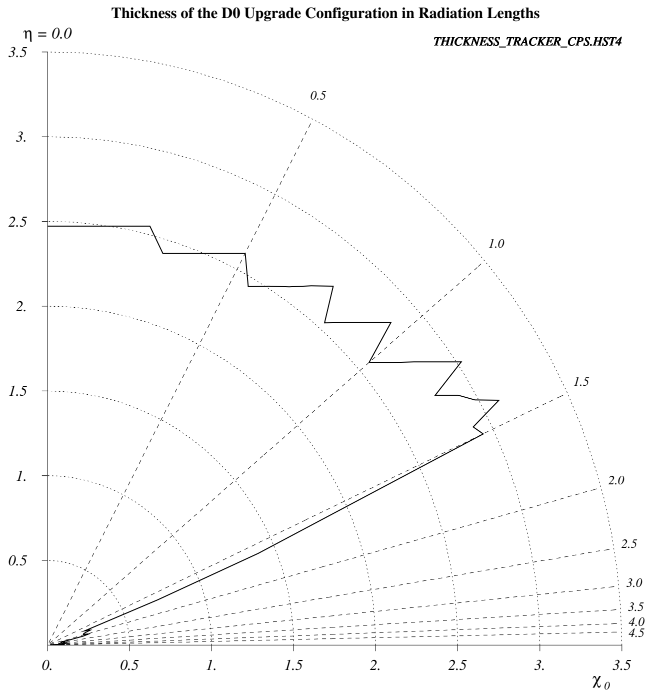

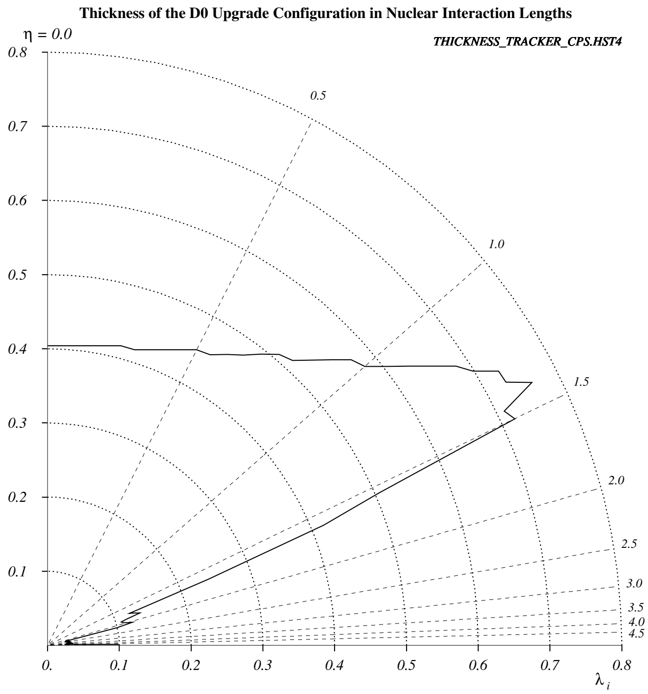

Figure 1: Amount of material traversed before the FPS by tracks originating at the center of the detector in radiation lengths (top) and nuclear interaction lengths (bottom). Cables and services from the inner detectors are not included.

of the expected trigger capabilities of the device, as well as some preliminary work on possible use of FPS information in the offline reconstruction for Run 2. This work has demonstrated that the proposed geometry – 16 ϕ wedges per side, and $\approx$ 5-mm-wide strips – constitutes a good balance between performance and channel count (or cost). We have used these numbers as a benchmark during the development of a final detector design. We discuss this design in the following sections.

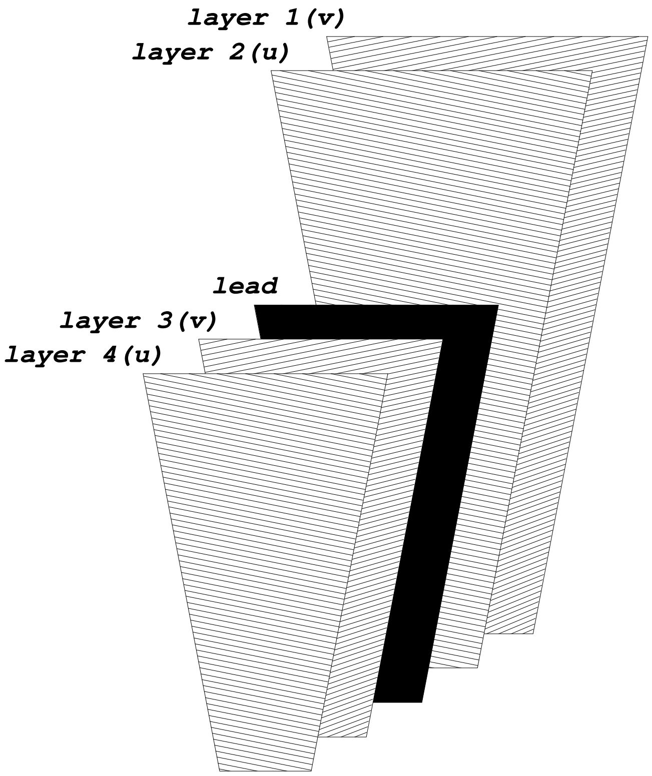

Figure 2: Schematic picture of one azimuthal wedge. The lines represent the scintillator strips.

2 Detector Design and Construction

We describe below the considerations that have motivated our technology choice, and follow this with a descriptive overview of the design of the detector. A more detailed discussion of the various parts of the detector and their construction are described in the subsequent subsections. For ease of identification throughout this document, we number the four FPS layers successively from 1 to 4, with the layer furthest from (closest to) the interaction point corresponding to Layer 1 (4).

2.1 Technology Choice

There are a number of constraints that have had a defining impact on the final design of the FPS. Electron identification is enhanced in a device that is highly segmented. Since the cost mounts proportionally to the channel count, a suitably inexpensive readout system is also called for. Triggering considerations demand that the technology be suitably fast as well. In addition, the preshower is designed not only to resolve minimum ionizing signals above the noise in order to do the appropriate track identification, but to identify and characterize the comparatively large signals that are the signature of electron showers. The shower energy typically constitutes $\approx$1-5 % of the electron energy for leptonic decays of interest at TeV II. In order to ensure that the high-resolution capability of the forward electromagnetic calorimeters is not compromised in any way, we intend to add the energy measured in the preshower to that measured in the corresponding calorimeter tower(s) for electron candidates. This dictates that the FPS readout must be linear over a fairly wide range of energies, and that it must also lend itself to an absolute energy calibration of some acceptable level of accuracy.

Another more practical – but no less significant – concern is the severe spatial constraints that exist in the region between the central and end cryostats (see Fig. 3). All of the cables and services from the inner silicon and fiber tracking detectors, which together consist of a total of about 900,000 readout channels, will necessarily be routed through this region before descending to the platform below the detector. In order to make the most effective use of the limited available space, a compact detector is essential. Such constraints also strongly suggest that the detector be pliable enough to conform to the spherically-shaped end cryostat inner head. The technology must therefore lend itself to such reshaping.

We have opted to pursue the same technology for the FPS as that which is being used for the CPS [3, 4, 8]: scintillator strips with embedded wavelength-shifting (WLS) fibers, read out by visible light photon counters (VLPCs). In addition to satisfying most of the features outlined above, this choice saves the cost and time involved in the R&D that would be necessary to develop a different technology. We will be able to use identical front-end and trigger electronics for both detectors. The many design considerations common to the two detectors, such as light yield requirements, scintillator properties and fabrication, and detector assembly techniques, will allow us to benefit from the considerable amount of research and development that has gone into the design of the CPS. We expect to base many additional components of the design of the FPS, such as connector design, detector calibration and temperature monitoring, fiber bundling, and scintillator extrusion on CPS R&D, introducing appropriate modifications as they are warranted. We refer the reader to [8, 19, 20, 21, 24, 7], and references therein, for more details on the CPS design and readout, specifics of the VLPCs, and other related details.

We intend to use lead as the absorber material that will be sandwiched between the active elements of the detector. Although an additional ≈ 4 mm in detector thickness could be gained by using tungsten or uranium, the cost and complications related to the handling, fabrication and/or machining of these materials makes their use here impractical. The intrinsic compactness of a lead/scintillator detector, coupled with the ease with which it can be made to conform to the endcap cryostat shells, also facilitates the construction of the detector in the available space.

As in the CPS, each scintillator layer will consist of two nested layers of triangular-shaped scintillator strips. This nested design eliminates dead regions resulting from projective cracks and has been shown to give position resolution much better than the inter-strip separation when light-sharing information between adjacent strips is used. In practice, a position resolution of ≈ 600 μm has been achieved with cosmic ray muons using strips with a base length of 9 mm and a height of 4.5 mm [8].

The strip dimensions are driven primarily by the expected occupancies, the desired position resolution, the light yield required, and detector cost. Detailed simulation studies, aimed at determining the optimal strip dimensions for the FPS, are currently underway. At present, we see no viable physics or other reason, however, to deviate from using the same strip dimensions as those that were used for the CPS detector. This choice also has the benefit of neatly mapping an appropriate number of channels into the desired Level 1 trigger sector. More will be said about this issue in later sections.

2.2 Detector and Signal-Routing Overview

The Forward Preshower is composed of trapezoidally-shaped ϕ-modules that are housed in disk-shaped aluminum support structures that mount on the faces of the end calorimeter cryostats. There are two such structures – both the north and the south end cryostats are covered – that span the pseudorapidity range $1.5 < |\eta| < 2.5$ (see Fig. 3). Each of the structures consist of four layers of modules. The coverage in pseudorapidity is meant to, within practical considerations, match the usable active region of the end electromagetic calorimeter modules. All of the elements of the entire structure – modules plus support housing – will be bent to conform to the spherical shape of the end calorimeter cryostat heads.

As mentioned above, the ϕ-wedges are modules made of extruded scintillator strips of triangular cross section, with embedded wavelength-shifting fibers. Each module consists of two layers of nested strips that form a crossing ("stereo") angle of 22.5 degrees with respect to one another, and so provide a space point (x,y,z or r,ϕ,z). The two stereo layers (u and v) are perpendicular to either edge of a module, and form an angle of 78.75 degrees with the vertical bisector of a module. The blue light emitted by each optically isolated scintillator strip is absorbed (maximum at 430

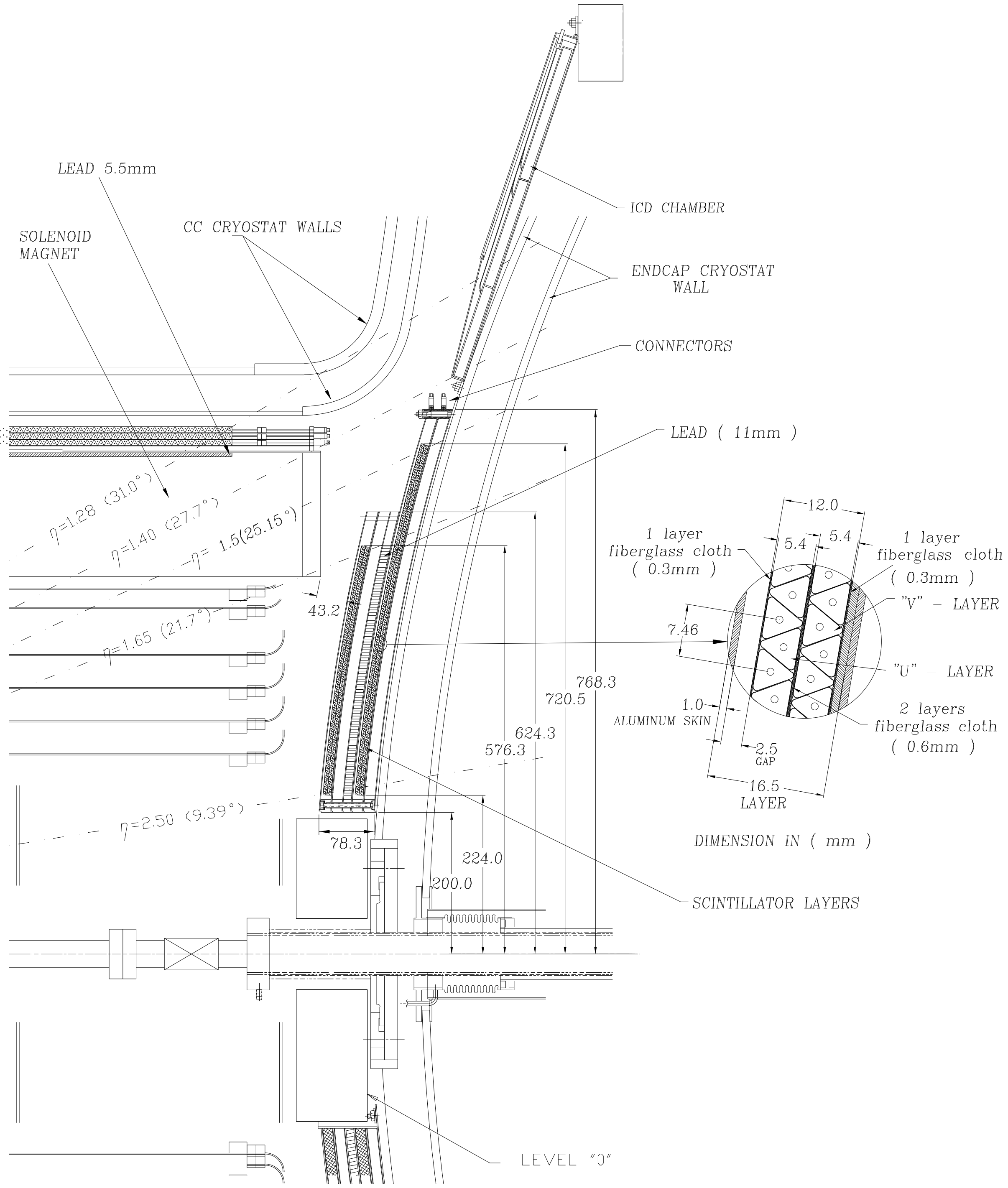

Figure 3: One-quarter r-z view of the proposed Forward Preshower Detector.

nm) in a coaxially located wavelength shifting fiber, and re-emitted in the green (510 nm). The signal is propagated via clear fiber connections to remote Visible Light Photon Counters (VLPCs). The VLPCs have a high quantum efficiency ($\simeq$ 80% at 530 nm) and high gain ($\simeq 10^4$), resulting in an expected light yield of approximately 15 photoelectrons per MIP. The detector system yields a position resolution better than 1 mm in the radial coordinate r, and better than 3 mm in r-ϕ, depending on deposited energy and strip-to-strip calibration.

The four structurally distinct layers that comprise the FPS will each consist of eight modules (see Fig. 4). Each module in a layer will subtend 22.5° in ϕ (1/16 of the full 2π ϕ coverage), covering the central half of the area subtended by adjacent 45° ϕ-sections. A complementary layer, which nests adjacent to it in z, will contain a set of modules that cover the alternate 22.5° ϕ sections. The full 2π angular region in ϕ is therefore covered by a pair of adjacent layers, which contain modules that are positioned in staggered locations in ϕ.

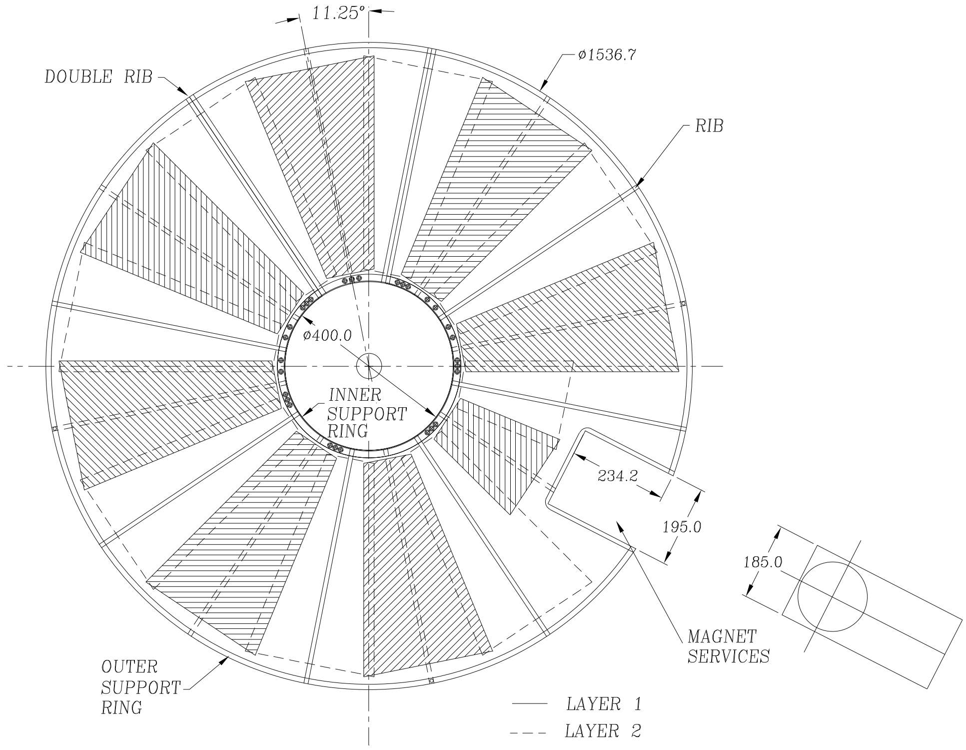

Figure 4: Schematic view in r-ϕ of the inner layer (Layer 1) of the FPS. The dotted lines show the outline of the layer that nests adjacent to it in z. Each layer is supported by a support frame consisting of radial ribs and in inner and outer ring, as shown.

A given module is a structurally independent unit which consists of both a u and v sublayer.

Each module subtends the central $\pm 11.25°$ of the ϕ-wedge on which it is centered, plus an additional 12.7 mm on either side. This defines the active region (in ϕ) of each modular unit. The 12.7 mm additional active area provides an overlap region of coverage between the adjacent staggered modules, in order to eliminate projective cracks. It results in one inch ($\pm 1/2''$) of overlap between adjacent modules. The staggering in z of the module position is necessary to allow the exiting and routing of the WLS fibers from the scintillator ends to the connectors at the outer radius.

The central hole in each triangular scintillator strip shown in the inset of Fig. 3 accommodates a WLS fiber, which runs axially along the scintillator strip to the edge of the module. The fibers then run radially to the perimeter of the detector. The support ribs in a given layer lie along constant lines in ϕ, between the modules, at 45° ϕ intervals. The additional space between the ribs and the modules provide space and mechanical support for routing the WLS fibers to the outer radius. Space restrictions, along with installation considerations, require that the connectors be mounted at the periphery of the detector.

Connectors that couple the emerging WLS fiber to the clear fiber waveguide are mounted to brackets that are fixed to the outer support rings of the detector (see Fig. 22 in Sec. 3.3.2). The clear fiber is then brought around the circumference of the FPS and down to the platform below the detector, where the VLPCs will be housed. Sixteen fibers will be routed to each connector at the detector end.

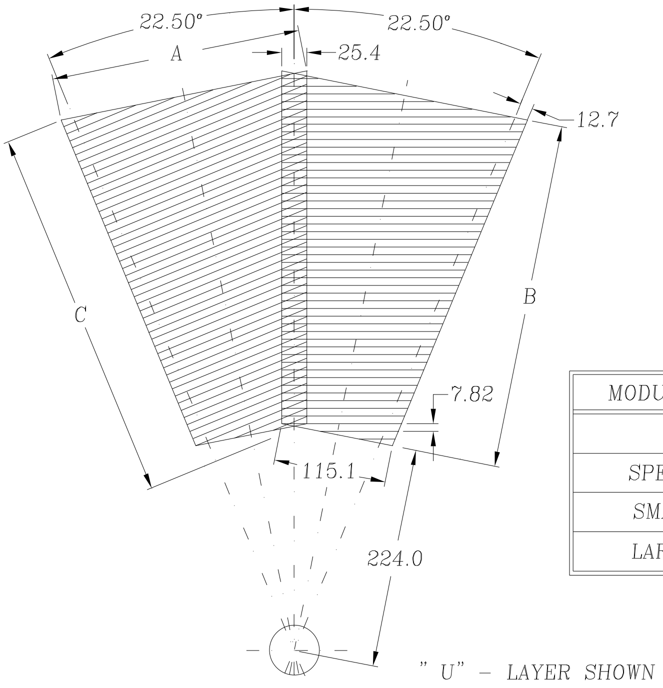

MODULE TYPE	DIMENSION (in mm)		
	A	B	C
SPECIAL	214.9	250.9	278.3
SMALL	255.3	352.3	381.7
LARGE	312.6	496.6	528.7

Figure 5: Generic drawing of two FPS modules, with dimensions given in chart on right.

Particles produced at the interaction point with $|\eta| < 1.65$ must traverse the magnet coil, which represents as much as $3X_0$ upstream of the FPS. Since showers will easily develop in the material upstream of the MIP-detecting layers throughout most of the region $1.5 < |\eta| < 1.65$, the discriminating power that the forward modules are designed to provide is severely hampered in this pseudorapidity range. The detector is therefore logically segmented into two distinct regions in pseudorapidity, defined primarily by the presence or absence of the magnet coil that shadows it: the layers behind (*i.e.*, downstream of) the lead can be used to provide shower information throughout the entire range of pseudorapidity, and therefore cover the full available range of $1.5 < |\eta| < 2.5$. The layers in front (*i.e.*, upstream) of the absorber are limited to that pseudorapidity range in which there is no coil upstream: $1.65 < |\eta| < 2.5$. Similar considerations dictate that the lead cover only the region $1.65 < |\eta| < 2.5$: the presence of the solenoid obviates the need for any additional absorber material in the region $1.5 < |\eta| < 1.65$. The lead will be 11 mm, or $2X_0$, in thickness.

For each side of the detector (north and south), there is a limited ϕ-slice for which the structural ϕ-symmetry of the design is broken. Modifications in two 22.5° sectors are required in order to allow the coexistence of the FPS and the magnet support services at $\phi = 332.946°$, or 27.054° below the $+x$-axis in the DØ coordinate system (see Sec. 2.1 below). (The channels occupy the same angular ϕ-slice on both sides – north and south – of the detector.) The presence of these magnet service channels requires that the detector be truncated in this region, resulting in four "special" modules per side that covering only $1.8 < |\eta| < 2.5$. The adaptation of the detector in this region is shown in Fig. 4. The dimensions for each of the module types – large, small, and "special" – are shown in Fig. 5.

We present in a condensed form in Tables 1 and 2 a list of some of the design parameters of the detector and modules, respectively. The reader is directed to Fig. 8 for a discussion of the scintillator dimensions. A more complete description of the detector is contained in the following sections.

2.3 Module Construction

The development of the FPS test beam prototype assembly during October-May, 1997, provided us with with the opportunity to confront the logistics of the module design and construction in a timely way. We begin the more detailed discussion of the FPS with a presentation of the active volume of the detector, and present in this subsection the module construction scheme that we propose. We expect that most of the details will remain unchanged before final construction begins. For discussions of the scintillator extrusions and wrapping procedures, we refer the reader to previous reports containing descriptions of these techniques [8].

2.3.1 Aluminum "Template" Domes

Aluminum domes, cut to the radius of the end calorimeter cryostat head, will be cut on a digitally programmable cutting machine in the Central Shop at Brookhaven. These domes provide the

Item	Description
Number of detectors	2 (one on each end cryostat)
Inner (outer) radius (mm)	200 (1536.6)
Active material	nested scintillator strips of triangular cross section
Readout	WLS fibers, clear waveguide, VLPCs, SVXII
ϕ-segmentation	32 $\times$ 2 trapezoidal ϕ-wedges
z-segmentation	4 (two u,v) layers per side
Strip geometry	22.5° stereo
Total channel count	2 $\times$ 7,184 = 14,368
Absorber	2X_0 lead
η-coverage of absorber	1.65< $\|\eta\|$ <2.5
Weight	222 kg (495 lbs.) per side

Table 1: Some detector parameters of the FPS.

	Large Module	Small Module	"Special" Module
η-coverage	1.50< $\|\eta\|$ <2.5	1.65< $\|\eta\|$ <2.5	1.80< $\|\eta\|$ <2.5
ϕ-coverage	$\pm(11.25° + 12.7$ mm)	$\pm(11.25° + 12.7$ mm)	$\pm(11.25° + 12.7$ mm)
# channels	274	198	144
# modules per side	14	14	4
Radial coverage (mm)	496.5	352.3	250.9

Table 2: Some parameters of the FPS modules.

surface on which all of the module construction is performed. This ensures that the modules properly conform to the spherical shape of the EC head.

The domes are constructed by fixing a $\approx$ 2-inch-thick aluminum sheet on the cutting table, and spinning it about a vertical axis oriented perpendicular to the plane of the sheet. A sharp cutting blade is then programmed to walk radially along the sheet with the height of the blade varying in order to carve out the shape of a sphere. A number of passes are needed in order to obtain a smooth finished surface with the proper radial tolerance. We produced four such "template" domes, each cut to a sphere of 100.42 inches (2550.7 mm) in radius. (This is the radius of the EC cryostat head.) The two larger (smaller) domes were each 36 (30) inches in diameter along their length, and were used for the construction of the larger (smaller) modules. The utility of constructing two domes of each type will become clear in later discussions.

2.3.2 Module Fabrication

The modules are independent structural units, consisting of wrapped scintillator strips, epoxy, and fiberglass cloth. They are constructed on the aluminum domes described above. The u and v ("stereo") layers, which are mirror images of each other, are each glued together independently and, after being allowed to set, are mated together in a seperate gluing step. A module consists of this doublet of stereo layers: *i.e.*, two sets of nested pairs. Each stereo layer is constructed in one step: the triangular pair of which it is composed is glued together as a single unit and allowed to cure. We note that this differs from the CPS technique, in which the lower sawtooth of the nested pair is glued to the backing material first. After curing, the CPS design called for using this first sawtooth as the registration template on which the mating half of the stereo layer was laid and glued.

One of the primary reasons we chose the single-unit approach is that we were concerned that the modules would have a tendency to delaminate using the sawtooth approach. Our initial R&D told us that this method resulted in layers that were held together by glue joints that fused aluminized mylar to aluminized mylar in adjacent strips, and that this tended to result in a structural connection that was too tenuous to rely on solidly. Construction of a stereo layer in one step resulted in modules that were composed of a continuous matrix of epoxy that had its own internal structural integrity, and thus provided an additional dimension of stability to the final product.

GEANT simulations have shown that the position resolution for electron showers in modules constructed with 6 mm isosceles triangular strips will be on the order of 1 mm. As an upper-limit benchmark, we tried to design a construction technique that would give an inter-strip alignment accuracy within a module of $\approx$ 20% of the electron position resolution, or 200 μm. Simulations suggest that this level of accuracy will not impact the electron-finding capability of the FPS. (The most stringent requirement for well-controlled strip-to-strip registration occurs at the trigger level, where the short time available for decision-making will allow no detector alignment corrections to be made.) Given the means of module construction, we have addressed the intra-module alignment at two different points during the module assembly: the strip-to-strip alignment within a given stereo layer, and the relative alignment of the two mated layers within a module. We address the two sets of approaches to the module alignment in turn below.

Intra-layer alignment

The primary means of maintaining the strip position within a stereo layer is with a pair of lateral alignment bars that have slots milled into their edges (see Fig. 6). These slots are used to anchor the ends (approximately the last 0.25") of every fifth scintillator strip on the bottom half of the stereo layer under construction. (We call these strips "registration strips" throughout this report.) The alignment bars are pre-bent to the relevant spherical radius, and they are fixed to the domes via threaded holes in the domes accessed through four countersunk through-holes in the alignment bars. The bars are kept thin enough (in their transverse dimension) so that bending in only two dimensions allows them to lie flush on the face of the dome. All strips that comprise the upper half of the stereo layer, which are nested into the lower sawtooth during epoxying, are free to move – they are not fixed to either the aluminum alignment bars or the lower strips in any way.

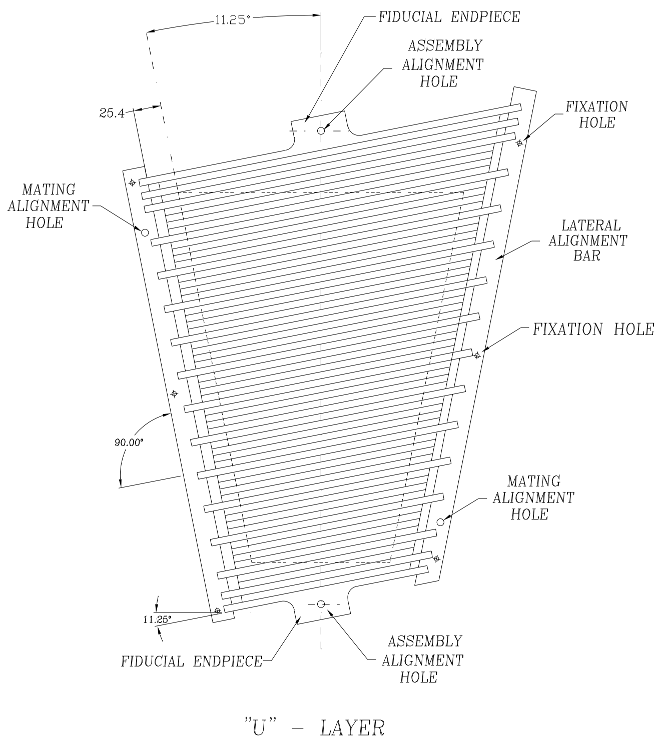

Figure 6: The two alignment bars with the fiducial endpieces at either end. The endpieces establish the proper orientation of the bars with respect to one another. Details are in the text.

The position of the alignment bars is set by a fiducial endpiece as shown in Fig. 6. This positioning is crucial to the overall strip-to-strip alignment within the module. A straight line is scribed into the dome across its diametric center. The quartet of pieces – two lateral alignment bars with a fiducial endpiece at either end – is assembled, and the scribed line is centered on the central fiducial hole in each of the endpieces. The angle formed by the scribed line and the lateral alignment bars is measured, and the assembly is adjusted until the proper 11.25° is made between both bars and the scribed center line. At this point, the positions of the fixation holes in the bars are marked into the dome, the assembly is removed, and the appropriate holes that will be used to fix the bars to the dome are drilled and tapped. This procedure establishes the position of the bars for all subsequent construction of this module type. The fiducial endpieces are used only to set the position of the lateral alignment bars and, once the positioning and fixation holes are determined and drilled, the endpieces are removed and are no longer part of the assembly procedure.

Since the glued stereo layer is placed under vacuum during epoxying, the dominant component of the force is radial – *i.e.*, along the direction of the radius of the spherical dome on which the assembly is constructed. (Calculations have shown that the vacuum forces result in a pressure of 5 psi.) The upper scintillator layer is forced into the lower layer into which it nests during the vacuum procedure, implying that the pieces of scintillator at the upper and lower boundaries of the module will, if left unsupported, "bow" away from the inner volume of the layer. In order to prevent any bowing of this kind, we also have designed precision-milled aluminum stops that are placed flush against the upper- and lower-most strips of each layer during the gluing and subsequent curing procedures (see Fig. 7). Like the alignment bars, these stops are screwed directly into the dome in order to maintain the proper scintillator spacing. The sides of the stops that abut the scintillator are milled at the appropriate angle so that they nest with the edge of the outermost strips of scintillator, ensuring a flush fit. There is no "outward" deflection of each of the strips, provided care is taken to prevent "bowing" at the top and bottom of the module. There is also no preferred non-radial direction to any of the resultant forces in the system. We therefore detect little or no systematic alignment bias introduced by this method of assembly.

For a strip with a measured base width of 6 mm, one would expect a nominal distance of 30 mm between the corresponding edges of two registration strips. In order to provide a region between the strips for epoxy to flow, we added 100 μm of additional space between each of the strips. This resulted in the 30.5 mm spacing between the slot edges. Since the strips are not really triangular in cross section, but instead are rounded at the three corners, the 100 μm additional space will not necessarily be enough to allow the tip of the upper nested triangle to lie along sphere – for the FPS prototypes, for example, the above construction constraints led to a strip-to-strip spacing shown in the upper right hand drawing in Fig. 8. We note that this nesting geometry – and hence the overall thickness of the detector – can be adjusted by varying this additional inter-strip space during design and construction. The minimum module thickness, however, corresponds to the strip spacing that allows the triangles to nest perfectly, as shown in the bottom right hand side of Fig. 8. (Proper nesting of the triangle – and module coverage – demands, of course, that the spacing be no larger than this.) The prototypes were slightly thicker than the possible minimum; however, we see no compelling reason to deviate from the module geometry defined by perfect nesting of the triangles,

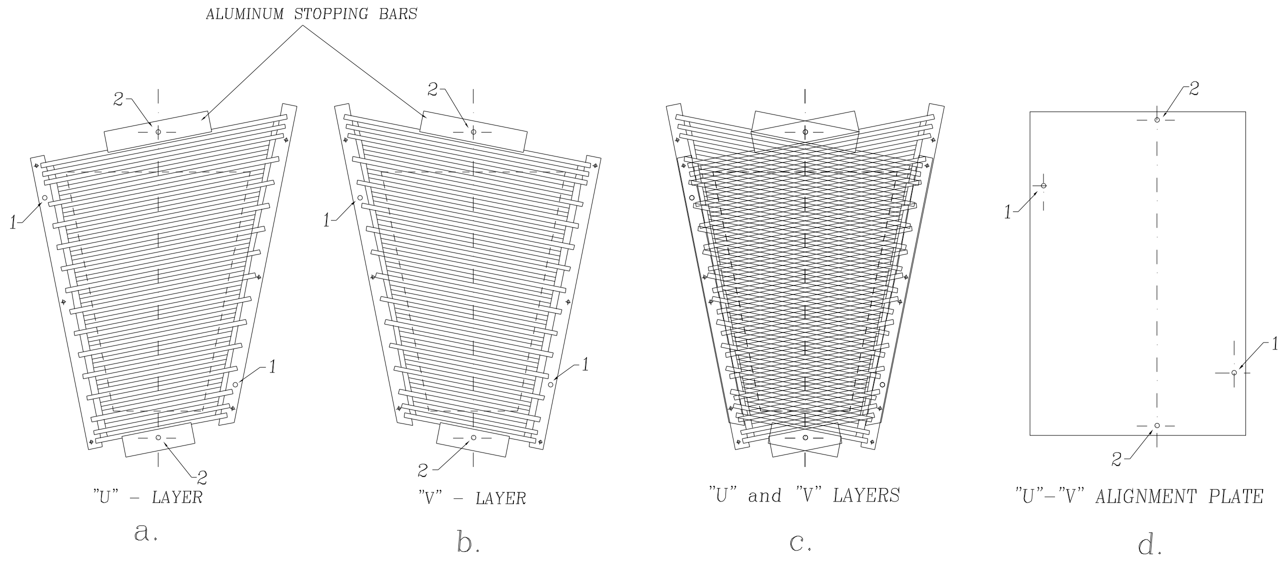

Figure 7: Drawing of an independent u (a) and v (b) layer, and the mated layers (c). The plate used to establish the alignment is shown in (d). The lateral alignment bars with their cattycornered alignment holes (1), and the upper and lower aluminum stopping bars with their fiducial reference holes for water-jet cutting (2), are shown.

and intend to follow this course during fabrication.

There will be $16 \times 1{,}024 = 16{,}384$ VLPC channels available for FPS readout. We define the sum of the signals in the small and large modules that subtend a $22.5°$ ϕ-wedge as a readout sector; this is the natural readout segmentation for use in the Level 1 trigger (see Sec. 3.7). Given that there are 32 readout sectors for the complete FPS detector, there can be a maximum of $16{,}384/32 = 512$ channels in each sector, or 256 in each u or v layer in a sector. (This ignores the small perturbation that the special modules introduce.) Assuming the CPS triangle geometry as shown in Fig. 8, each sector will consist of $274 + 198 = 472$ channels, or 236 channels in each stereo layer. Were one to try to populate all of the available VLPC channels for readout, the base size of the scintillator triangles could be reduced by $1 - (236/256) \approx 8\%$ from the CPS value. We do not see this as a sufficiently compelling reason to alter the extrusion dies, and intend to use strips of the same dimensions as those in the central region.

The module construction procedure consists of the following steps:

1. Plastic backing material is laid on the domes.

2. The lateral aluminum alignment bars are fixed to the domes at previously determined positions

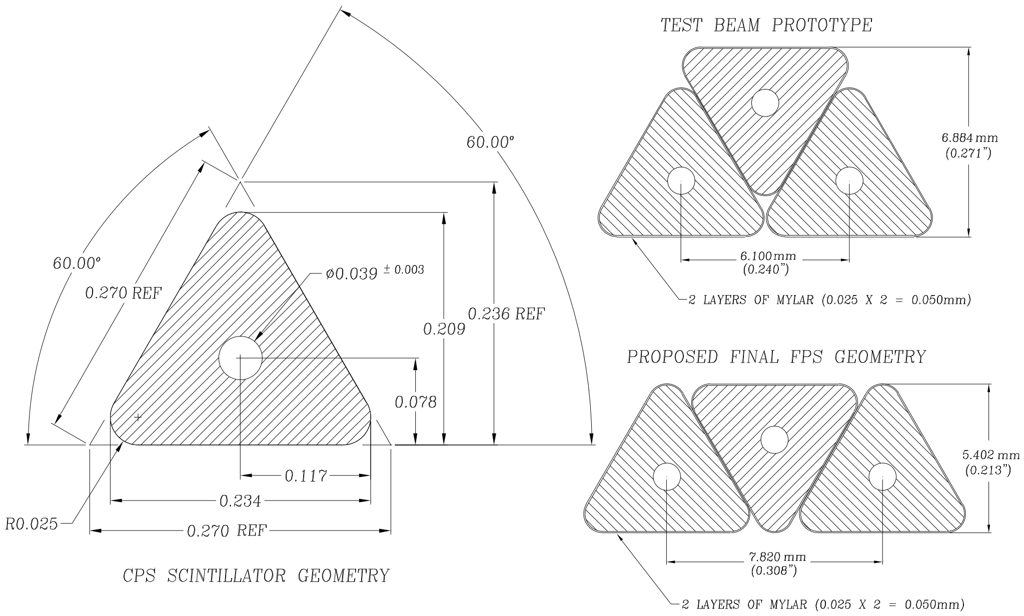

Figure 8: (Left) Detail of the scintillator dimensions used for the CPS detector. Dimensions are in inches. (Top right) The scintillator spacing of the test beam prototype modules. (Bottom right) The proposed scintillator geometry for the final FPS detector. The nature of the u-v nesting varies in the two latter cases.

in the manner previously described. These positions maintain the proper angle of the strip axis relative to the module edge. The bars are sprayed with a releasing agent in order to facilitate the removal of the scintillator strips from the alignment bars after curing.

3. Fiberglass cloth of thickness 0.012" (300 μm) is laid down in the region between the two bars. EPON epoxy, applied with either a tongue depressor, a "squeegee"-type device, a paint-roller, or some other appropriate applicator, is liberally spread over the cloth. Enough epoxy is applied to allow it to easily penetrate both the matrix of the cloth and the pre-determined inter-strip spaces.

4. Strips cut to the appropriate length and pre-slumped (see Sec. 2.3.5) are put in place one by one onto the cloth. Every fifth "registration" strip is carefully anchored into the slot. It is important during assembly to be sure that these registration strips are anchored properly, without any bias or rotational cocking of the strip as it goes in, as these strips define the alignment of all of the neighboring ones and, since the spatial location of all strips is strongly coupled, the rest of the layer.

5. More epoxy is again liberally applied, in a similar manner, to the upper side of this first layer of scintillator.

6. The upper sawtooth of the stereo layer is laid down, strip by strip. We note that none of these strips are anchored to the alignment bars.

7. A final layer of fiberglass cloth is laid across the top of this final scintillator layer, and coated with a last layer of epoxy. A thin plastic covering sheet is laid down on top.

8. The entire assembly is vacuum bagged, pumped down, and allowed to cure for at least 24 hours at room temperature.

The u and v stereo layers are mirror images of one another and each are constructed in parallel on independent domes. The two layers must then be mechanically mated to form the full double-layered module. Prior to mating, the alignment of one layer relative to the other must be established. This procedure is described below and illustrated in Fig. 7.

Alignment during u-v mating

The two lateral alignment bars each contain one hole that accommodates a 1/8" diameter dowel pin. The two dowel pins are inserted into the holes, which are in cattycornered positions on the two alignment bars. A thick (1/8") aluminum alignment plate with tight-fitting through-holes at the position of these pins is slipped over each of the layers. The plate also contains two precision-drilled holes at top and bottom which are used to position fiducial drill holes into the aluminum stopping bar at the top of each layer. Using bushings to guide the drill, thereby ensuring that the axis of the drill-holes are perpendicular to the alignment plate, fiducial holes are drilled into the upper and lower aluminum stopping bars on each layer independently. These fiducial holes provide the positioning of the two stereo layers relative to one another during the mating process. They also establish the absolute orientation of the module in space during the water-jet cutting of the fully assembled module.

After removing the aluminum alignment plates, what will become the upper (or upstream) stereo layer – the u layer – is removed from the dome. The mating surfaces of each of the layers are gently sanded to encourage adhesion. Epoxy is liberally applied on the lower layer and the upper layer is laid on top. Pins are placed through the upper and lower holes in order to establish the layer-to-layer alignment. Before the assembly is pumped down to begin the curing process, any overhanging areas of the upper layer are carefully shimmed to prevent any buckling of the upper layer from the vacuum forces. Our experience with the prototypes has taught us that this shimming process is somewhat delicate: over-shimming of the wings of the upper stereo layer can result in unwanted space between the two layers, impacting their relative alignment and the epoxy connection between them. Under-shimming can result in undue stress being applied to the wings of the upper layer. We used stock pieces of plexiglass and G-10 of varying thickness for shimming the prototypes, and were able to mate the two halves in such a way that no discernible alignment or structural difficulties resulted. Nevertheless, we will probably machine precise shims for this purpose when constructing the final FPS modules.

The mated assembly is allowed to cure for at least 24 hours. After curing, the (now over-sized) mated module is sent to Steel Art in Boston, Massachusetts, where the module is cut to size using a water-jet cutter. This process is described in the next section.

2.3.3 Water-Jet Cutting

A number of different means of cutting the modules to size were investigated. Laser cutting was found to be untenable: the plastic scintillator was heated during the process, and upon cooling sometimes blocked the holes. The aluminized mylar also proved to make use of a laser difficult, as the light tended to be reflected by the wrapping. After discussions with a number of vendors, this possibility was eliminated fairly quickly.

We also investigated using a milling machine. This procedure resulted in some excess plastic obstructing the holes, which had to be reamed out – although we did not consider this to be an altogether prohibitive feature. It was felt, however, that mechanical disturbances that result from machining the epoxied modules – particularly the ends of the scintillator – would tend to encourage delamination of the structure. This consideration drove a number of construction decisions: we felt it important to maintain a solid, single unit during each step. This resulted in our rejecting this avenue as well.

The most effective means we found of cutting the modules has been a water-jet cutting technique. This technology is used in the aerospace and other industries to cut metal, plastic, and other parts to size. A very thin jet of water is driven from a small nozzle at approximately 50,000 pounds-per-square-inch (psi). The module to be cut is placed on a digitally programmable table that uses the holes drilled in the upper and lower support bars as fiducial reference points. The form is cut relative to these holes according to prints provided by BNL. A tolerance of 1/32" ($\sim$ 30 mils) is guaranteed by the vendor; accuracies of better than half that have been typical in the prototypes that were cut using this technique. This technique has proved to be an accurate, inexpensive, and reproducible means of cutting through both the plastic and the mylar with equal effectiveness. It produces a very clean module edge.

In order to facilitate cutting, and to ensure a reasonably clean edge, sand or grit is traditionally added to the water prior to pumping. The size of this grit can be varied, according to one's needs. Upon return of the first modules, we found that a small amount of sand was occasionally forced transversely into the holes into which the wavelength-shifting fibers were to be inserted. We spent a significant amount of time investigating whether the modules could be cut with water only: that is, with eliminating the sand from the water. It was found, however, that the abrasive power of water alone was insufficient to produce a clean, reliable edge, even when more powerful pumps were used. This avenue, therefore, was abandoned. We have instead opted to live with the infrequent migration of sand into the WLS channels, and instead intend to remove it with either a gentle water-jet or air gun prior to inserting the WLS fibers. Any scratches to the inner scintillator surface should not impair the light collection properties in any way. Studies are underway to quantify this effect.

Miscellaneous comments

The final design for the detector calls for a gap of 2.5 mm between the spherically curved surface of the module closest to the interaction point and the aluminum cover skin directly above it. (This gap was not needed in the test beam prototype.) The gap provides space for some of the WLS fibers that are routed over the top of the module before exiting the outer ring of the detector. (This routing helps to ensure that the 2" minimum bending radius that is specified for the fibers we are using is respected – see Sec. 3.3.2.) In order to maintain this 2.5 mm gap, we expect to attach ≈ 4 or 5 plastic standoffs to the upper surface of the modules, probably with epoxy. These standoffs will be applied either directly after the module is cut and returned from the vendor, or after they are installed in the support structure and cabled.

During the construction of the prototypes, we grew concerned that cross-talk might adversely effect the pattern recognition in the detector. In particular, we took measures against the possibility that light from the scintillator might travel axially along the length of the strip, exit out the ends, and bathe the complement of WLS fibers that are routed in this region in unwanted light. (Cross-talk internally from fiber to fiber requires that the light pass through four layers of cladding at the proper angle; we expect this effect to be negligible.) Since the fibers coil in many directions in this region, it is possible that spurious light in this region may enter some of the fibers and be picked up at the readout end. We did not have sufficient time at that point to quantify this effect, but decided to err on the side of caution. All of the prototype module edges were spray-painted, using a paint gun, with a few (three to four) coats of black paint. It was necessary to thin the paint with alcohol to ensure that the gun did not become blocked with paint as the coats were applied. Toothpicks were placed in the holes during painting in order to prevent the paint from entering the holes. We would like to avoid this additional step, and are currently in the process of quantifying this effect. We do have, however, a proven method of painting the modules should it prove to be needed. We are also in the process of investigating the possibility of designing a suitable jig that will enable us to more easily plug and protect the holes during painting.

In the original trapezoidal geometry, the large modules extended to $|\eta| = 1.5$ at their outer radii. (The coverage here is measured at the center – *i.e.*, at the upper edge along the bisector – of the module.) After mocking up the final proposed outer radius of the detector, including the cabling and the connector placement, we found that we were able to slightly extend the coverage by cutting a circle, rather than a straight edge, along the top of the module. Such a cut would provide little or no gain at the inner radius and, since space is tight there for cabling, we will probably leave this inner edge straight. In this scenario, the outer edges of the modules in a given layer will define a contour of constant η. The wings of the modules will define this pseudorapidity, and this circular cut will pass through these outer corners. The coverage for the large modules in this design will increase to a constant $|\eta| \approx 1.47$. We are in the process of discussing with Steel Art, the vendor who will do the water-jet cutting, any potential complications that such a circular cut will introduce. Our final decision will be based on these discussions. Naturally, all of the three module types will have either the straight or the circular cut – we will not mix the two in the detector.

Since constructing the prototypes, we have developed a tentative means by which we will place survey marks on the modules that will be used to establish the absolute alignment of each of module in space. We intend to string three wires across the curved face of the upstream u layer during gluing: one will be strung along the module bisector in ϕ, and the other two will be run across lines that are parallel to both the nominal upper and lower module edges at a position corresponding to 25% of the length of the module. (It is possible, but unlikely, that such a system will be needed for the underlying v layer.) This provides two points of intersection along the center of the module that can be used to establish the position (and orientation) of the module in space. These thin wires will be precisely positioned by attachment at appropriate pre-drilled holes (and pins) in the lateral alignment bars and, in the case of the bisecting wire, at either the aluminum stopping bars or at the outer diameter of the construction dome. They will be strung just underneath the final layer of fiberglass cloth before the u layer is pumped down for curing. One would like the wire to be thin enough to allow for an accurate measure of its position, but strong enough so that it remains straight as it is strung and drawn taught during assembly over the scintillator surface. Gold-plated tungsten wire of $\approx$ 100 μm in diameter can withstand up to 500 grams of tension, which should allow us to reliably and reproducibly determine the position of the crossing points. The wire diameter and material will be varied as needed. These two fiducial crossing points will also allow us to establish the absolute orientation of the water-jet cut relative to the scintillator: the position of an upper (or lower) and lateral module edge with respect to both crossing points will allow us to determine the angle of the scintillator strips relative to the module edge and, by interpolation, the absolute position of a given strip anywhere in space.

2.3.4 Module Testing

The modules will be tested at various stages of the construction. The scintillator will be visually inspected after extrusion, and during the wrapping at Fermilab (see Sec. 3.5). After cutting, we intend to check the alignment of the strips in each module on an optical bench, rejecting any that are out of tolerance. After each module is installed on a given layer (see Sec. 2.4.4 below), the connectors will be anchored, the WLS fibers routed, and the scintillator-WLS fiber-connector chain will be tested using either cosmic rays or a source. Use of a source is the preferred choice at the moment, as the rates will not introduce any limitations. In this latter case, a step-motor will move the source up the center of the module in fixed increments, and the corresponding strips will be read out and the data analyzed. Bundles of clear waveguides will be terminated in the proper sixteen channel mating connector and fixed directly to the already-installed WLS connector for readout. The end point of most available sources do not exceed $\approx$ 3.5 MeV, which will provide an insufficient rate for testing both the upper (u) and lower (v) layers at once. It is likely that the two sides of the module will have to be tested independently: in this case, two sets of measurements will be made, with the source being run up the over- and under-sides of the module (probably on top of the aluminum skins) in separate steps.

Readout for the test station will consist of a PC, a multi-channel phototube (64 or 96 channels), a CAMAC interface, and the LABVIEW software package to facilitate online histogramming and feedback. Appropriate records will be kept for each module. Should it be found to be sensible and/or necessary, we will test the modules (or a subset of them) at various stages of the layer-to-layer mating. We expect that, at a minimum, some additional testing will be done after the full detector sub-half is bolted together and the vertical mounting procedure is performed (see Secs. 2.4.4 and 2.4.5).

2.3.5 Scintillator Strip Preparation

One of the more labor-intensive portions of the construction process is the preparation of the scintillator for module assembly. An effort has been made to minimize the waste of scintillator resulting from cutting away the module border during the water-jet procedure. The trapezoidal shape of the modules, along with the assembly technique we have chosen to employ, dictate that each of the scintillator pieces must be individually cut to size and prepared prior to assembly. We have kept this border to about one inch (see Fig. 6). We have considered the possibility of cutting out more than one module from larger preformed layers, but this would result in more demanding alignment procedures during module construction, and would also increase substantially the amount of wasted scintillator.

The pre-cutting of the scintillator must be done carefully, so as to avoid cracking the piece along its length, or developing other types of stress fractures. Visual inspection after cutting with a sharp hand-cutting tool have revealed no blemishes beyond $\approx 1/4$" from the scintillator edge, a safe distance from the one inch border that is cut away. Because the scintillator is already wrapped when it is cut, care must also be taken to prevent the wrapping from unravelling after the cut is made. (There will be no tape or glue to keep the aluminized mylar in place at this point.) We therefore wrap each piece at each end before cutting with thin ($\sim$ 1 mil) mylar tape, taking care not to overlap tape to form any double layers. It will be recalled that the scintillator ends must lie flush with one another in order to ensure that no mis-alignment occurs. For the same reason, it is also critical that the ends of each of the registration strips lie neatly and uniformly in their corresponding slots in the alignment bar. Additional thickness due to tape or any other source will cause a perturbation of the strip-to-strip registration at the ends, and distort the overall structure. We therefore take considerable care in applying the tape at this stage. We remind the reader that the tape is removed at the cutting stage. It is therefore only a temporary bond meant to maintain the integrity of the wrapping prior to gluing of the module. The strips are numbered with a felt tipped pen as they are cut according to their position in the module.

After cutting and taping, the strips are pre-bent ("slumped") by heating them to 170°F for two hours under vacuum on one of the aluminum domes. In order to help maintain the proper relative shape of the strips – ensuring the proper concavity (convexity) of the lower (upper) layer of scintillator during slumping is most important – the strips are laid in the alignment jig during this procedure. The oven is turned off after heating, and the strips are kept in the oven overnight so that cooling is gradual. We are currently in the process of studying whether heating the scintillator results in any short- or long-term change in its response characteristics.

During the module production R&D, we learned that epoxy could easily wick up into the extrusion holes during the gluing procedure. Although we were able to ream out most of the blocked (or partially-blocked) holes for which this occurred – which represented $\approx 20\%$ of the strips in a glued layer – using a thin drill bit, we were loathe to corrupt the scintillator in such a way. It was clear that a reliable preventive measure had to be taken during assembly, prior to the application of the epoxy. Once the strips are slumped and cooled, therefore, we plug the holes at the ends of the scintillator with five-minute epoxy. (To avoid any potential fractures in the plugging epoxy, we plug the scintillator strips after they are slumped.) Care is taken to prevent the plugging epoxy from creeping too far up the opening: since a border of about 1" is provided for prior to cutting, the plug must extend no farther than this. We aim to plug approximately 1/4" into the hole. Care must be taken to ensure that the epoxy bead lies only on the cross-sectional face of the scintillator, and does not extend anywhere down the length of it. This ensures that the scintillator layers nest properly when they are glued. The bead must also cover the entire hole: we found that even small, partial exposures of the hole entrance allowed some of the epoxy to wick up into the scintillator. (For the prototype construction, this was complicated by the fact that the modules were constructed out of the scintillator that was extruded for the final CPS detector. This scintillator had a tear-drop-shaped, rather than round, hole that accommodated the WLS fiber. Extra care had to be taken to seal the entire profile of the hole properly in this case.) The five-minute epoxy is allowed to cure overnight before the scintillator is glued together; we use the five-minute version because its quick-setting properties prevent wicking during the plugging process. In order to enable us to control the depth of the epoxy applied, we at times broke a 0.835 mm diameter fiber into 1/4" lengths, dipped them one by one into the 5-minute epoxy, and inserted the fiber fragment with its epoxy bead into the hole. This helped us to control the actual application of the epoxy during plugging. The protruding fiber ends were cut off after curing.

The strips will be visually inspected for any irregularities, especially at the scintillator ends, before they are placed in the jig for gluing. Experience has shown that we can expect $< 1\%$ of the strips in the final modules to have any problems at their ends that are related to plugging of the strips. (These problems will in any case occur at the accessible ends of the strips, in the less-critical overlap region.) Depending on the severity of the problem, modules containing any plugged ends will either have the corrupted strips reamed out, will be used for spares, or will be discarded.

Once the scintillator strips are precut, taped, slumped, and appropriately plugged, they are ready to lay into the jig for the assembly procedure described above. The entire module assembly procedure is quite labor intensive and, when assembling 64 modules consisting of some 14,300 channels, one can expect that the process will require a significant amount of attention to detail for a reasonably extended period. (With spares, we expect to fabricate a total of 73 modules – three spares of each of the three types of modules.) Once the final jigging is machined and ready and the procedure is well in hand, we expect to be able to assemble approximately 2 modules per week. This assumes one technician working full-time on module production, with intermittent help from one or two others.

The R&D associated with the prototype construction was quite successful. It enabled us to develop a suitable solution to most of the details and complications associated with module production, including strip preparation, slumping, gluing, intra-layer and u-v alignment, and cutting the modules to size. We have converged on a reproducible, proven procedure that we are quite confident is sufficiently robust to provide us with structurally solid and accurate tracking elements.

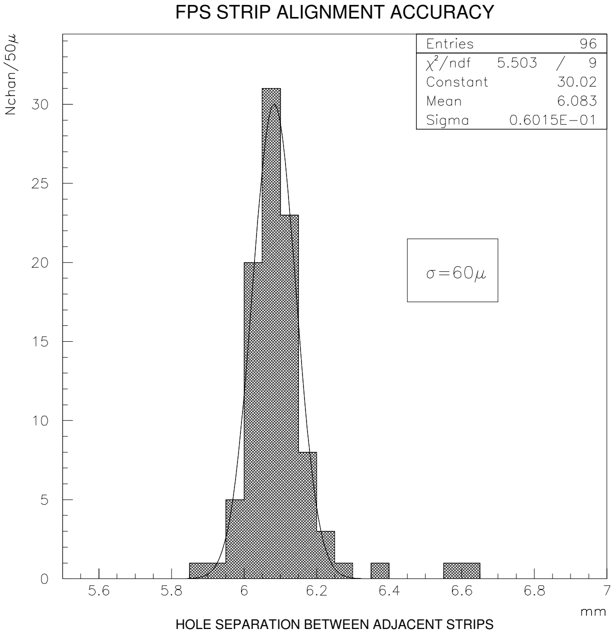

Figure 9: Distribution of individual measurements of the position of the scintillator strips for one of the test beam prototype modules. The measurements were performed on an optical bench. An accuracy of 60 μm was achieved.

We have mentioned above that our goal was to establish strip-to-strip registration of less than 200 μm. Using an optical bench, we measure a strip alignment accuracy within a module of 60 μm – well within our expectations (see Fig. 9). We expect that the resolution in the strip registration accuracy for the FPS will be dominated by the variations in the module-to-module position within a layer, the alignment of the four FPS layers relative to one another, and the overall positioning of the detector in space during mounting to the cryostat. Our means of controlling these contributing effects is intimately coupled to the support structure, and we discuss them in this context below.

2.4 Detector Support Structure and Assembly

Once the modules have been built and cut, it remains to mount them to an acceptable support structure. This section describes the current design of this frame, which provides the structural matrix for mounting the active detector elements.

One of the primary constraints in developing the support structure is the need to negotiate the installation of the FPS with the beam pipe already installed. We decided to build this capability into the design so that we would not be absolutely compelled to deliver the FPS early for installation, allowing us more time for detector R&D, design, and construction, should it be needed. By necessity, then, the detector must be composed of at least two independent pieces that will be joined in some way during the installation and mounting procedure at Fermilab. Given the schedule and its associated uncertainties, we are also (conservatively) assuming that the FPS-North will have to be installed while the detector is in the collision hall, where the detector access and means of suspending and supporting the FPS as it is being installed will be limited. This consideration (primarily) has motivated our decision to design each FPS detector half (*i.e.*, north or south end) so that it consists of the smallest number of possible pieces (two). This minimizes the amount of internal detector cabling and detector alignment adjustments that will have to be made during installation in this limited space. The layers of each of the two halves will be assembled, aligned, and bolted together at BNL during detector construction – in a controlled environment – and not during installation at Fermilab. Where possible, we have built into the design the capability of assembling the detector reversibly and in stages, which will allow us to incrementally adjust the alignment as it is constructed, if the need arises. The primary alignment considerations during mounting at Fermilab then become those of maintaining the relative alignment between the two mounted halves, and the overall detector positioning. All of the internal degrees of freedom are dealt with during assembly at BNL.

2.4.1 Structural Components

The FPS will be constructed of layers of modules that are mounted directly to thin aluminum sheets that have been appropriately shaped to conform to the outer head of the EC cryostat. The sheets in each layer will be structurally supported by an aluminum frame consisting of radial ribs and an inner and outer support ring.

The sheets are made by a method that is conceptually analogous to that used to produce the template domes on which the modules are constructed: an aluminum sheet is spun on a pre-fabricated dome of the same radius as the EC head, and a digital machine is programmed to move a small, steel spherically-shaped ball radially along the sheet at a height corresponding the radius of the template dome. A number of passes are made, after which a sheet of the proper dimensions is produced. A hole corresponding to the inner radial boundary of the detector (~ 200 mm) will be cut from the sheet either before or after it is spun. There are four layers of modules for each half of the FPS (north and south); with a mounting skin and a protective covering skin for each layer, and an additional sheet which will be used to mount the lead absorber, $9 \times 2 = 18$ sheets in all will be needed for the final detector. Spares and additional (thicker) sheets, to be used during assembly, will also be fabricated. We expect all sheets used for mounting the detector to be 1 mm in thickness. Given the means of structural support (see below), we expect sheets of this thickness to offer enough rigidity to provide a proper mounting surface for the modules, and a fair amount of flexibility to allow us to form the sheets to the desired radius during assembly. This latter characteristic is an important one, as the sheets will be fabricated by the vendor with a finite tolerance in their bending radii. We anticipate that some retro-fitting will be necessary during assembly.

The aluminum mounting sheets will need additional machining in order to be used for the detector mounting and assembly. As already mentioned, each detector half will be composed of two pieces, which dictates that each of the sheets be cut into two pieces to allow for this type of assembly. In addition, a notch must be cut out of each sheet to allow for the passage of the magnet services through the relevant slice in ϕ (see discussion below). A central hole of ≈ 200 mm to accommodate the Level 0 detector will also need be cut out of each sheet (see above). The fabrication of full 2π sheets, each containing the central hole, will be done by an outside vendor. We are currently discussing this part of the project with Spincraft, located in North Bellerica, Massachusetts. The other adjustments – half-sheet cuts and notching – will be form-fitted during installation. This is discussed in some detail later in later subsections.

The aluminum supporting frame will provide the structural integrity for the detector. The aluminum sheets in each layer will be directly fastened to the frame: recent investigations have found that utilizing a simple hand-riveting tool provides a very solid, mechanically sound connection. The frame itself in a given layer will consist of eight radial ribs spaced at 45° intervals in ϕ that are fastened at either end to an an inner and outer support ring (see Fig. 10). The ribs will be bent in two dimensions to conform to the curvature of the EC head. The rings will contain milled slots 45° apart – corresponding to the rib-to-rib angular spacing in ϕ – that will accommodate the placement and attachment of the ribs. The ribs will also be machined at their ends to further facilitate proper ring-rib mating. The pieces will be milled in such a way that the support elements fit snugly together with the proper spatial relationship between them, and so that the support frame is of a uniform thickness throughout. A given layer of the detector consists of the support layer and eight modules, both sandwiched between two aluminum sheets.

The outer rings will also be machined to contain milled slots through which the wavelength-shifting (WLS) fibers will pass as they exit the edge of the module and are routed to the outlying connectors (see Fig. 22). The connectors are mounted to brackets that are in turn mounted to the outer ring. (A more detailed discussion of the connectors and those aspects of the support structure that are relevant to their mounting will be presented in Sec. 3.2.) We also note that, due to the different radial extent of the forward and backward layers, the outer support rings will be of two different sizes, each corresponding to the outer radius of the inner and outer layers of the detector (see Fig. 12). These rings will naturally accommodate the connectors for their corresponding layers.

The outer support ring is bent in two dimensions, and contains milled slots to which the connectors will be mounted at the appropriate positions in ϕ. Assembly and installation concerns demand that it be composed of three pieces. The surfaces of both of the rings at their inner- and outermost $|z|$ positions will be machined in order to ensure that the rings in adjacent layers nest properly with one another. The outer rings in Layers 1 and 2 will also contain through-holes located in at least four positions in ϕ to allow the outer radius of the assembly to be tacked to the cryostat by studs that will be welded to the cryostat at pre-determined points prior to installation. By far, the

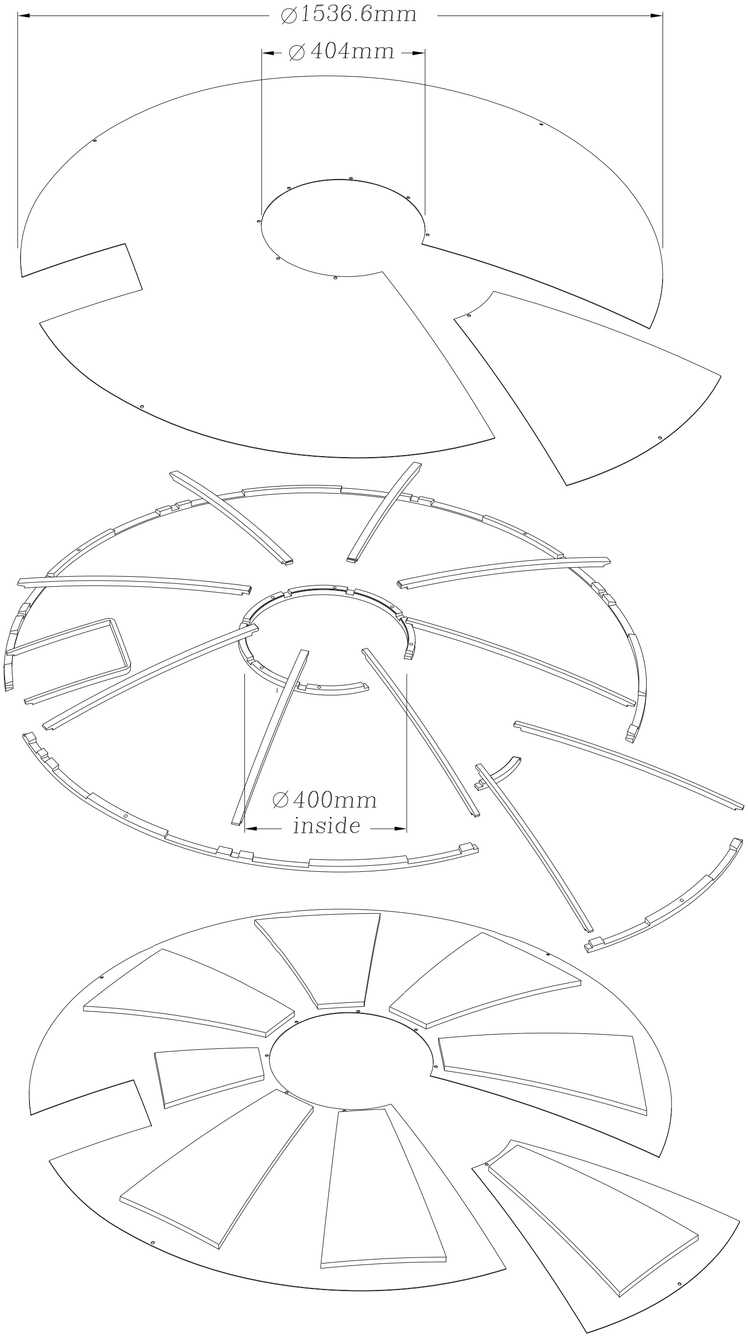

Figure 10: Exploded view of the complete innermost layer (Layer 1) of the FPS. The upper aluminum cover sheet (top), the sandwiched support frame (middle), and the lower sheet to which the modules are mounted (bottom) are shown. Note the magnet service channel and the two-piece structure of the support frame and skin. The milled slots in the outer rings that accommodate the exiting WLS fibers are shown as well.

most important piece of the support structure is the inner ring. In addition to providing structural support, it will provide all of the precision mounting and alignment holes for the detector. We therefore describe this element in detail in a following subsection, in conjunction with a description of some aspects of the alignment of the detector. We first discuss the fabrication and mounting of the lead.

Lead Absorber

The lead absorber for the prototype detector used at the test beam was built out of 11.25° wedges which were epoxied to stiff wedge-shaped aluminum backing supports. The lead wedges were nested along lines of contact at constant ϕ to eliminate any projective cracks. We feel that the construction and assembly will be simplified by fabricating full half-domes of lead[1], mounting them to an aluminum sheet, and fixing the sheet+absorber sandwich to the upper and lower support frames that they abut. Discussions with Spincraft, who will be supplying the aluminum sheets, have given us confidence that the 11-mm-thick ($2X_0$) absorber can probably be spun to shape in an identical manner as the support sheets.

Care must be taken in forming two half-domes of lead from one full spun dome to ensure proper coverage of the aborber – *i.e.*, that there be no projective cracks. Upon creating two half-domes from one spun piece, enough material would be cut away so that the mating edges would not nest neatly without some settling of the smaller piece into the larger one, resulting in two pieces that have a different inner radius. Also, in order to eliminate the projective cracks, the geometry of the cut along the edges that mate has to allow for some step or diagonal surface – a straight cut will be insufficient. We are currently considering a number of ways to deal with these problems – fabricating the half-domes from two spun domes would probably be prohibitively costly, and wasteful. We are currently leaning toward a solution that entails constructing the half-domes from a lead sheet that is slightly larger in diameter than the final piece of lead we intend to mount. The slightly oversized piece of absorber would then be spun, the central hole cut out, and a wedge of the proper angular extent (the mating "half-dome") cut from it on a bias, so as to ensure proper "non-projective" nesting along the edges. The two half-domes will then mesh properly, but when mated, will have different inner and outer radii. The pieces will each then be re-machined to the proper inner and outer radius. Discussions with Spincraft, as well as other companies, are currently underway to evaluate the viability and cost of such a procedure. Initial indications are that it can be done for a reasonable amount of money.

We will be procuring antimony-doped lead (6% Sb) for the absorber, which help to maintain the rigidity of these large, reasonably heavy structures. (The larger of the two pieces will weigh about 150 pounds.) The lead will be tacked along its length to the adjacent ribs to ensure a solid

[1] We use the term "half-domes" to denote either of two mated spherical pieces – large or small – of the support structure or its components – *i.e.*, the term does not necessarily refer to a $\Delta\phi = \pi$ angular section of the detector, but rather to the two pieces under discussion in a given layer that when joined will subtend 2π radians.

connection to the frame and to prevent creeping. It will be mounted to the same 1-mm-thick sheets as the modules will be mounted to – probably by a combination of epoxy and rivets – and this sheet will in turn be fixed to the inner and outer rings for additional support (see Sec. 2.4.3). We have performed a finite-element analysis on the appropriate lead alloy in the relevant half-dome geometry we expect to employ (see Sec. A.1). When the larger of the two pieces of lead is suspended (alone) from its two upper corners only, the maximum stress seen is 593 psi, which is less than 21% of the elastic limit of the material (σ_y = 2,800 psi). Moreover, the stresses above 60 psi are limited to a region that is less than 5% of the size of the structure. The maximum deflection in the structure is also less than 0.009" (230 μm). Our scheme for mounting the lead distributes this small amount of stress over a large area. We therefore expect, given the limited nature of both the stress and the deflection of the absorber, that our plan for mounting the lead will be quite adequate, even over the long term, and intend to pursue this course. We mention, however, that should we learn anything in the interim that causes us to question this scheme in any way, we intend to return to the original method that was used for the prototypes. This method has proven to be a viable and quite satisfactory solution, and it could easily be applied in the final detector.

2.4.2 Brief Discussion of a Few Design Considerations

Three Dimensional Bending

There are a number of non-trivial complications associated with the construction of a spherical detector. Every step must be performed on a spherical template of some sort. Maintaining reasonably tight alignment tolerances over a detector of this shape over the $\approx$ 1.54 m diameter requires some special assembly and design considerations. The malleability of materials one uses and the expense of the construction procedure become more of an issue than they would otherwise be. We would have far preferred to simplify our lives by building a detector that is conformally bent in only two dimensions.

This was one of the first things we investigated during the R&D associated with the prototype module construction. We found that building modules that subtend the same range in η and ϕ as those currently proposed, but are bent in two dimensions rather than three, results in an additional 3 mm (5 mm) of space required (in z) per small (large) module at the module's outer wings (*i.e.*, the upper left- and right-hand corners). Over the entire four-layer structure, this would result in the addition of $\approx$ 20 mm in thickness to the detector in the range $1.65 < |\eta| < 2.5$. This is roughly half of the space that remains between the lower tip of the solenoid and the FPS in our current three-dimensional design – this is one of the tightest regions in the experiment. We consider this waste of precious real estate to be unacceptable. Since there were no acceptable design modifications by which we could reduce this amount of dead space to tolerable levels using a two-dimensional bending technique, we opted to design a spherically-shaped detector and learn to deal with whatever additional difficulties it presented.

Given the spherical shape of the detector, each layer would have to be constructed at a different radius in order to make the detector nest perfectly – this includes the inner and outer radii for each set of ribs, the aluminum sheets for each layer, etc. On the other hand, construction of all of the detector elements at the same radius – the template domes, aluminum sheets, modules, ribs, and so on – would greatly facilitate the construction and help to contain the cost. We have calculated the effects of building the detector from one radial template, and find that the additional amount of space that this introduces is negligible. We have therefore opted to build all of the elements at one radius of curvature. Similar studies have shown that the ribs can be bent to the proper shape, rather than machined, even though this results in their inner and outer surfaces having a different radius of curvature. Machining would have been required if the amount of additional dead space after bending was prohibitive in any way. It would also have been far more expensive.

Accommodation of Solenoid Services

The ϕ-symmetry of the detector is broken on both the north and south sides by the presence of steel channels that contain magnet services (cooling lines, current return, etc.) These channels are centered at $\phi = 332.946°$, or $27.054°$ below the (horizontal) $+x$ axis, and begin at an inner radius of ≈ 544 mm (see Figs. 4 and 12). The angular region swept out by the two corners at their inner radii subtends approximately $\pm 10°$. They are a constant 185 mm (7.28") wide in ϕ throughout their length, and take up all of the room in z between the end and central cryostats from the inner radius of the solenoid to the outer radius of the FPS and beyond. In these (and perhaps a few neighboring) ϕ-segments, then, the FPS must be truncated so that the magnet service channels and the preshower do not conflict. We treat this region as a "special case", and have considered a variety of ways of integrating it into the design of the FPS.

There are a number of means by which these channels could have been accommodated. Our final decision was driven by our belief that the most important part of the FPS is that which offers tracking information both before and after the lead radiator. This corresponds to the more forward pseudorapidity region, $1.65 < |\eta| < 2.5$, which is covered by both the large and the small modules. We have therefore chosen that option which gives us the most complete and uninterrupted coverage of this region. These considerations result in a $45°$ region around the solenoid service area in which both the forward and backward modules are truncated in pseudorapidity, covering $1.8 < |\eta| < 2.5$. Coverage in ϕ remains complete in this region. There will be four small "special" modules that will be constructed for each of side of the FPS (eight in all) for this region. The support structure – specifically, the rib elements and the outer ring – will be modified in this region as well, as shown in Fig. 4. All remaining modules, including those directly neighboring these "special" modules in ϕ, and the rest of the support frame, will remain unchanged.

Impact of Installation on Detector Geometry

We have investigated two approaches to installing, and hence constructing, the FPS: one calls for affixing the detector to the cryostat layer-by-layer, and the other consists of mounting two fully pre-fabricated detector "sub-halves" successively on the end calorimeter head. We have opted for the latter approach. The basic scheme we intend to follow is illustrated in a 3-dimensional drawing in Fig. 12. The two halves of the FPS will be constructed independently at Brookhaven before shipment to Fermilab. The mated pieces are staggered at their edges due to the fact that modules in adjacent layers are offset by one module-width in ϕ: any plane containing the beam line that penetrates the detector will cut through at least two modules. The staggered edges occur at module boundaries, ensuring the integrity of the active volume of the detector.

Many features of the final detector geometry seen in Fig. 12 are driven by installation concerns. As already discussed, scheduling uncertainties dictate that we have to be prepared to install the preshower while the detector is in the collision hall and the beam pipe is in place. In this scenario, the end calorimeters will be rolled out from the barrel, leaving a 39" gap to work in. This small amount of available working space helped to motivate our decision to throw out the design that required installing the detector layer-by-layer *in situ* – we felt this scenario to be unnecessarily unwieldy and cumbersome.

Many of the important details of the nesting of the two halves in our preferred solution are also determined by installation limitations. Although the lower (upper) half of a given side of the FPS will weigh only about 310 (185) pounds, some means of suspension will have to be devised in the collision hall that avoids the cryogenic piping overhead: there will be no crane available. One option would be to to install the detector by first suspending and mating the two halves over the beam pipe, followed by fixing the resulting single unit to the cryostat in one piece. Given the limited means of suspension and small amount of space that will be available to perform such a procedure, we consider it unlikely that we will pursue this avenue. This being the case, it means that, whatever their geometry, the detector halves must mate in such a way that the two halves can be bolted to the EC in succession. This then dictates the nature of the nesting of the two sections: the half that is bolted to the cryostat first has as its largest (smallest) layer (in ϕ) that which is closest to (furthest from) the cryostat. This geometry then allows the mating layer, which naturally consists of the opposite nested orientation, to be installed directly on top of its counterpart. No after-the-fact adjustments to the lower half will be needed after it has been mounted.

With the above considerations resolved, the important features of the nesting geometry of both halves of the detector are more or less fixed. Physics, triggering, and reconstruction considerations dictate that the seam between two FPS modules line up with the boundary between two calorimeter pads – or, more preferrably, between two calorimeter trigger towers. This establishes the absolute orientation of the detector in ϕ. Structural ease and simplicity suggest that the FPS hardware adaptations to the magnet channel be subsumed into one half of the detector or the other – not both. Once all of these considerations are properly integrated, the detector is constrained to look like that which we are proposing for the final design (see Fig. 12).

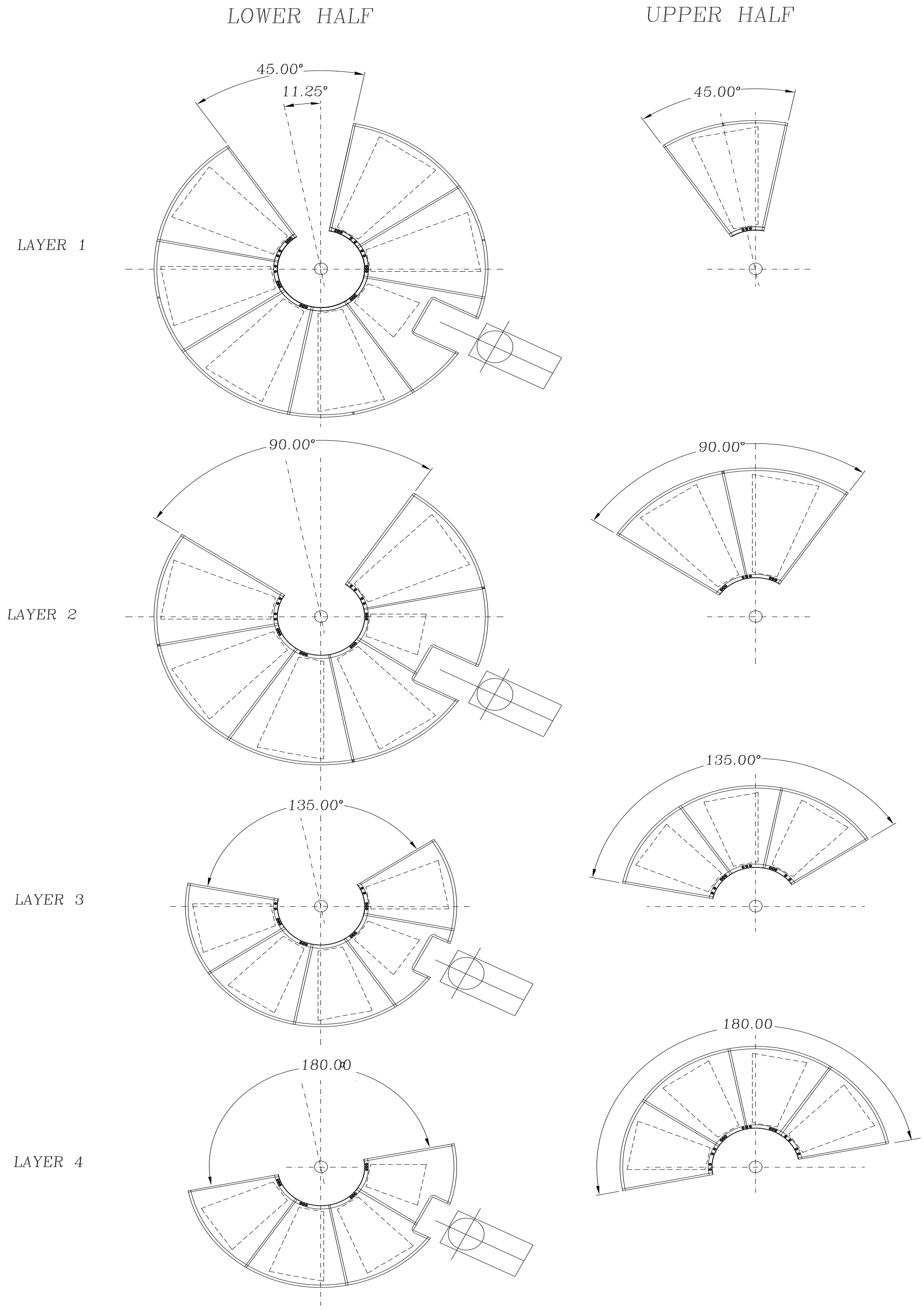

Figure 11: Geometry of the individual layers of the FPS for each sub-half of the detector. The four elements on the left- and right-hand sides bolt together independently, with the relative orientation in ϕ as shown. They together comprise the lower and upper halves of the detector shown in Fig. 12. The accommodation for the magnet services are shown.

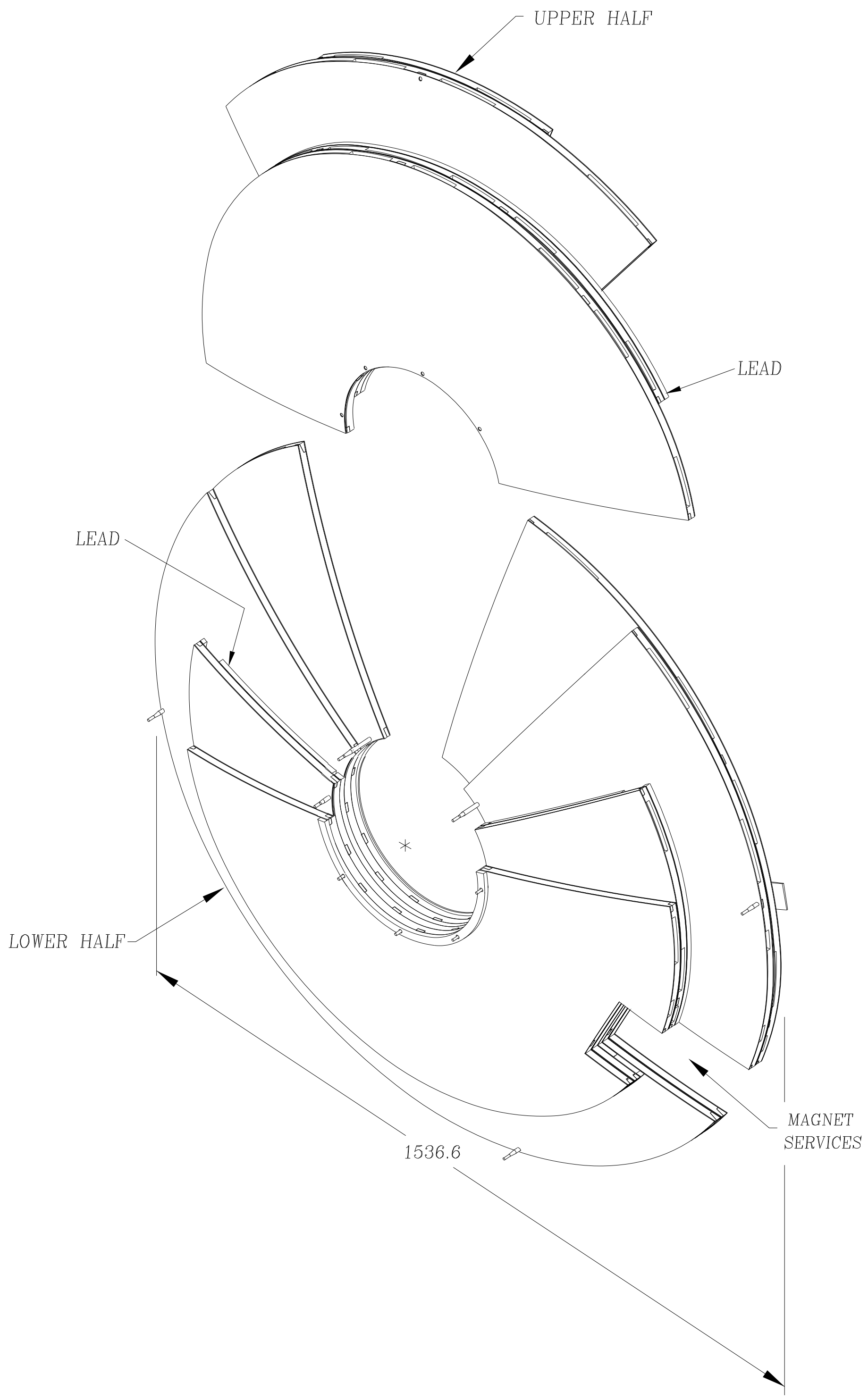

Figure 12: Fully constructed sub-halves of the FPS. The layers in Fig. 11 are bolted together to form the fully assembled structures, as shown. The outlying mounting bars that anchor the connectors are not included (see Fig. 22).

2.4.3 Detector Alignment Issues I: Inner Ring Design

As a benchmark, we are attempting to establish the position of each module in space to about the expected resolution for electromagnetic showers, or 1 mm. The alignment of the detector naturally falls into four categories:

1. *Intra-module alignment.* This portion consists of the strip-to-strip alignment accuracy within a module. As already mentioned, we have measured this to be 60 μm in one of the prototype modules. We also include in this portion the u-to-v alignment accuracy, which is established when the two stereo layers are mated (see above). Given our experience with the prototypes, errors of this order are also expected from module-to-module variations in the absolute orientation of the water-jet cutter.

2. *Module-to-module alignment.* This refers to the accuracy with which the modules are placed relative to one another, within a given layer.

3. *Layer-to-layer alignment.* The contribution to the module-to-module alignment accuracy due to the positioning of layers relative to one another as the detector is assembled.

4. *Overall detector positioning.* The alignment of the overall detector in space upon mounting to the cryostat.

Item (1) has been previously discussed. Clearly, given the 1 mm positioning resolution we are trying to achieve, it makes a negligible constribution to the total alignment of the detector. We expect the alignment accuracy to be dominated by items (2), (3), and (4), and present in this and the following two subsections the means by which these aspects of the problem are addressed in the design. Items (3) and (4) are constrained, at least in part, by features that have been built into the design of the inner ring of the support structure. We discuss this aspect of the detector in this context in this subsection. Our proposed method of installing the detector, and the means by which the overall detector alignment will be maintained during this procedure, is discussed in Sec. 2.4.5. We defer the discussion of item (2) until Sec 2.4.4.

An end-on (r-ϕ) view of the center support ring for Layer 1 of the bottom half of the assembly is shown in Fig. 13. A magnified cross-sectional r-z view of the inner ring of the two layers closest to the cryostat, showing the detail of the nesting and the layer-to-layer connection, is shown in the left hand side of Fig. 14. We describe the significance of each of its features in turn below.

There are four types of holes in the center ring, with each performing a specific function:

1. In order to mount each of the detectors to the cryostat independently, each half must be constructed as a free-standing element. The first set of holes is used to bolt the layers in each half to one another. These are precision holes, and are labelled "layer fixation". The role of the different classes of these holes, denoted by $4a$, $4b$, $4a'$, etc., will be discussed in more detail below.

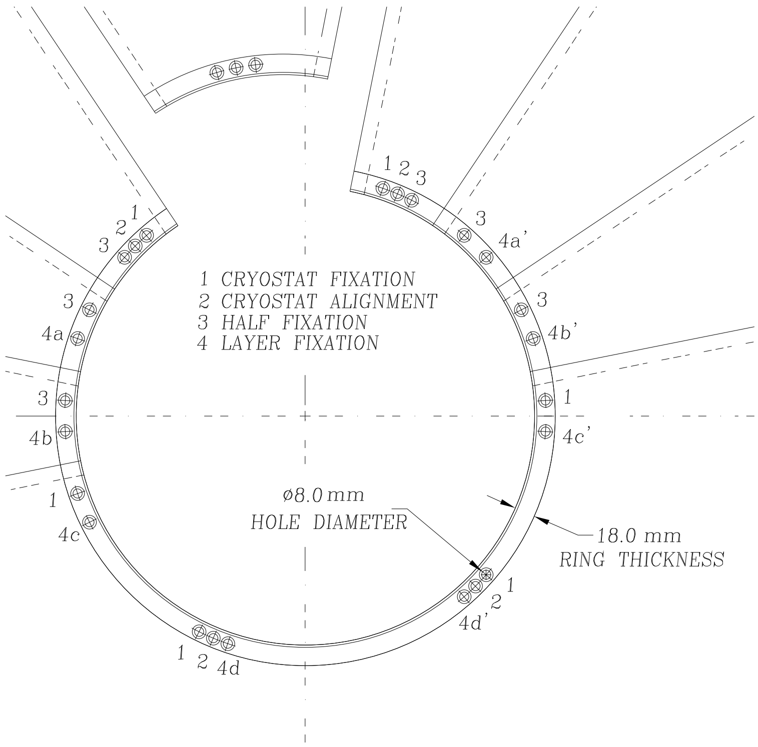

Figure 13: An r-ϕ view of the inner support ring for Layer 1 of the bottom half of the assembly. The different holes used for assembly, alignment, and mounting are discussed in the text.

2. As already discussed, we intend to mount one half (the lower one in Fig. 12) to the cryostat first, bolt it in place, and then mount the other half. There are a second set of holes that will accommodate dowel pins to ensure that the two halves are aligned with respect to one another. These constitute the second set of holes, which are also precision holes, and we label them "half fixation" holes.

3. For alignment on the cryostat (described in more detail below), it was decided that welding tight-fitting alignment studs on the cryostat that are as long as the preshower is thick (≈ 78 mm) would be prohibitive: maintaining the precise position in space in all three dimensions of such long, weld-affixed studs would be impractical. We've therefore opted to produce two types of holes for mounting the detector on the cryostat: one set of precision holes will enable the precision alignment of the detector on the cryostat by mating to a set of shorter (≈ 1.5", or 40 mm) studs that will be precision-welded to the cryostat, while another set of less precise through-holes ("sloppy" holes[2]) will allow the preshower to be bolted to the cryostat head by an additional set of longer studs (≈ 85 mm or more in length), also welded to the cryostat. These constitute the third and fourth set of holes, labelled "cryostat alignment" and "cryostat

[2]We note that our so-called "precision" holes will have an inner diameter that is 0.5 to 1.0 mils (15-25 μm) larger than the stud to which it mates; "sloppy" holes will have an additional 15 to 20 mils (300-500 μm). We currently expect all mounting and alignment studs to be 1/4" (6.4 mm) in diameter.

fixation", respectively.

As seen from Fig. 11, the inner support rings in each layer necessarily consist of two pieces. Each of them differs in size; we use the one in Fig. 13 (described above) to demonstrate the logic of the hole use and placement. Matching the nesting of the layers in Fig. 12 to the set of layer fixation holes in Fig. 13 helps to reveal the function of these holes. The layer closest to the cryostat and its neighboring layer are joined to one another through holes $4a$ and $4a'$. Were they not joined in such a way, the exposed wings of these layers (*i.e.*, the ϕ-segments closest to the mating gap) would not be fastened in any way to the rest of the half-structure. The connection is made by a pair of mating bolts that nest inside machined slots in the center rings of the two layers (see Fig. 14). We discuss the nature of these connections in some more detail in later paragraphs.

The next layer to consider is that of the absorber. It will consist of 11-mm-thick half-dome of lead to which a 1-mm-thick aluminum backing sheet has been fixed either by epoxy or by flat-head or other screw-type fasteners. (The flat head will allow perfect nesting between the lead layer and its neighbors.) The primary support for the lead in this sub-half will be provided by fixing it, along with its attendant aluminum backing skin, directly to the ribs beneath it. (Due to the overlapping modular structure, this option does not exist for the active layers of the detector.) The lead will be cut to an inner and outer radius identical to those of the small modules – its partner skin will be of the same inner radius as the other skins in the structure, and hence will be slightly larger in radius. The skin will thus provide additional material that overlaps the inner and outer support rings, by which more fixation points can be accessed. The inner ring for the lead layer will also be of a slightly different thickness – 11 mm instead of the 14.5 mm used for the active layers – to ensure that the layers mesh properly.

The next layer to be fixed to the remaining structure below is the layer of small modules closest to the lead. The holes marked $4b$ and $4b'$ perform this function. The actual fastening occurs by an analogous pair of mating bolts in the center rings of Layers 1 and 3. The layers in between (one layer of large modules, plus the lead) are simply sandwiched between the outer two by through-holes that these bolts pass through. We note, then, that our current plan is to fix all of the layers directly to the inner ring of the layer closest to the cryostat: the head of one of the layer-mating bolts in each layer are anchored into slots in this first layer (see Fig. 14). The holes labelled $4c$ and $4c'$ provide a similar function for the outermost layer of small modules in an equivalent manner. The two additional holes ($4d$ and $4d'$) will provide additional overall support for the half-structure, if it is needed.

The half-fixation holes accommodate nested dowel pins that will protrude from the inner ring in a direction parallel to the z-axis, and thereby establish the alignment of the two halves during installation. The heads of these bolts will nest within the inner ring in a manner identical to those being used for the layer fixation. Examination of the geometry of the nested halves helps to elucidate the logic behind this set of pins: guiding the upper half into the already-mounted lower half, each layer of the upper half maintains its proper orientation relative to its corresponding layer in the lower half by two of these so-called half fixation bolts (or threaded dowel pins). The two sub-halves of the detector are mounted to the cryostat successively, implying that the bolt heads that are buried in the lower sub-half, which is mounted first, will be inaccessible. A suitable means of anchoring these bolts in place in their slots has been designed. It consists of an allen screw buried in the center ring, oriented in the radial direction, that keeps the alignment bolts in place in their slots by compression against the outer rim of the holes in which they are housed.

We are currently designing for four cryostat alignment holes and six cryostat mounting holes, as shown in Fig. 13. Given the location of these holes in the figure, it will be clear that we intend only to precision-mount the lower half of the detector to the cryostat. The upper half will be precision mounted to the lower half only (through its half fixation holes), and not to the cryostat. The entire structure – both halves – will be fixed to the cryostat through the cryostat fixation holes, which penetrate the full thickness of the detector.

The details of the surfaces of the center ring, including the nesting of the mating bolts used in the layer fixation, are shown in cross section in Fig. 14. Layers 1 and 2 are shown in the left-hand drawing. The mating bolt pairs consist of two threaded pieces: one "male"- and the other "female"-type. The heads of the mating bolts lie against the inside of the machined inner surfaces of the holes in the center rings, allowing them to precisely nest inside the slot. Engaging the threads provides the compression by which two (or more) layers are held snugly together. The nature of the fixation of Layer 4 to the remaining structure below through its layer fixation hole is shown on the right hand side of Fig. 14. We note that the heads of both the "male" and the "female" bolts are anchored in the fourth and first layers, respectively, and that the remaining intervening layers are held in place only passively (at this ϕ-position) by through-holes that accomodate the fixation holes. We note that, at other ϕ-positions, each of the other layers will be held together directly by their own set of nesting bolts, thereby helping to ensure the structural integrity of the overall assembly. We expect to be able to find these mating bolts commercially in quantized lengths; if so, we will cut them to size for use during preshower assembly. If machining them ourselves is necessary, we believe we can make them simple enough so that the cost is contained within reasonable bounds.

The most important surfaces of the inner support ring are those at the inner and outer z-position of the ring. The inner radial surface of the ring defines the boundary between the Level 0 and the preshower, and provides no precision mounting or fiducial points. The outer radius has a similarly non-precision function. The surfaces of the rings that mate with other layers are important, however, and will be precision-machined. The "step" into which the rings in two layers mate helps to guide the layer-to-layer nesting (in z) and the relative radial orientation of the layers. The bolts define both the radial and the "clocking" (ϕ-orientation) of the layers relative to one another. The machining of the remaining surfaces at the inner and outer z positions also, in general, will define how well the layers nest, although other detector elements contribute here as well.

It is important to note, then, that all of the important layer-to-layer and cryostat alignment of the detector is established by the inner ring of the detector. It serves as the fulcrum of the support structure, and is the most expensive and precise support element. In fact, as will be discussed below, all of the precision mounting of the detector is dictated by this ring. The only additional connections to the cryostat will be at the outer radius, where the detector will be tacked to the

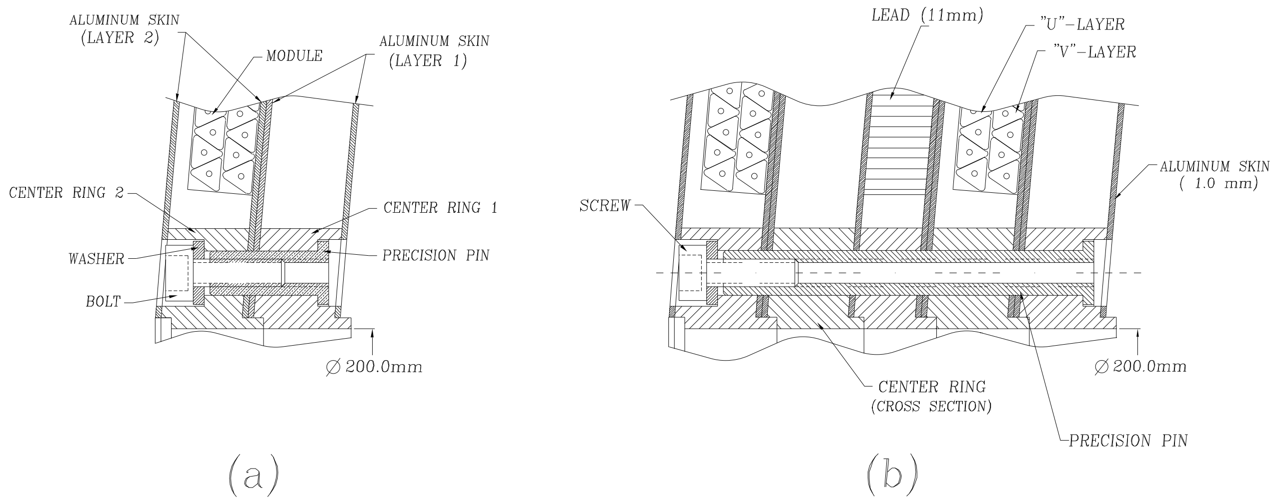

Figure 14: (a) An r-z view of the mating of the two inner support rings for the two innermost layers (Layers 1 and 2) of the bottom half of the assembly. The mating bolts are shown. (b) Same as left-hand figure, but showing a cross-section through the entire detector at that ϕ-section where the fourth (outermost) layer is attached to the rest of the underlying structure.

EC head through a few (probably four) oversized holes that will accommodate studs welded to the cryostat. (We note that only the outer rings for the layers closest to the cryostat will be able to be used for this purpose – the outer rings that help to support the MIP layers lie atop layers of active elements that make such attachment impossible. The outer rings for the MIP layers will be tacked directly to the absorber and the first layer of ribs beneath it.) There are therefore no additional precision holes or elements related to cryostat mounting at the outer perimeter – the detector is simply supported there at a few points.

As alluded to above, the inner ring in each layer consists of two pieces, and each piece must nest properly as the two detector halves are mated during installation. In order to ensure this, we intend to fabricate each ring from two different original template rings: the loss of material that would result upon fabricating both halves of each ring from the same original template would cause a mis-match between these halves. Fabricating these elements from two different original stock pieces enables the two mating surfaces of each ring to precisely mesh.

We now turn to the remaining aspect of the internal alignment of the detector: the means by which the modules in a given layer will be mounted to the support frame, and how the layers themselves will mate to one another.

2.4.4 Detector Alignment Issues II: Module Alignment

The intra-layer module alignment is intimately coupled to the means by which the detector will be assembled. We discuss the entire procedure in detail below.

A cross-sectional view of the assembly hardware is shown in Fig. 15. It consists of a series of aluminum angles that will be placed in appropriate positions to approximate the desired radius of curvature. (They are therefore inexpensive, and will need to be: our assembly procedure calls for three or four of these types of assemblies.) A reasonably rigid full sheet – of 1/8" (3.2 mm) thickness – will be spun during the skin fabrication, and will be used as the curved template on which the construction of the support frames will take place. (We call this sheet the assembly skin – see Fig. 15.) The support frame for each layer will be constructed as a stand-alone, precision structure on top of this skin, which simulates a dome of "negative curvature", as shown.

At the inner radius of the assembly rig, a precision-machined positioning ring is mounted. A precision milled inner "step" in this ring serves as the fiducial surface on which an alignment disk is laid. The alignment disk will serve to position and support an alignment arrow, which will be positioned at its geometric center and will point upward (see Fig. 15), precisely positioned in space. The assembly skin will be attached to the positioning ring by through holes. We emphasize that the assembly skin is used only as a cradle of the proper radius on which the frame is constructed and then removed; it is not part of the final assembly.

Each piece of the inner ring of the layer under construction are first fixed to both this positioning ring and the assembly skin. Two of the support ribs, separated in ϕ by 180°, are placed into their final position, using as a guide the corresponding milled slots in the inner ring that mate to the ribs. These first two "reference" ribs are precisely placed in space by the means described below, and their position will in turn be used to establish the position of the remaining ribs. Furthermore, our module installation scheme consists of positioning the modules in a given layer relative to the nearest set of support ribs. All of the internal layer alignment, therefore, is bootstrapped off of these first two ribs, and their positioning is critical. We first describe the means by which we establish absolutely the position of these reference ribs.

We use as a constraint the fact that a straight line in the (x,y) plane of the detector passing through the tip of the alignment arrow should also pass through the longitudinal bisector of each of these diametrically opposed reference ribs. Exploiting this, we intend to string a wire across the assembly in the (x,y) plane just at the tip of the alignment arrow. The reference ribs will be scribed along their length at their centers. A telescopic sight will be used to set precisely the position of the two reference ribs, and a few positions along their length (as well as at their ends, at the position of the inner and outer rings) will be marked and, later, drilled through both the ribs and the assembly skin. A set of bolts will be passed through the assembly skin and the ribs, locking the reference ribs precisely into place on a spherical surface of the appropriate radius. We note that each of the layers will then use this first set of fiducial bolts to establish the absolute position of their first two (reference) ribs.

Once the reference ribs are placed in position, the rest of the alignment within a given layer

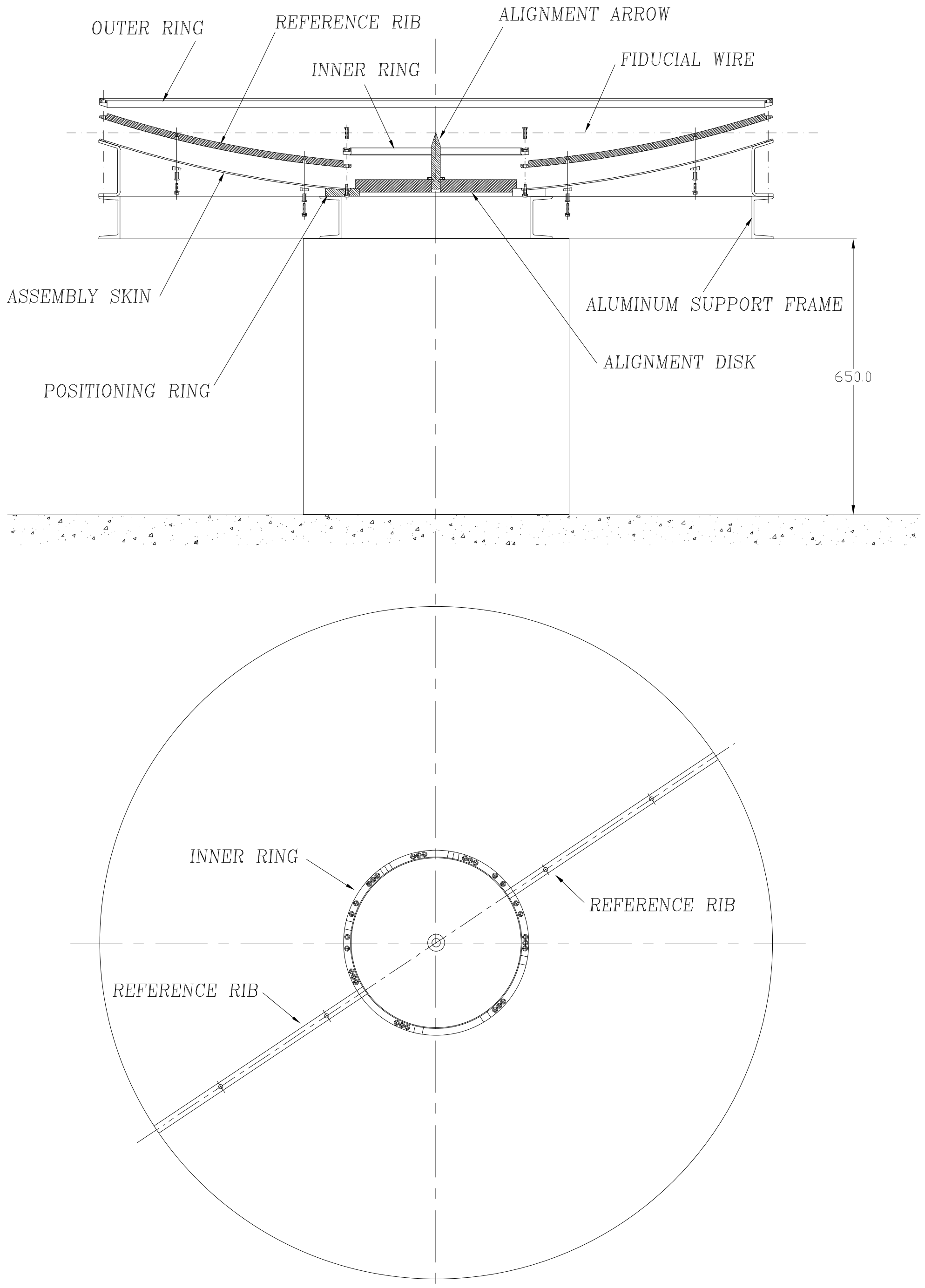

Figure 15: (a) Elevation of assembly rigging setup. The slice in ϕ is chosen so as to show the two reference ribs. The assembly skin, reference ribs, inner positioning ring, disk, and alignment arrow are all shown. (b) Top view of assembly, showing placement of precision elements: the reference ribs and the inner ring.

unfolds rather naturally. An alignment template is produced which will use the position of neighboring ribs to establish the precise position of those being installed. It will be a wedge-shaped, rigid aluminum plate that precisely subtends the appropriate 45° rib separation, and will contain an appropriate means of coupling to the ribs on either side so as to ensure precision mounting. The additional ribs will be added one at a time, fixing them at their ends to the appropriate milled slots in the inner and outer ring as the support structure is built up. The support frame of a given layer is thus built up successively and, after completion, exists as a fully integrated, stand-alone structure.

Once it is complete, the support structure, still in place on the negative dome, has a 1 mm (final) aluminum mounting sheet attached to its back, or concave, side. The reference ribs are unfastened from the assembly skin, and the entire structure – frame plus mounting sheet – is then turned over, placed on a similar assembly rigging setup with positive curvature, and bolted in place. The modules are then installed one by one using an analogous installation template that uses the adjacent pair of ribs as reference. The module installation template will be used to step through angular sectors of the detector, where appropriate markings for mounting and support hardware will be made. This last step was employed quite successfully during the construction of the test beam prototype. It greatly simplified the installation process, and was quite easy to use.

The means by which the modules will be aligned and fixed to the aluminum support sheets is shown in Fig. 16. Small stainless steel module alignment tabs will be hand-riveted to the sheet in precise positions at the four corners of the module. The positions of these tabs will initially be set by the module installation alignment template, which will be precision-machined at its four corners in order to properly register the position of the tabs. The tabs each have a precision notch cut out of them, into which the corner of the module will nest. This determines the position of the module. A clamping bar will screw into a threaded tube that will be fixed to each of the tabs (see Fig. 16): this will hold the module in place. The clamp will be positioned in the 2.5 mm space between the module and its neighboring upper skin. This space is needed for routing the WLS fibers from the outer edge of the module to the outlying connectors (see Sec. 3.3.2).

We note that such a mechanical means of module fixation is highly desirable, as we anticipate the need for a large degree of flexibility and reversibility during the cabling of the modules. Our experience during the prototype R&D also taught us that forming a reliable, robust glue joint between the module and an aluminum substrate was difficult to do. For these reasons, we prefer such a mechanical clamp to gluing the module directly to the skin with epoxy or other adhesive. Much of this system (rivets, threaded tubes) can be fabricated from commercially available products; the remaining pieces (tabs, clamps) can be machined for a reasonable cost.

Having built up a full layer of the detector, the modules will be cabled, tested, and covered with a protective aluminum sheet. (This protective sheet will remain in the final detector – the geometry of the overall device would result in exposed modules in two of the four layers without this protective skin. At a very small cost in thickness, we have opted to provide one for each layer for protective purposes.) As layers are completed, they will then be built up on an additional assembly that has an inner radial ring containing precision dowel pins oriented parallel to the z-axis that,

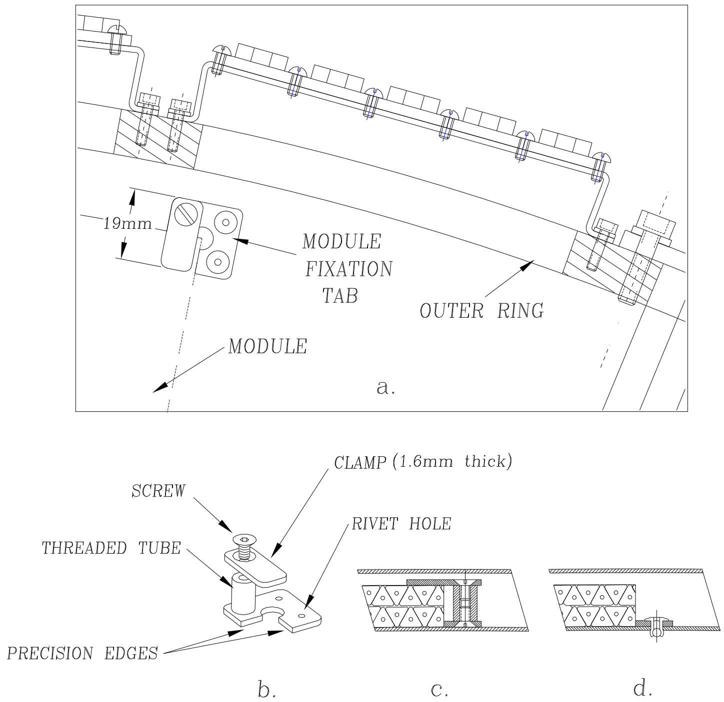

Figure 16: (a) An r-ϕ view of the outer edge of a layer, showing the stainless steel module fixation tab. Each module is held in place in an identical manner at each of its four corners. (b) Details of the fixation tab. (c) Side view of one module at the position in ϕ at which the clamp is located. (d) Same as (c), but at a ϕ position where the rivet joint to the sheet is shown.

using the precision mounting holes in the already-installed inner rings of each layer, will ensure that the layers are mounted properly relative to one another. The layers will be bolted together in the manner described in the previous section.

Our intention is to fully assemble the support frames for each layer, and the detectors as a whole, without any modules as soon as the pieces are returned from the shop. Any needed adjustments or retro-fitting will be done at this point. We also intend to mock the full installation of the detector onto the cryostat at BNL, mounting the two completed halves of each detector to one another. Again, any needed alterations or re-fitting of components will be made during this period. This last step will also be performed in a vertical position, to make sure that no unexpected distortions of the overall structure(s) result, and that the integrity of the mounting alignment scheme is preserved. We anticipate the need for some surveying here.

Having discussed most of the details of how the detector comes together, we present in the next subsection the last important component in the sequence of steps that define the FPS assembly and installation: how the detector alignment will be established and preserved during its installation on the cryostat.

2.4.5 Detector Alignment Issues III: Installation

We focus in this subsection on the means by which the FPS will be mounted to the cryostat heads. We note that, in general, the heads of each of the ECs will deviate from the nominal sphericity by some amount. This deviation can result in head distortions that can be as large as about 1/2" – a non-negligible number, given the alignment accuracy we are trying to achieve. Although a few regions of the head have been measured in detail, it is unrealistic to assume that the shape of the entire area to which the detector will be mounted can be understood in any great detail prior to installation. Experience has shown that surveying the head, with the goal of producing a full contour map, yields results that take many months to understand and, in the end, are usually not wholly unambiguous. We have therefore developed an installation procedure that presumes that the details of the shape of the heads are unknown. We also assume that no surveying will be able to be performed during installation which, in the worst case, will be done in the collision hall. We present below our proposed procedure, which was developed in conjunction with Fermilab personnel, who will play an integral role in the mounting of the FPS.

We will design and machine another precision installation template plate that will contain the same cryostat alignment and fixation holes as those in the inner ring of the detector. This stainless steel plate will be used to guide the welding of the mounting studs onto the cryostat head. We intend to mount the preshowers so that the detector is centered on the beamline: the beam pipe will therefore provide the reference for all of the detector alignment relative to the DØ coordinate system. (We will assume for this discussion that the beam is centered in the beampipe in x and y.)

With the help of survey marks, the installation plate will be placed on the cryostat in the proper (centered) position while the ECs are in the assembly hall. The ϕ-position of the ring will be established – again, by surveying – using the alignment holes in the ring. It is important as well that the studs be welded to the cryostat so that they lie parallel to both the beamline and to one another. All three spatial dimensions will therefore be surveyed during the mounting of this element. Given the possible deviations from sphericity of the head, the plate may not be able to be mounted perpendicular to and centered on the beampipe, and still remain flush on the face of the cryostat. We intend to mount it as close to cryostat as possible, while still respecting the alignment constraints we are after.

We have mentioned previously (see Sec. 2.4.3) that the cryostat alignment studs will be approximately 1.5" in length. The thickness of the plate must be sufficient to ensure that the proper orientation of the studs in space after welding is maintained. We believe that a thickness of 1" for the installation plate will be sufficient. It will also contain access points for the welding machine, so that the studs can be welded on with the plate in place. After welding on both the cryostat alignment and fixation studs at the inner radius, the plate will be removed. The position of the studs will be found by detailed surveying after welding, and full spatial information will be available for each of them.

Although the above means of welding the studs in position guarantees us that the detector will be properly positioned in ϕ and that it will lie in the proper plane relative to the z axis, the final position of the detector in z cannot acceptably be established by the above procedure without further refinements. Irregularities in the detector shape, the head shape, or both implies that the detector will not nest neatly on the cryostat shell: in general, it can only be expected to touch the head at one, or perhaps a few, points. Moreover, the irregularity of the weld joint at the interface of the cryostat and the studs cannot be relied upon to establish "stops" for the detector as it is mounted: the innermost (*i.e.*, closest to the cryostat) z-position of the usable portion of the studs may not all lie in a plane perpendicular to the beamline. (Our planning assumes that the detector will be able to be placed no closer than $\approx 1/8$" from the cryostat head – even if the head and the FPS are found to be perfectly spherical – due to irregularities of the weld joints.) It is necessary, therefore, to establish some means of setting the z position of the device during mounting.

The FPS will be lifted into position and mounted on the studs. If we have to install the detector in the collision hall, we will probably have to design some simple lifting fixtures that will enable us to support the detector off of the muon trusses or some other appropriate overhead points. These will be developed as the need arises. From the surveyed position of the junction of the weld joint and the cryostat head, we will be able to compute the plane perpendicular to the z axis that is closest to the cryostat head and still contains a usable portion of each of the studs. (By "usable", we mean that portion that is uncorrupted by the welding procedure, and can therefore be relied upon for proper detector mounting.) This defines, then, the z-position of the detector that we would like to establish, provided there are no interferences between the head and the FPS at outer portions of the detector. Shims of the appropriate length will be added to each of the studs to establish this plane, which will be used as reference. In general, of course, each of these shims will be of different thickness. However, as already discussed, mechanical distortions imply that we cannot rely on these shims to define the proper z position of the detector. Our means of mounting the detector will therefore consist of the following steps:

1. Since the thickness of the detector will be well-known, one can calculate (or measure) the nominal z-position of the detector that is closest to the interaction point. This point will be at the inner ring. This position will be calculated or measured for that position of the FPS that includes the nominal shims described above. We call this point along z P1, and it is used for reference.

2. The lower half of the detector is mounted on the outer length of the studs. It is assumed that the FPS is free-standing at this point – *i.e.*, it does not touch the cryostat head anywhere. All studs will have to be of sufficient length to account for reasonable offsets of the FPS from the EC head at this point, and still allow additional motion of the detector along z as the final adjustments are made.

3. The half-detector is translated in z until any point (or portion) of the detector touches the cryostat head. Its position here, which we call P2, is noted.

4. The difference P2$-$P1 gives the size of the shims that will be needed in order to mount the detector in the desired position.

5. The detector is dismounted, shims of this size are placed at each stud, and the detector is remounted.

6. The procedure is iterated, if needed, after which the detector is bolted on to the cryostat using the (longer) fixation studs.

The utility of the procedure is largely contained in the last two steps: we are guaranteed to have placed the detector in the proper position in z – even taking into consideration distortions in either the cryostat head or the FPS – by using identical shims everywhere. The position of the detector in all three dimensions is thus set properly, with all surveying having been performed prior to installation. The amount of surveying in this scheme is also kept to a minimum.

Our design dictates that the upper half be mounted after the lower half is in place. As already mentioned, dowel pins in the exposed portions of the inner rings on the lower half will properly position the detectors relative to one another: since the lower half is already properly positioned at this point, this implies that the upper half will be oriented properly as well. Most of the fixation studs at the inner ring will be used to mount both detector halves to the cryostat.

We anticipate applying similar techniques to pre-establish the position of the four studs that will be used to tack the FPS in place at its outer radius. We note that the (over-sized) holes in the outer ring to which they mate are not precision elements, and will not be used to establish the position of the detector – they are used only for support. In any case, we have not yet decided whether to pre-weld these outer studs, or position them *in situ* during the mounting. In this latter case, we would anticipate marking a few points at the outer radius after the detector is mounted properly (*i.e.*, steps (1-5) above are completed), removing the detector an additional time, welding on the outer studs, and replacing the device for final mounting.

We note that all assembly of the two halves done at BNL will utilize the same template that is used to position the inner alignment studs on the cryostat. Before and after the assembly of a given layer, we will stack the assembled individual layers of that sub-half in their final positions on an assembly dome. The final position of these layers relative to one another will be established by a mock-up of the alignment studs at the inner ring of the detector (perhaps some precision pins.) The same template that was used to establish the positioning of these studs on the cryostat prior to welding will be used to reproduce their positions for this mock-up. Any needed adjustments to the alignment will be made at this point.

After a given sub-half of the detector is assembled, it will be suspended vertically in the rotated position (in ϕ) necessary for installation at DØ. We anticipate that we will need to design a device that will properly attach the sub-half to whatever suspension mechanism will be available in the collision hall (crane, cables, etc.) The design of such a coupling device will be considered during the next few months, as all of the details of the detector and assembly are finalized. In any event, we will fully assemble and join the two halves of the detector in a vertical position at BNL before the detector is shipped to FNAL: that is, both sub-halves will be bolted to some facsimile of the EC head and the corresponding mounting studs, and pinned and bolted to one another in the method described above. This will ensure that, in principle at least, all modifications necessary for aligning and mounting the structure on the cryostat will have been performed in their entirety prior to shipment of each detector half to Fermilab. We consider this step a very important part of the overall construction procedure. Although experience has shown that some new features will make additional adjustments necessary at DØ, we are trying to develop a design and assembly procedure that will limit the number and magnitude of these *in situ* adjustments.

Finally, we mention that, in order to absolutely determine the position of the modules in each of the layers, survey marks will be provided at a number of points in each layer. In case we have the opportunity to establish the position of the installed detector at DØ by survey, we also intend to include at least three survey marks on the external skin(s) of each sub-half of FPS-North and FPS-South.

3 Light Connections and Signal Processing

3.1 Readout Scheme

The demands placed on the readout system for the FPS are based on the fact that the detector will be used efficiently to identify and characterize both minimum ionizing signals and electromagnetic showers. This requires that the readout system be able to handle the signals over a reasonably large dynamic range. A block diagram of the FPS readout system is shown in Fig. 17. We note that both preshowers, central and forward, will be using the same readout and trigger electronics. It is possible, however, that differences in the particle rates and energy spectra in the two regions may require that some of the parameters – *i.e.*, charge division capacitors – be different in the two systems. The readout has been designed with enough flexibility to quite comfortably adapt to the needs of both detectors.

The major elements of the readout system for the FPS consists of Visible Light Photon Counters (VLPCs), the Scintillating Fiber Tracker trigger chip (called the SIFT chip), and the SVX-II readout chip. Photons from the clear fibers are converted into electrical signals by the VLPCs and digitized by SVX-II. The intermediate SIFT chips are introduced to provide fast Level 1 trigger signals; the SVX-II digitization speed is too slow to generate signals for a Level 1 trigger decision. The SIFT also drives the analog signal to the SVX-II chips downstream. The SIFT chip contains a dual-range discriminator for which the threshold may be set within a pre-determined range of values. (At the moment, the proposed discriminator ranges are 5-80 femtocoulombs (fC) and 30-300 fC. The relevance of these values will be made clear in subsequent paragraphs.) The corresponding TTL output will be sent to Field Programmable Gate Arrays that will implement the trigger logic. In addition, the analog line of the SIFT attenuates the signal by a programmable factor of either 2 or 4 prior to shipping it off to the SVX-II for digitization. We point out that this readout system has generally been designed to detect small, MIP-like signals for tracking systems (silicon detector and fiber tracker) – it must be suitably adapted for use in the showering layers of the preshower, which must be able to characterize signals with large pulse heights.

In order to fully adapt the readout scheme for use with the preshowers, we are implementing the scheme illustrated in Fig. 17. The photons liberated from each scintillator strip will be wavelength-shifted from the blue (wavelength of 430 nm) to the green (510 nm) by WLS fibers, and then routed through the clear waveguide to the VLPCs below the cryostat. The resulting electrical signal at the output of the VLPC channel will be charge-divided into two arms: a high-gain (or MIP) and a low-gain (or showering) readout arm. Each arm of the divided signal is shipped to its own independent set of SIFT and SVX-II readout channels, where the signals are processed for triggering and digitization. We emphasize that the optical signal from each strip is converted to an electrical signal and amplified by *one* VLPC channel, but that after the bifurcation resulting from the charge-division, the high- and low-gain arms are each handled separately. There are thus twice as many SVX readout and SIFT trigger channels as there are VLPC channels for the preshowers.

We expect about 15 photoelectrons (p.e.) per MIP to be liberated at the VLPC for minimum

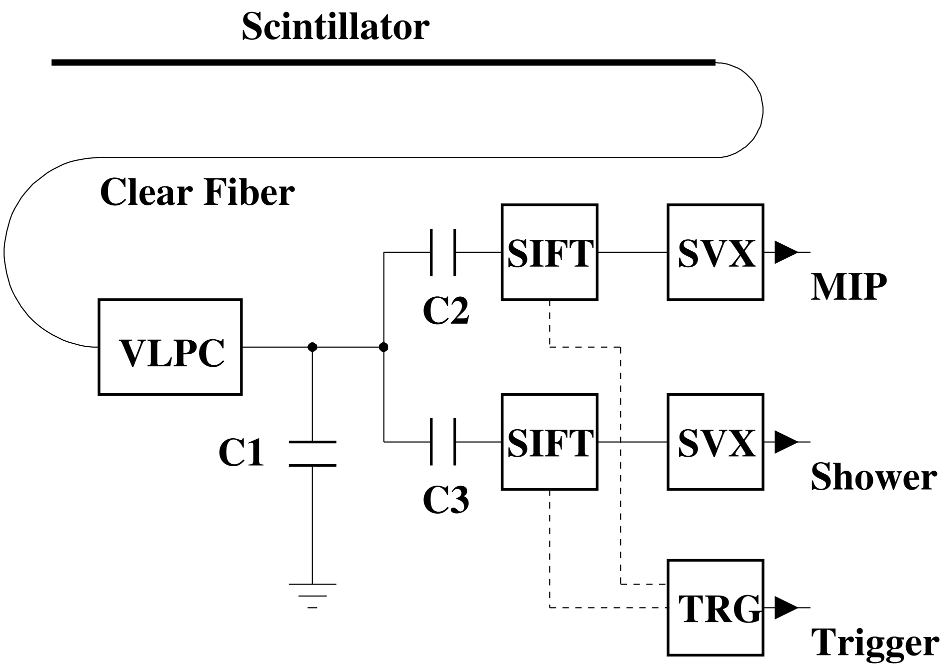

Figure 17: Block diagram of the FPS readout system.

ionizing particles that traverse $\approx$ 5 mm of scintillator. The gain of HISTE-VI VLPCs has been measured to be about 40,000 [17]. Combining these numbers, we get:

$$15 \text{ p.e.} \times 1.6 \times 10^{-4} \text{ fC/p.e.} \times 40,000 \approx 100 \text{ fC/MIP}. \tag{1}$$

The energy distribution in the strip with the largest pulse height (called "stripmax") for 50 and 5 GeV p_T electrons, obtained from Monte Carlo simulations, is shown in Fig. 18. The mean energy deposited in stripmax in the forward region will be greater than that deposited in the central region for electrons of the same p_T because the incident electron energy is higher. (As a benchmark, we point out that the ratio of the energy (E) of a particle to its p_T at $\eta = 2.0$ is $\approx$ 4:1). The maximum p_T for electrons emitted from W or Z decays (those at the Jacobian edge) is $\approx$ 50 GeV, or $E_e = 200$ GeV at forward pseudorapidities. To be conservative (and to simplify the discussion), we take 100 MIPs as a representative value for the energy deposited in stripmax for 50 GeV p_T electrons; using Eqn. 1, this corresponds to 10^4 fC. Naturally, for electrons at lower p_T – which are important for b-tagging, supersymmetry searches, and other processes – the amount of charge collected will be less. For electrons of 5 GeV p_T, for example, Fig. 18 indicates that a factor of $\sim$ 3 less charge – or $\approx$ 3,000 fC – is deposited in stripmax in the showering layers.

There is therefore a difference of a factor of $\approx$ 100 between the energy deposited in stripmax by a MIP and that by the shower of a highly energetic electron. The values for the charge division

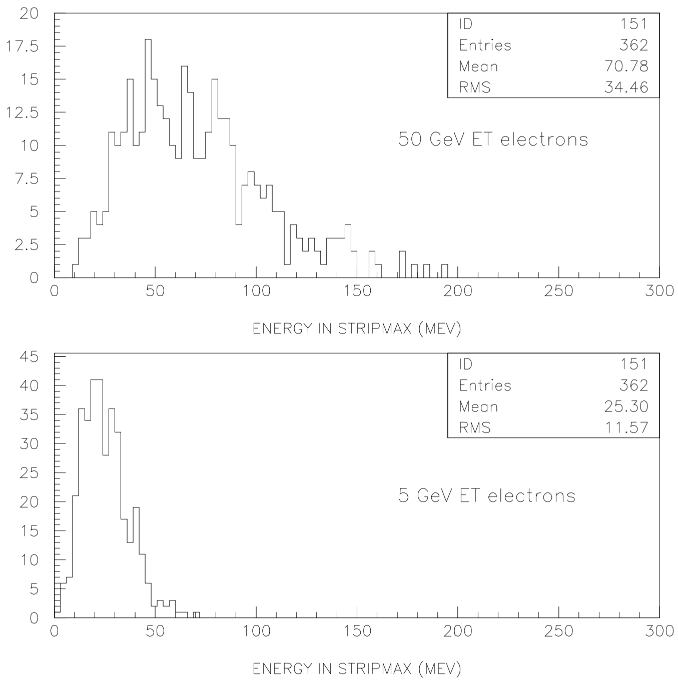

Figure 18: Distribution of the maximum energy deposited (in MeV) in a strip of the FPS for electrons of two different p_T values. Strips used for this Monte Carlo study had a 5-mm-square cross section. A MIP deposits about 1 MeV in a strip.

capacitors will be chosen so as to utilize as much of the dynamic range of the system as possible for both the high- and low-gain arms of the SIFT and SVX readout, subject to the constraint that the system not saturate at too high a frequency. It is also important that the charge not be divided too finely so as to demonstrably degrade the signal-to-noise. One also wants to keep the resolution fine enough so that single MIPs – and, perhaps, even single photoelectron peaks in the high-gain channels – are resolvable. One also wants to be sure that the system is optimized for both high- and low-p_T processes.

We use some concrete numbers in order to illustrate some of the more important considerations that influence the choice of charge-division capacitors. The random noise in the SIFT chip has a width of about 0.7 fC. Taking a generous 7-sigma above this as a reasonable trigger threshold, this gives a minimum trigger threshold of 5 fC, or 5% of the expected maximum signal from a MIP. We emphasize that this 5 fC minimum is at the input to the SIFT, after charge-division. In Fig. 17, choosing values of C1=200 picofarads (pf), C2=120 pf, and C3=5 pf, for example, would route $\approx$ 40% of the charge out of the VLPC into the high- and low-gain arms. At the junction just prior to the charge division, therefore, one MIP corresponds to 40% $\times$ 100 fC/MIP = 40 fC. Roughly 95% (5%) of this charge would travel through the high- (low-)gain arm, which would result in approximately 40 (2) fC/MIP at the input to the SIFT for each of them.

The triangle geometry of the strips suggests that the minimum amount of scintillator that a particle traverses in a nested (u or v) layer is half of the full height of the triangle. Taking into account Landau and noise fluctuations, one would like to be able to establish a trigger threshold for MIPs that is efficient at roughly half of this value. This corresponds to $1/4 \times 40$ fC/MIP = 10 fC in the high-gain arm after charge division in this example. This is consistent with the minimum acceptable threshold computed from the noise considerations above. For the low-gain arm, a 5 fC lower limit on the threshold corresponds to 2.5 MIPs – comfortably below the lowest value of 3-5 MIPs that we expect to apply for isolation determinations at Level 1, if they are needed.

The analog output of the SIFT attenuates by an optional factor of either 2 or 4. Choosing the former, the SVX will see 20 fC/MIP at its input for the high-gain channel. The full range[3] of the SVX is ≈ 150 fC, which therefore corresponds to 7.5 (75) MIPs full scale for the high- (low-)gain arms. Both of these values are quite reasonable. The full scale for the SVX corresponds to 256 ADC counts, which thereby gives 34 (3.4) ADC counts/MIP for these two legs, respectively. The readout resolution in the former is fine enough to resolve MIP peaks, which is important for calibration. We emphasize that the numbers used above are simply meant to provide a concrete illustration of how the readout system will be used: we believe, however, that there is enough flexibility in the system to allow us considerable leeway in designing a suitable readout system with all of the needed characteristics.

The charge division capacitors will be soldered onto the front end boards individually, and by hand, using technical manpower. One clearly wants to avoid iterating the procedure: for the FPS, there will be $15{,}000 \times 3 = 45{,}000$ capacitors to install. Such considerations have helped to motivate the beam test at Fermilab during the summer of 1997: one of the primary goals here was to obtain a few benchmarks of the expected shower profiles for electrons at as many different energies as possible, using a close facsimile of the final readout chain, and to compare them to Monte Carlo. (We note that, before this test, neither the scintillator technology nor the readout scheme had previously been tested for showering particles – the response of the system to MIPs, using cosmic rays, had been extensively studied in an earlier test [3, 8].) Despite the extreme levels of coherent noise at NWA, the shower profiles for 50 and 70 GeV electrons we were able to extract agree well with the Monte Carlo (see Sec. A.2 and Ref. [23]), giving us a measure of confidence that the Monte Carlo can be used as a guide for the final determination of the values of the charge division capacitors we intend to use, and that the readout scheme contains no fundamental difficulties. Another beam test, for which the final version of all electronics components (including the SIFT) will be available, is under consideration for Fall, 1998 at Brookhaven.

3.2 Fiber Connectors

The preshower detector readout is effected through the coupling of WLS fibers to clear fiber waveguides which together transport light to remote VLPCs. This requires accurately matched and

[3]This is the full dynamic range per beam crossing. The dynamic range integrated over many crossings, after which a reset is required in order to re-activate the chip, is ≈ 450 fC.

efficient connections between the two different fiber types and in the fiber-to-photodetector coupling. The main requirements are to provide reproducible light transmission greater than 95%, and long-term stability to within 1%.

3.2.1 Early Connector R&D

Extensive R&D efforts were performed by our DØ collaborators at the University of Illinois at Chicago (UIC) to fulfill these requirements [7]. The resulting UIC design serves as a basis for light connections to be used for the Scintillating-Fiber Tracker, as well as for both the Central [8] and Forward Preshower detectors. Here, we outline the main effort of the study, and the details of the light connector chosen for implementation in the FPS.

The UIC study consisted of designing and fabricating various connectors, and testing them in quantity for transmission characteristics. The group tested a total of eight different v-groove connector pairs in the process of optimizing connector performance. (The "v"-shape refers to the shape of the grooves in the connector into which the fiber is inserted.) Two pairs of v-groove connectors were designed to study both 0.965 mm and 0.835 mm diameter fibers. Here, connections were based on a one-to-one type (0.965-mm-to-0.965-mm fiber diameter matching) and a step-up type (0.835-mm-to-0.965-mm fiber diameter) of coupling. The 128 channel prototypes were all machined from black Delrin plastic. For both assemblies, multiclad fibers made by Kuraray [12] were used, rather than single-acrylic-clad fibers, primarily because the refractive index n of the fluorinated polymer ($n = 1.42$) is observed to be lower than that of acrylic ($n = 1.49$), resulting in a larger total internal reflection light capture cone and a brighter fiber (longer attenuation length).

Prior to gluing the fibers in the connectors, the front face of each connector was wrapped with clear plastic sheeting to prevent glue from flowing over the side. The connector was then held fixed with the front surface facing down. Unpolished fibers were individually routed into the v-grooves, allowing them to protrude a few millimeters beyond the face. Several epoxy adhesives were tested for best adhesion of the clear fiber to the connectors. Bicron BC-600 epoxy [26] was chosen for its durability, and because it is specially formulated for gluing plastic scintillator. After fiber insertion, epoxy was injected into the glue pocket located on the back end of the connector. The assembly was allowed to cure overnight. Finally, the fiber/connector assembly was placed in a clamping jig and inserted into a special diamond fly-cutting tool, designed and fabricated at Fermilab [9], for polishing. A microprocessor allowed control of rough-cuts and final cuts. Each connector required roughly eight minutes to polish.

After assembly, optical grease [10] was uniformly applied to the connector joint of the fully machined prototype connector, and the light transmission was measured [7] to be $(98 \pm 2)\%$. The observed light transmission for a one-to-one connector assembly appears in Fig. 19. The measurements were made with a green LED point-source, using optical grease as a couplant. The theoretical maximum transmission based on Fresnel's reflection formula is 99% for coupling with optical grease with a refraction index of $n = 1.40$. Both the one-to-one and the step-up connector pairs yielded the same average light transmission, and therefore a design using the simpler one-to-one geometry has been chosen.

Individual connectors have been produced by injection molding rather than machining in order to allow faithful reproduction in quantity. Transmission measurements for injection molded connector assemblies (using, however, machined alignment holes) yield an average of 95% transmission efficiency when optical grease is used as the couplant. This slightly lower transmission is due to alignment errors in the machining; in the latest version of the connector, the alignment holes are included as part of the connector mold.

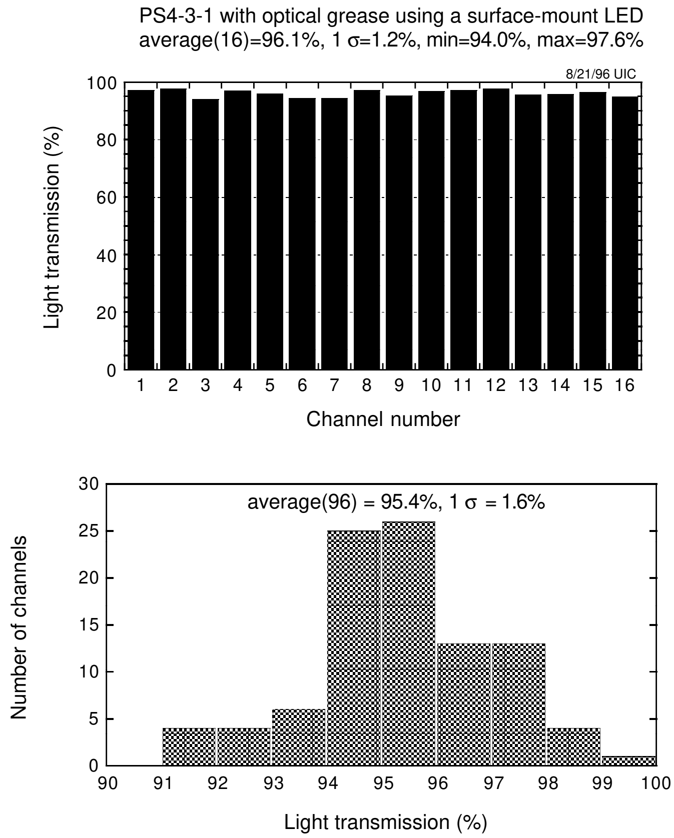

Figure 19: Observed light transmission for each channel in a 16-channel one-to-one type connector assembly (a), and the measured distribution of fiber channel transmissions (b). Both distributions yield, on average, 95% light transmission through the fiber/connector interface. The connector assembly uses 0.965 mm to 0.965 mm diameter fiber connectors with optical grease as couplant.

Several effects contribute to the reduction in light transmission in connectors. The major source of light loss is due to axial misalignment: for a 0.965 mm diameter fiber with a 1 mil (25 micron) misalignment at the connector joint, the ratio of the overlapped area to the full cross section is

0.967, equivalent to a 3.3% light loss. Thus, in order to achieve a light transmission greater than 95%, the misalignment must be kept below 1.5 mils (38 microns). To meet this specification, the molded connectors must be made with sufficient accuracy, requiring careful design of the mold. Moreover, alignment pins mounted on the connectors serve precisely to register the mating halves of the connector pair. Angular misalignment is not found to be a problem for multichannel connectors. Variations in fiber diameter of about 1% at the joint result in a light loss of approximately 2%. However, fiber manufacturers such as Kuraray are able to control the variation in fiber diameter to within 1%, thereby avoiding significant light losses due to this effect. Fiber ends were inspected and found to be free of blemishes after the cutting/polishing with the diamond fly-cut tool.

Gaps between the connector joints must also be minimized. Light transmission between two 0.965 mm fibers decreases linearly by about 2% for every mil of air gap, up to a gap size of 0.5 mm (20 mils). Using Fresnel's reflection formula at the connector/gap interface, the light transmission between fibers with a polystyrene core having an index of refraction $n = 1.59$ is roughly 90% through air, and about 99% through optical grease having $n = 1.40$. A non-fluid couplant must therefore be used. With its high viscosity, optical grease works well in a temperature-controlled environment; its counterpart, mineral oil, tends to flow quite readily. Such a propensity for flowing means that gradual light loss will occur when mineral oil is used. In fact, measurements indicate that the initial light loss when optical grease is used is $\approx (1 \pm 1.3)\%$, and that this loss increases to only 2% after a one-year period. For the same initial yield, the transmission through mineral oil drops some 5% within a few days. For these reasons, we intend to use optical grease [10] as a couplant in connector joint gaps.

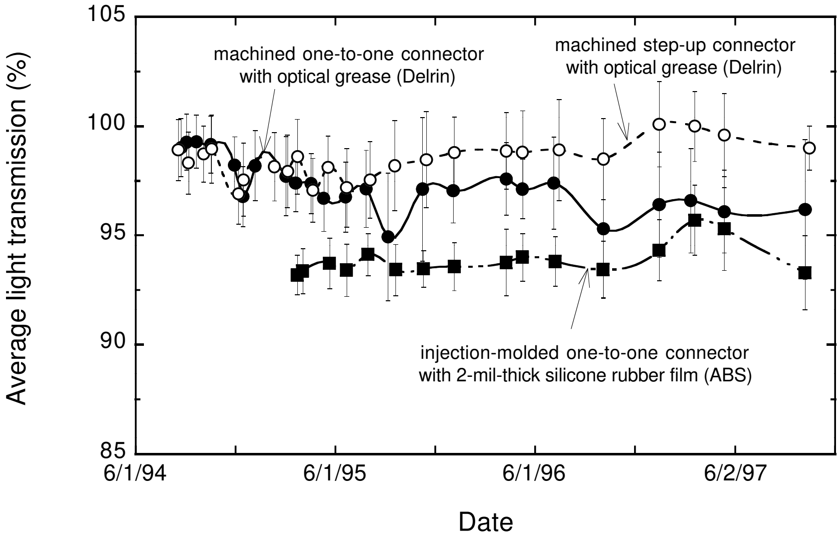

Figure 20: Long-term stability study of light transmission using prototype preshower connectors.

Since the lifetime of the upgraded DØ detector is expected to exceed five years, the stability of light transmission must be monitored. The long-term transmission data for various connector types is shown in Fig. 20. The error bars indicate the *rms* width of the measured transmission distributions, which represent 128 measurements each. The data show a gentle decrease in transmission over time for the machined one-to-one type connector for which optical grease was used. More stable results are obtained for the injection-molded version, although the average yield is somewhat less. Minor variations in all three curves are believed to be due to temperature fluctuations during the test, which caused a slight flow of optical grease. In fact, over the one year period during which they were monitored, the temperature was known to have varied between 18°C and 25°C. In any case, the light transmission for the injection-molded connectors is observed to be stable for eight months to within $\approx 1\%$.

3.2.2 Sixteen-Channel WLS-to-Clear Fiber Connectors for the FPS

Like their counterparts in the CPS, the FPS WLS-to-clear fiber connectors will be injection-molded sixteen-channel connectors made from black Delrin plastic. The injection mold for the FPS has been developed by the UIC DØ group following guidelines set by spatial and other constraints specific to the FPS. The mold will be produced by the UIC machine shop. All three FPS module types – large, small, and "special" – will use these connectors, with the only difference being the number of connectors required for each. We note that both the clear and the WLS sides of the detector-end connectors will be produced by UIC. Naturally, both sides will be injection-molded.

Initial connector pairs will be tested at UIC for light transmission following the procedures described earlier. The connector, shown in Fig. 21, has dimensions 6.4mm $\times$ 22.0mm $\times$ 7.0mm, and contains a matrix of 4×4 fiber channels. (The connector will be mounted so that the spatial direction corresponding to these dimensions are $z \times \phi \times r$ – see Fig. 21.) The design is similar to that of the CPS connector, but reduces the inactive area at the outer boundary where the connector is mounted to the plate on which it sits. Each connector groove holds a 0.835 mm diameter WLS fiber. The connector has a compact channel-to-channel spacing of 1.5 mm, which leaves a sufficient amount of material between the fibers to ensure mechanical stability. A glue pocket in the rear-end of the connector allows for convenient gluing of fibers. The Bicron BC-600 epoxy described earlier will be used as the adhesive for fixing individual fibers in the connectors.

A square 4×4 fiber array has been chosen over the 2×8 array of the CPS connectors, thereby reducing the overall length from 33 mm to 22 mm. This was of particular importance in the FPS, as WLS cabling constraints clearly preferred a scheme in which the connectors were mounted in a single row in z; in order for the fibers of Layer 1 to negotiate the run over the face of the outlying ICD, the connectors need to be positioned as far away from the cryostat face as possible. One layer of connectors helps significantly to reduce the potential stresses on the fibers, and particularly on the delicate fiber/connector interface. Maintaining this one-row geometry was found to be impossible with the old 33 mm CPS version. We feel that the new connector represents a decidedly more intelligent use of space for the Forward Preshower detector.

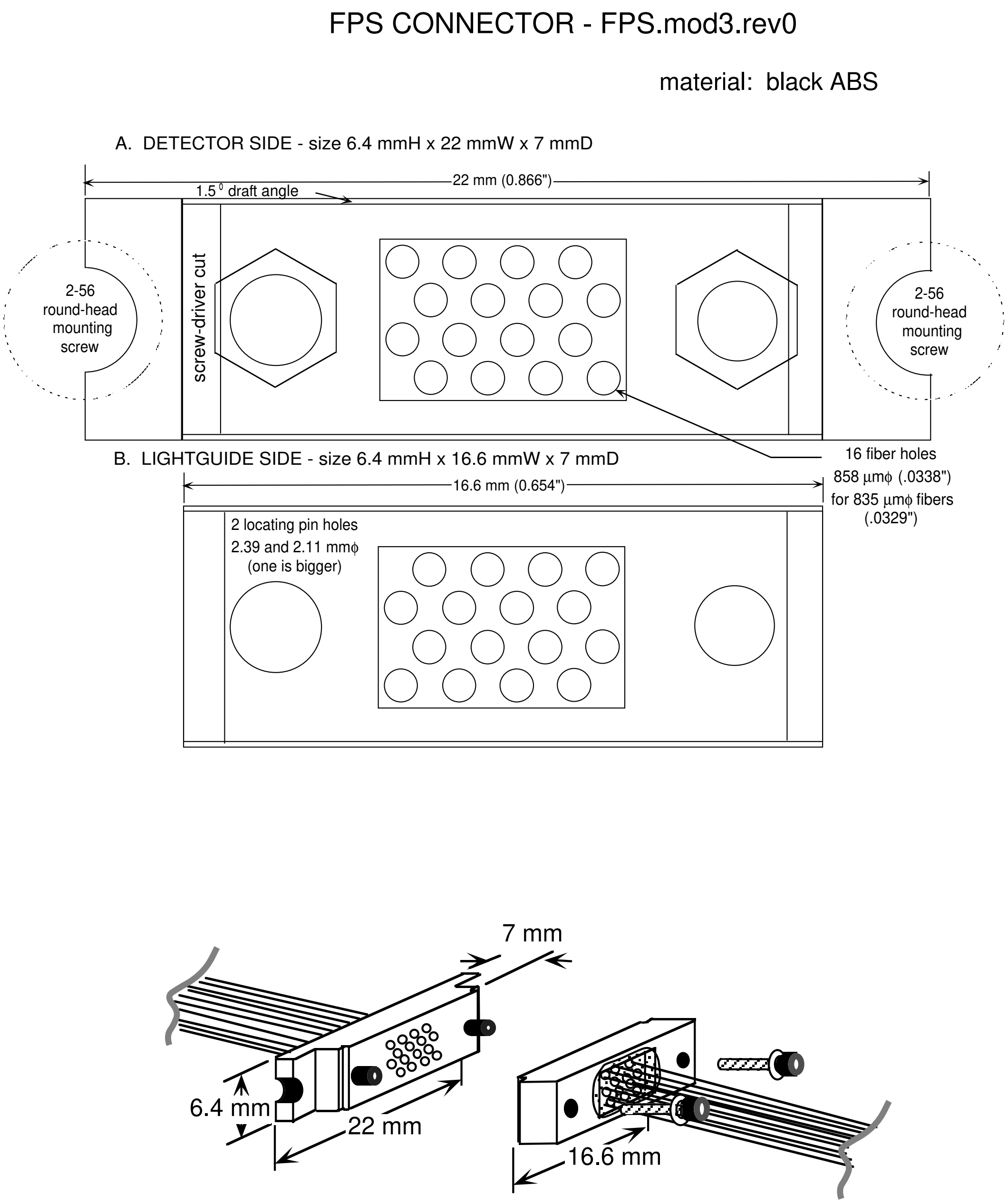

Figure 21: Layout of the 16-channel FPS connector, showing the front-view (top) and the 3-dimensional view (bottom).

For the large (small) module, connectors are located at the detector rim in two groups of 9 (7) connectors on either side of the module, for a total of 18 (14) connectors per module. The "special" module will require 5 connectors per side, for a total of 10 connectors per module. Two views of the connector locations for FPS Layer 1 are shown in Fig. 22 and Fig. 23. Connectors are mounted to an outer stainless steel or aluminum support bracket with round-head 2-56 screws. We note that, in order to conserve space, each mounting screw serves to fix two adjacent connectors to the bracket. The connector nearest to the upper edge of the module lies ≈ 40 mm from the module edge. This distance is important, as it must be large enough to allow the WLS fibers to maintain the minimum 2 inch bending radius we are seeking [22] as the fibers are routed into the connectors. The cabling scheme we have devised calls for a minimum bending radius of 59 mm (2.3"), comfortably beyond the prudent minimum (see Sec. 3.3.2).

The WLS fiber connector on the FPS detector must be precisely mated to its mating connector on the clear waveguide fiber bundle assembly leading to the VLPC photodetectors. As indicated earlier, in order to minimize light losses, fiber-to-fiber misalignment must be kept below 1.5 mils. We have therefore opted to use two alignment pins, similar to those used in the CPS connector, which have been shown to work quite well both in tests performed at UIC and during the Summer 1997 FPS beam test at Fermilab [23]. We have chosen as well to follow the alignment pin polarity scheme that was used for the CPS connectors. Two pins of different sizes, one on each side of the connector, will serve to both align and couple the WLS and clear fiber connectors on the detector side. The larger (smaller) pin will measure 2.39 (2.11) mm in diameter. The polarity ensures the proper orientation during WLS/clear connector mating, as dictated by mapping concerns. The connectors are bolted to one another by inserting flathead 0-80 1/4" socket-head bolts into these inner-threaded alignment pins. Light transmission will be kept above 95% by a uniform application of optical grease couplant at the WLS-fiber-to-clear-lightguide connector joint.

We are still studying the most effective means of making the assembly light-tight. Although aluminum skins will cover the active region of the detector, cracks will inevitably remain that will have to be effectively masked over. The connector brackets will be made of sheets that will be bent to form a covering over the region through which the WLS fibers are routed as they emerge from the outer ring to the underside of the connector. This region, too, will probably require additional attention for potential light leaks. RTV is an obvious candidate at such metal-to-metal joints; we are still, however, considering a number of different options here, and have yet to settle on any specific technique.

3.3 WLS Fiber Routing and Assembly Procedures

3.3.1 WLS Fiber Length Determination

The FPS modules contain a u- and a v-layer, with the strips in each layer oriented perpendicular to one of the radial sides of the sector module. Within each strip, the 0.835 mm WLS fiber will be inserted, protruding approximately 3-5 mm on the far end from the connector. In order to collect all of the light, half of which travels down each end of the fiber, we have opted to silver this "non-connector" end. The fiber will be held in place at both ends of the scintillator by a small ($\simeq 0.9$ mm diameter) O-ring. This proved to work very well in the test beam prototypes. These O-rings eliminate the need for gluing, which can be very messy, are able to hold the fibers very firmly in place, and have the advantage of being easily reversible: any mistakes made during cabling can be readily undone and the proper connections easily re-established.

The WLS fibers will be delivered in 3 meter canes. They will be pre-cut in lengths of 1.0 (1.5) m for the large (small) modules, and both ends will be both polished and aluminized (by vacuum deposition) at Fermilab. The fibers will then be shipped to Stony Brook for insertion into the fiber connectors. Prior to insertion, the fibers are cut in half (50 cm and 75 cm lengths), and the aluminized ends protected with small dabs of glue.

The trapezoidal geometry of the FPS modules dictates that only the two nested scintillator strips in each u (or v) layer have exactly the same length. The length of the associated WLS fiber depends on the length of the strip it is coupled to, the strip position, the position of the connector, and on the detailed routing it is constrained to follow. We have devised an efficient algorithm to accomplish this task, which is calibrated and cross-checked with actual measurements at critical locations on the detector. The algorithm has worked very well for the prototype modules, and will be repeated for the final design.

In order to determine the fiber routing and the connector placement, the FPS group has constructed a full-scale test jig for each of the three major types of modules. The jig is flat and has a full scale Autocad to-scale (1:1) drawing of an actual module on its surface, showing numbered locations of each strip and connector. Several (≈ 10) scintillator strips are fixed on the jig at locations that represent classes of cable lengths. These classes are used to represent a full complement of fibers in the final determination. The WLS fiber for these strips are optimally routed, and the resulting fiber lengths measured; the regular spacing of intervening strips in the u- and v-layers leads to a simple linear interpolation, that is used to find the fiber lengths for these intermediate strips.

Once the lengths are determined for all fibers in the module, a fiber length map is made for each connector of the module, labeled by strip number. A graphical full scale map is plotted for each connector of each module type. On a second jig, with the plot mounted and the actual connector fixed at one end, individual WLS fibers are inserted into the connectors using this map as a template, and the fibers are then glued to connectors. The connectors are labeled according to position and module type. They are then packaged and sent to Fermilab for diamond fly-cutting and polishing. The final product is sent back to Brookhaven for module assembly.

The WLS fiber routing scheme shown in Fig. 22 was created with no attempt to equalize the WLS fiber lengths. Using this scheme, we have determined using the cabling jig that the lengths of the WLS fibers in the large module will vary from 14 to 88 cm. In an effort to ameliorate any channel-to-channel response variations due to such length differences, we have also developed a scheme wherein all of the cable lengths in all three module types – large, small, and special – are equal in length to the longest WLS fiber (88 cm). In order to realize this uniform-length scheme, a few additional loops were introduced to the path of the shorter fibers, and the mapping of which WLS fiber goes to which connector was appropriately rearranged. No modifications to any aspect of the design, including the physical position of the connectors, were necessary. Naturally, the requirement that all fibers be the same length makes the WLS cable length determination quite a bit easier as well.

Since the longest cable in the small and special modules is 68 cm, we may opt to match all of these fibers to this length for these two module types, keeping the 88 cm length in the large modules. The response variation induced by this 68-to-88 cm difference is negligible[4], taking into consideration the expected $\approx 15\%$ lot-to-lot variations in the VLPC response, and the $\approx 3\%$ (5%) variations expected through connector interfaces (channel-to-channel SVX response). Using shorter fiber lengths in the smaller modules eliminates the need to deal with the 20 cm excess for each fiber that would result from implementing the former scheme.

3.3.2 WLS Fiber Routing

Prior to the full detector assembly, the routing of the individual WLS fibers from the scintillator strips to the 16-channel FPS connectors must be carefully determined. Possible routing schemes are severely constrained by the tight space limitations. Moreover, the required minimum fiber bending radius of 2" must be respected throughout the cable run.

In an effort to most completely understand the limitations of various fiber-routing schemes, the cabling jig described above has been used to mock-up various scenarios. Clearly, the design of the outer radius of the detector – including the active coverage of the modules – is intimately coupled to the location of the connectors. The final position and orientation of the connector assemblies shown in Fig. 22 is the result of a significant amount of thought and legwork. The ICD detector at the outer radius has introduced a number of difficult and defining constraints for the layer closest to the cryostat head (Layer 1), which is the most problematic region of the detector. To limit the complexity of the hardware, our solution to the cabling issues for this layer has been applied to all the other detector layers.

The WLS-to-clear connectors have to be accessible after the FPS is installed; they must therefore be situated at the outer perimeter of the detector. Since these connections will be made in a limited amount of space *in situ*, they must be able to be easily made. A generous amount of space has to be available to ensure that the sensitive fiber/connector interfaces on the outside of the detector are not corrupted in any way during installation, or over time during Run 2. The placement of the connectors in r is dictated by a number of competing constraints. In order to maximize the active coverage of the FPS (*i.e.*, by increasing the $|\eta|$ coverage between $1.4 < |\eta| < 1.5$), the distance between the WLS connector and the upper module edge will necessarily decrease, for a fixed connector position. The minimum bending radius of the fibers, on the other hand, dictates

[4] The attenuation length for these Kuraray Y11(250 ppm) WLS fibers, using VLPC for readout, has been measured during the CPS cosmic ray test [18] to be ≈ 10 m. This yields about a 2% response variation between fibers with lengths of 68 and 88 cm.

that the connector has to be at least 40 mm from this edge. At larger r, the clear fiber connector must be far enough away from the ICD (in some combination of both r and z) to ensure that connections are easily made, and that stresses are minimized for both the fibers themselves and the fiber/connector joints. On the WLS side, construction and similar internal cabling considerations also demand that the row of connectors in Layer 1 not extend in z beyond the inner edge (*i.e.*, the edge at the smallest $|z|$) of its outer ring. Moreover, the clear waveguide bundles will likely have to be routed over the face of the ICD, limiting access to that detector, and imposing a number of logistical installation constraints. The design of strain-relieving clamps for the clear bundles will also have to respect the presence of the ICD.

In the r-z view (see Fig. 23), it is evident that the connectors are mounted in an approximately vertical position: they do not follow the contour of the EC head (or the preshower itself). This helps to accommodate the routing of the clear fibers over the face of the ICD, while maintaining a generous bending radius. It also allows the clear fiber connector itself to easily clear the face of the ICD. Constraints on the inner (WLS) side of the connector, however, prevented us from pitching this connector too far: an appropriate bending radius at the sensitive connector-to-WLS-fiber joint had to be maintained. The pitch of the connector shown in Fig. 23 is therefore a compromise between these two basic considerations. These constraints also influenced our decision to mount the connectors in one row, which required a new connector design.

The fiber-connector layout scheme that is believed to be optimal is shown in Fig. 22. The layout chosen preserves the maximum active scintillating region for the detector, and locates the fiber connectors at the outer edge of the detector. The 16 fibers emerging near the outer radius, detector region 9, exit with a 290° fiber loop of radius of about 4 cm over the face of the module, and enter the connector closest tot he bisector of the module (number 9). The 32 fibers from detector regions 7 and 8 emerge on the other side and end through 90°. Fibers from the remaining regions 1-6 bend through angles between 60° and 130° and travel partly over the module face.

Thus about half the fibers will need to be partially routed through the existing 2.5 mm gap between the module and the aluminum cover skin. This 2.5 mm gap is found to be quite sufficient, given the density of fibers in this region. Clearance of about 0.8 mm is left at such crossing points. In the current layout, the bending radii are kept within the required limits. As an additional check, we are currently making our own measurements of the light transmission as a function of bending radius.

We mention that the cabling solution we have developed will allow us to extend the module coverage slightly by cutting the module with a circular, rather than a straight, contour at its outer radius. We refer the reader to Sec. 2.3.3 for a more detailed discussion of this.

3.4 Clear Fiber Waveguides

A major technological challenge for the upgraded DØ detector will be the large-scale use of Visible Light Photon Counters (VLPCs) that will serve as photodetectors for both the preshower detectors as well as the CFT. VLPCs require cryogenic operating temperatures of $\simeq 6-10°$K, requiring the use

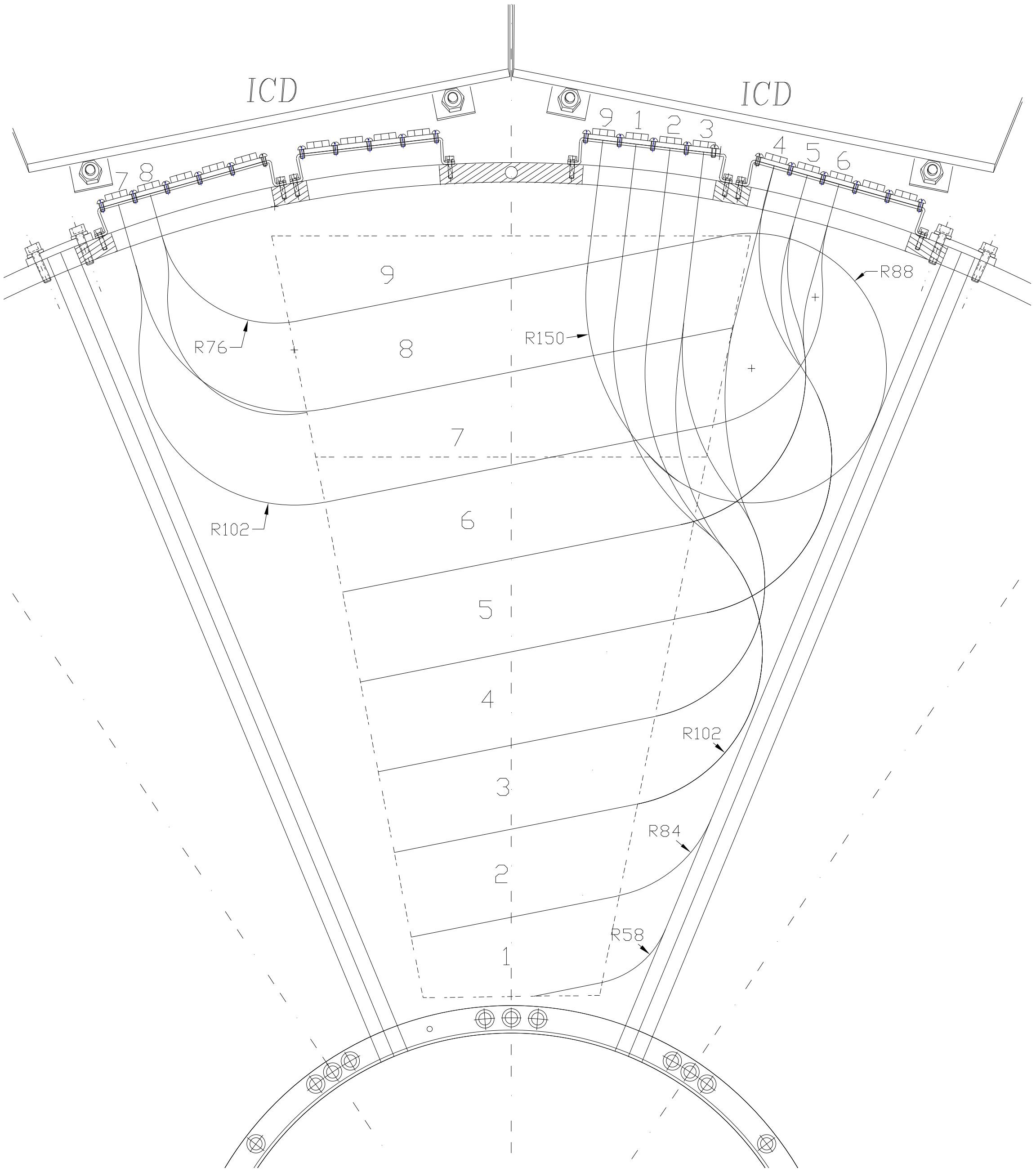

Figure 22: The r-ϕ view of one module in Layer 1 of teh FPS, showing the WLS fiber/scintillation strip layout and routing. Individually labelled connectors are shown at the top – they map to regions of 16 contiguous strips on the detector as shown. Cabling and connector numbers for the u layer only are shown – the v layer is mirror-symmetric.

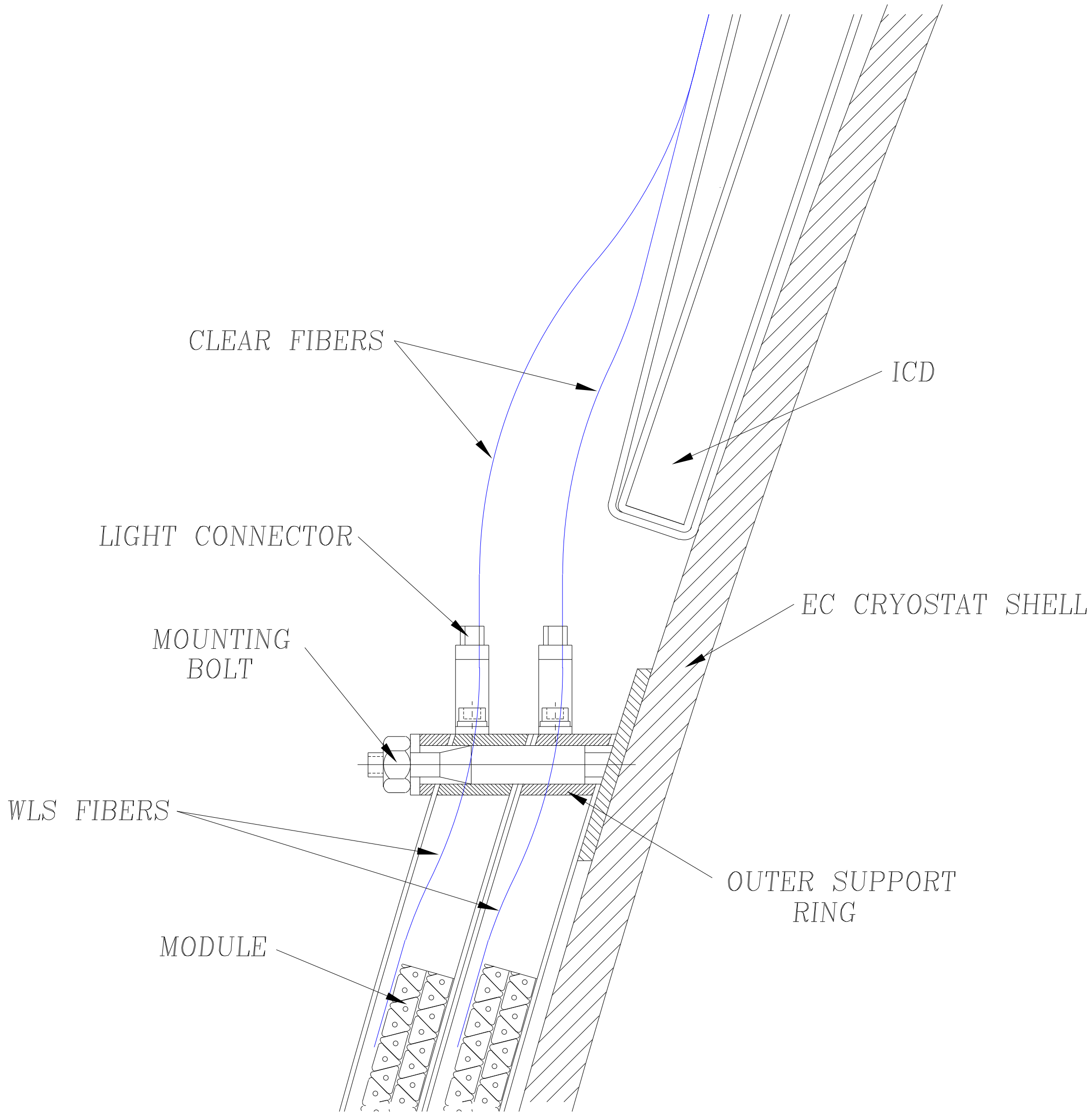

Figure 23: Side (r-z) view of the FPS-ICD interface. The connectors for each of the layers are in one row, and are pitched relative to the contour of the cryostat. Bending radii both internal and external to the detector, ease of cabling, and access to the two detectors were major factors in determining the cabling scheme and final design at the outer radius. Details are in the text.

of liquid helium and cryostats. In addition, specially designed connectors must be used at the warm input end of the VLPC readout. The waveguide cable and connector design must accommodate and match the high channel density and the readout granularity of the photodetectors and the following SVX-II readout chain.

During inital R&D studies, the UIC group constructed 30 128-channel lightguide bundles both 8 and 11 meters in length. Twenty-four of these were tested successfully in the cosmic ray test setup in 1995 at Lab 6 at Fermilab. The bundles are terminated with 128-channel connectors machined from a square block of black Delrin plastic [14], which connects firmly to the short waveguides leading into the cryostat.

Clear multiclad fibers made by Kuraray [12] will be used in the FPS lightguide bundles to transport scintillation light from the WLS fibers of the detector to the remote VLPCs. The clear fiber consists of an undoped polystyrene core enclosed by two 25-micron-thick layers of cladding. The inner cladding layer consists of acrylic plastic, and the other of a fluorinated polymer. Two of the more significant advantages of using multiclad as opposed to single-clad fibers are their longer attenuation length (approximately 10 m [14]), and the fact that they are mechanically more robust.

Kuraray offers two different types of fibers from exactly the same base material. These are conventionally known as the 'non-S-type' and the newer 'S-type' fiber. Although the non-S-type fibers are observed to have a $\simeq 30\%$ longer attenuation length, the non-S-type fiber is very brittle and easily damaged. The S-type fiber is far more resistant to bending and cracking. Results reported for the CPS [8] indicate that light losses are several percent greater in fiber-to-fiber connector joints where non-S-type, rather than S-type, fibers are used. Experience with the non-S-type fibers during the recent FPS beam test showed them to be quite sensitive to handling, and difficult to work with. Therefore, like the CFT and CPS, the S-type fiber by Kuraray has been retained as the fiber of choice for the FPS detector.

Details of the construction of the clear fiber bundles are described elsewhere [7, 14]. All bundles were tested for light transmission after fabrication. Out of the 30 bundles tested at UIC, one full bundle appeared to be damaged during handling. The remaining 29 bundles had an average bad channel count of 0.2% over the total of 3712 channels. The light transmission efficiency through the connector was of the order of 90%. These tests indicate that a satisfactory method of bundling and testing has been developed.

3.4.1 Sixteen-to-128-Channel Bundle

The 128 fibers in a waveguide bundle must be split at some appropriate point into 8 separate bundles of 16 channels each to match the FPS WLS detector connectors discussed earlier. The cable run around the perimeter of the FPS along the face of the ICD and through the cable winder requires a maximum of 13 to 15 meters of cable in order to reach the VLPCs below the platform. The responsibility for fabricating these bundles for the FPS and CFT is in the process of shifting from UIC to Notre Dame.

The bundles produced to date at UIC were fabricated under strict quality control, and tested using an automated procedure [8]. Fibers were cut to length and checked for continuity and light transmission. Groups of 16 fibers were placed into black plastic sleeves of about 7 m long to ensure that they were protected and light tight. Individual fibers are glued into the 16-channel preshower connectors using the same procedures as described in Sec. 3.2.2. At the other end the 128-channel cryostat connector is fixed. Somewhat before the 7 m branching point, all eight groups of 16 fibers are gathered together, and the remaining 6 m is wrapped in a 3/8"-diameter black PVC jacket manufactured by Zippertubing [15]. The PVC jacket both provides mechanical protection and prevents light leaks. A strain relief bracket is mounted between the connector on the VLPC cryostat and the 128-channel clear fiber bundle, which maintains the mechanical integrity of the fiber-connector joint. A similar strain-relief is implemented on the detector end as well. Finally, both connector ends are polished with the Fermilab diamond-fly cutting machine.

3.4.2 Routing of the Clear Fiber Bundles

The routing of clear fiber bundles from the FPS connectors to the VLPCs located below the platform of the DØ detector is, to a large extent, governed by the electronic readout chain and the signal mapping requirements at the Level 1 trigger. In the current scheme, a single FPS triggering "unit" consists of the signals emerging from the large and small module at a given ϕ position. We call this unit a readout sector (see Sec. 3.7). The $(18 + 14) = 32$ connectors that service these modules result in $32 \times 16 = 512$ possible connections, or half of the channels in one VLPC cassette – a very natural unit for detector readout. (We note that not all of these channels will be used; the total signal count for these 32 connectors will be on the order of 274 (large module) + 198 (small module) = 472.) The 32 clear fiber mini-bundles emerging from the readout sector will probably be merged into a super bundle as they are routed radially out and along the face of the ICD in ϕ. The channel count for the final VLPC-end connectors, which will dictate how the super bundle will be split at the other end, has not yet been decided on. We note that we expect the cryostats for the FPS to be located at either end of the platform (in x), with the signals for the FPS-North and FPS-South each being serviced on opposite sides. There should therefore be no need for re-mapping the signals (in, say, a junction or transition box) as they are routed below the platform to the VLPCs.

We are currently in the process of developing a full scheme for routing the clear fiber bundles from the perimeter of the FPS to the VLPCs below the platform. The bundles from Layers 1 and 2 (*i.e.*, from the large modules) will be routed along the face of the ICD, and those from Layers 3 and 4 (*i.e.*, from the small modules) will be routed along the face of Layer 2, just above the lead absorber in r. The required length for the clear fiber bundles varies from ≈ 10 to 15 m, depending on origin. Cable supports, in the form of L-shaped brackets, will most likely be mounted directly to the cryostat in the region between the FPS and the ICD. These brackets will provide a means by which the bundles will be tied or clamped for support and protection. A means of interleaving the bundles from different readout sectors as they join those of other sectors (in ϕ) along the face of the ICD is in the process of being developed. We are hoping to make all bundles the same length. A suitable means by which the significant amount of excess cable that will result can be dealt with will have to be developed in this case. All of these issues – perimeter route, means of strain relieving, clamping hardware, fiber routing through the cable winder, protective sheathing, accommodating excess cable, and so on – are being vigorously investigated by the FPS group.

3.5 Quality Control during Construction

The design and production of the preshower prototype modules has provided us with a detailed understanding of the procedures that must be implemented during final production. This includes careful monitoring and testing of individual detector components at all stages of construction in order to have a fully operational and reliable detector.

Since individual scintillator strips are both extruded and machined-wrapped at relatively high speeds – on the order of 1 ft/sec and $\simeq$ 4 ft/min, respectively – only a preliminary inspection of each strip can be done during each of these procedures. During the extrusion, we intend to inspect every five or ten strips for correct outer dimensions of the triangular profile at various places along their lengths. Since some irregularities were found in the hole dimensions for the strips used for for the FPS prototype, we intend to insert a 0.835 mm-diameter WLS fiber down the full length of the axial hole of each strip to check for any deformations or other irregularities. Visual inspection of the mylar wrapping will be performed during the wrapping procedure.

After gluing and surface polishing, each channel in the WLS fiber/connector assemblies will be checked for light continuity. Such a test will be done by exciting the WLS fibers one at a time with a blue LED and measuring the response at the connector end via a short clear bundle and a single PMT. This system will be very similar to the calibration test setup already in use at Stony Brook. Light yields similar to those described earlier will be expected. We refer the reader to section 2.3.4 for a description of the module-connector testing procedure that will be performed during the detector assembly.

A construction and assembly database will be kept for the entire collection of intermediate and final system results and a history summarizing the measurements for each detector component will be available.

3.5.1 Continued R&D and Fiber-Connector Readout Tests

In order to continue the study of fibers and connectors under various conditions, the Stony Brook and Brookhaven groups are each developing a test stand to continue the R&D of the optical properties of the relevant FPS components. The Stony Brook stand is already being used for a variety of studies. The dependence of light transmission with fiber bend radius, the long term stability of components, detector calibration methods, cross talk in the fibers and at the module edges, and the effects of heating ("slumping") on the scintillator response are a few of the more important topics that are being addressed.

The Stony Brook test assembly uses both green and blue LEDs as light sources. Output will be measured on a multi-anode photomultiplier tube. The testing is being designed to be fully automated by the use of a workstation or an equivalent PC. Initial testing has been using a CAMAC module, with analysis done by programs written in Quick Basic. Future tests will build on these initial components. The system will be upgraded in the near future to include a sixteen channel analog-to-digital converter and LABVIEW software [16].

3.6 Forward Preshower Calibration System

The function of the Forward Preshower (FPS) calibration system is two-fold: first, the system serves to certify the proper connectivity and yes-no operation of the fiber channels and attached readout chain; second, the calibration system, when sufficiently precise and repeatable, will serve to calibrate the response of the individual channels and to provide a relative channel-to-channel energy calibration of the system from the WLS fibers onwards.

Calibration will be done using physics events, special prescaled triggers, and special pulser calibration runs. The latter will be taken when no physics data taking is in progress, e.g. in between collider runs.

The required precision for relative fiber-to-fiber calibration of fibers in the same 16-channel set is of order of 10%. This is to be compared to the expected variations in light transmission through connectors ($\simeq 3\%$), VLPC gain variations ($\simeq 5\%$), and SVX gain variations ($\simeq 5\%$). After tagging and excluding fibers with yields far away from the mean, light yields of individual connectors can be equalized. In this section we describe the pulser calibration system incorporated in the FPS detector.

Injection of light for calibration can be done at several locations; into the scintillator with blue light (directed towards the WLS fiber), into the WLS fiber as blue light, and finally into the WLS fiber by direct optical coupling as green light.

Injection into the scintillator has not been tried as it complicates the detector design appreciably. Injection of green light by direct coupling is complicated: injection ideally would take place at the far end of the fiber, e.g. by placing the WLS fibers retracted by 2 mm inside the scintillator, and abutting them with clear fiber carrying green (or blue) light from an LED; in this method the WLS fiber ends couldn't be aluminized, thus reducing light output from physics signals by a factor of two. Alternatively, green light can be injected using an optical coupler to the WLS fiber somewhere along its length. Of course such an "injector" would also enable physics light to leak out at precisely the same location, and would therefore need to be inefficient in order to keep leakage (and cross talk to adjacent fibers connected to the same injector) at an acceptable level. From an optical point of view, using a blue light injector is preferable. In order to inject into a set of sixteen fibers a calibrated amount of light (calibrated at least relatively), the WLS fiber length exposed to the blue light and the distance to the source must be carefully controlled. This can be achieved in several ways. A plexiglass lightguide for the blue light fixes both optical coupling area for the attched fibers, and the source-to-fiber distances. Alternatively, one could fix the fibers in calibrated spatial positions with respect to the LED source, and mask off fiber regions for illumination, i.e. a air-based lightguide. Finally, one could direct the light towards individual WLS fibers with clear fibers lightguides and individual couplers to the WLS fibers. Of the above methods, the plexiglass waveguide seems technically the simplest and most promising. Below we describe prototype tests based on this last approach.

We are presently testing a prototype calibration system which is based on injecting LED light pulses to 16 channels at a time, at the place just before the WLS fiber enters the molded sixteen channel connector to the clear fiber cable. A sketch of the proposed LED pulser is shown in Fig. 24.

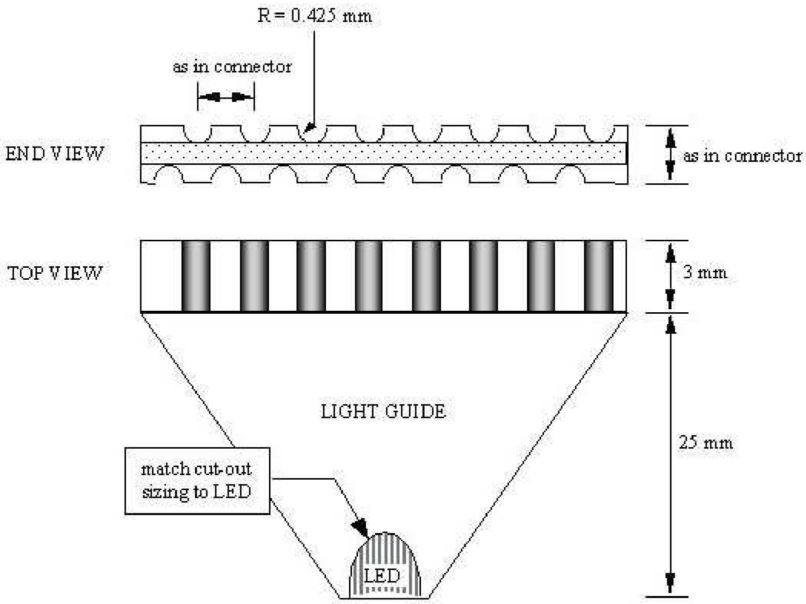

Figure 24: Proposed calibration pulser for sixteen WLS fiber channels to be located directly before the connector to the clear fiber bundle. The 2×8 CPS connector design is shown.

3.6.1 Prototype LED Pulser System

Current tests are done with a common green LED as light source. Tests with fast Nichia [13] blue-emitting LEDs for calibration are in progress. Injection with blue light is very efficient and is expected to be more reproducible. The current design, and the prototype tests described below, were made assuming the earlier WLS fiber connector design used in the CPS (two staggered rows of eight fibers). The design will be adapted to the new 4×4 WLS fiber connector.

A fan-shaped Plexiglas light guide guides the green LED light towards a rectangular Plexiglas distribution/injection block with 16 grooves, eight per side, that match the fiber spacing in the adjacent connector. The block and light guide are painted with white reflective titanium-oxide paint, to diffuse the light equally over the sixteen fibers. The grooves and the hole for the LED are milled after painting. The fibers are held in the grooves by a thin black Delrin U-shaped clamp that mounts over the fibers. The LED is glued in place with optically transparent epoxy (BC-600), and subsequently painted.

3.6.2 Results of Prototype Tests

A first prototype was built from a Plexiglas bar with 10 holes for fibers and a light guide for the LED (see Fig. 25). The prototype was machined from a single piece of 3 mm thick Plexiglas, with 10 holes of 0.85 mm diameter for the fibers and a cut-out for the LED. Current results, using PMT readout, are shown in Fig. 26, where the pulse height distribution of a fiber/PMT channel is shown for each of the ten holes. The means and their uncertainties are plotted in Fig. 27. The results show that the systematic variations between the centrally located holes are at the level of 13.4% if one ignores the fibers in holes 9 (located off-center by about 1mm) and 10 (badly burned/melted). The remaining smooth variation is most likely due to the narrow emission pattern of the LED, combined with a misalignment (by $\simeq 20°$). In addition, some of the other holes were larger than the required 0.85 mm, due to wobbling of the drill bit in the plexiglass. These problems are being addressed in the latest version of the LED pulser prototype.

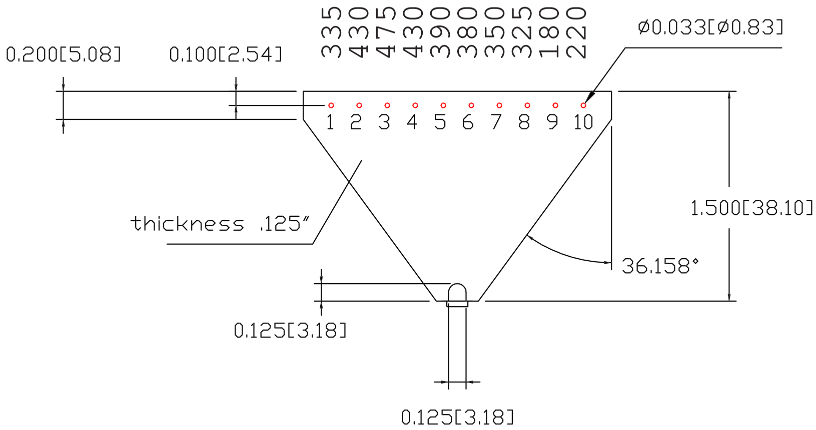

Figure 25: Present prototype calibration pulser for ten WLS fiber channels. The numbers above the fiber holes represent the peaks of the pulse height distributions, rounded to the nearest 5 ADC counts.

We have checked reproducibility of the results, and find that peak positions do not change by more than 10 ADC counts for runs of 10k events or more. The blue LED used has sufficient brightness for our purposes. The PMT was operated at 1.8 kV, and output pulses had 200-300 mV amplitude. The LED pulse used had an amplitude of 4.5 V and a width of 20 ns.

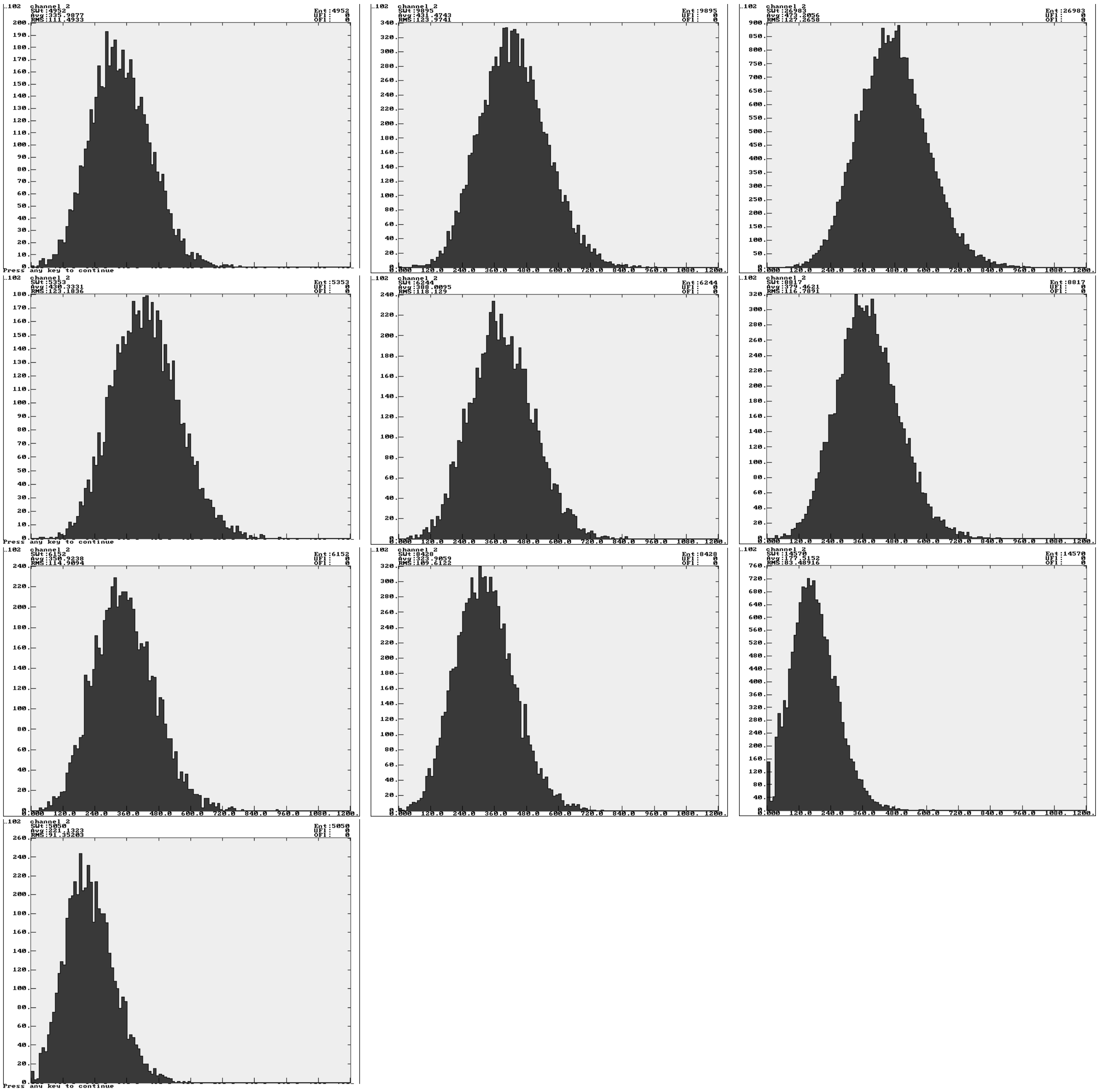

Figure 26: Pulse height distributions at the 10 successive locations in the prototype LED test pulser.

3.6.3 Electronics

The electronic LED pulser driver circuit has to be stable, simple and robust. In its normal quiescent state, it should not inject any noise in other DØ systems, and it should adhere to the DØ grounding rules.

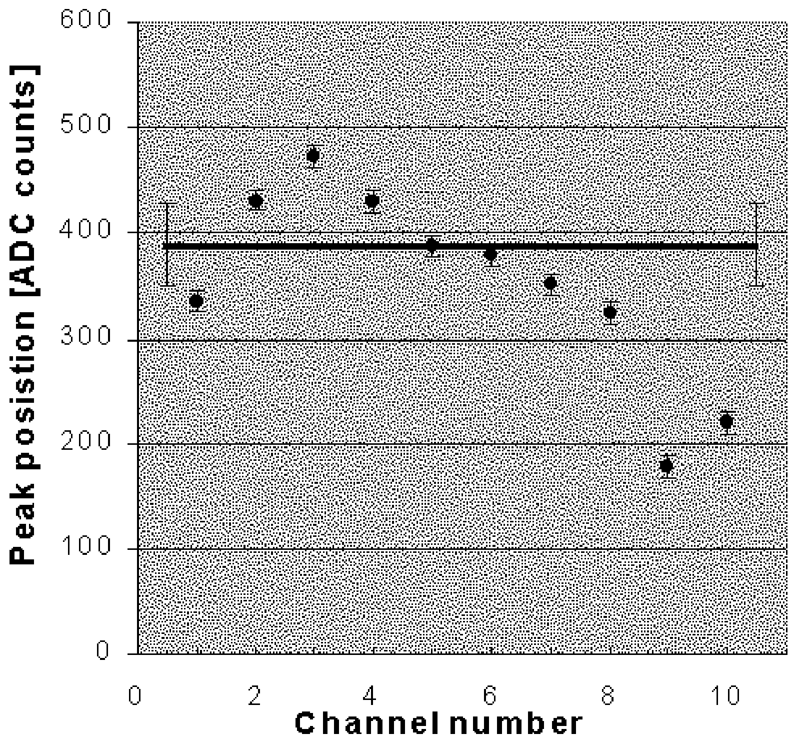

Figure 27: Distributions of the means of the pulseheight distributions at the different locations in the prototype LED test pulser. The error bars indicate the uncertainties in the measured means (of order 10,000 test pulses).

The circuit consists of up to sixteen LED drivers, which are selected by a serial-input multiplexer logic circuit. The logic circuit allows for the individual selection of LEDs, or the simultaneous selection of all LEDs. The four controls and power for the each circuit are: GND, +5V power, $4 - 10$V LED voltage, and a single digital line for serial programming and firing. One circuit per module is foreseen, with the multiplexer circuit located near the outer edge of the detector, and the three-wire LED driver packaged with the LED and optical coupler.

3.7 Trigger

The luminosity in Run II is expected to reach $2 \times 10^{32}\mathrm{cm}^{-2}\mathrm{s}^{-1}$ with an initial bunch spacing of 396 nsec. As the luminosity of the delivered beam increases, it is anticipated that that the bunch spacing will be reduced by a factor of 3 to 132 nsec. We have been asked to design to this latter, more restrictive, specification. The $\approx \times 10$ increase in the luminosity and associated decrease in the bunch spacing relative to Run I conditions have dictated that DØ trigger system be completely re-designed.

The Level 1 (L1) trigger system has to operate at a rate of 7.6 MHz and a latency of less than 4.2μs. The L1 trigger accept rate will be fixed to, at most, 10 kHz, which is limited by the rate capability of the SVX II readout chip. The L1 trigger is based on information extracted from four of the sub-detector systems independently – CFT, preshowers, calorimeter, and muon – which have been fed into a Trigger Framework [27].

The Level 2 (L2) trigger system is designed to make a decision on a time scale of a few hundred μs. It is composed of a global L2 processor (L2GLB) that operates on a list of objects coming from detector-specific Level 2 pre-processors (L2pp). The L2pp will pass a restricted list of physics objects found in each of the sub-systems on to the L2GLB, where appropriate spatial and other (for example, p_T) matching between the objects found in the various detectors will take place. The L2 trigger is designed to provide a factor of $\approx \times 10$ in rejection, resulting in an output rate of ~ 1 kHz. The amount of deadtime at this stage should not exceed 5% [6].

The L1 trigger for the FPS detector is devoted primarily to the detection of electron and photon candidates. Upon requiring coincident energy deposits in front of (electrons only) and behind the lead converter, rejection rates of between 2 to 4 are expected at this hardware level. Calorimeter (CAL) and FPS candidate clusters found in the L2pp are passed on to the L2GLB, where the CAL and FPS information is combined to form electron and photon candidates.

3.7.1 FPS Trigger Hardware

The FPS signals are routed from the outer perimeter of the detector to VLPC cassettes through clear fibers. Each cassette contains 1024 channels, and will map the signals to two electronics boards. The signals for the detector at L1 will be divided into 22.5° ϕ-bins, which we call a readout sector. The readout sector consists of the a sum of the signals emerging from both a small and a large module at the same ϕ position. These signals are grouped and sent to one electronics board, for a total of 472 channels per board. The FPS readout sector will therefore use 472 of the 512 channels in half of the corresponding VLPC cassette. With 16 readout sectors in ϕ per side, a total of 8 VLPC cassettes will be needed for each of the north (FPS-North) and south (FPS-South) detector sides. The cassettes for FPS-North and FPS-South will be located at the extreme and opposite ends (in x) of the VLPC cassette region underneath the detector platform.

The signal for each scintillator strip is charge-divided into two analog outputs – a high-gain and a low-gain arm, described in Sec. 3.1 – and is routed to two distinct sets of Multi-Chip Modules (MCMs). Each MCM consists of four trigger pickoff (or SIFT) chips, and one SVXII readout chip. Only 64 of the full complement of 128 channels for each SVXII chip will be used for the FPS; these 64 channels will map in a one-to-one fashion to the four SIFTS, each of which will contain 16 (used) channels. The high- and low-gain arms will each use eight sets of MCMs, for a total of 16 MCMs per front end board. This results in the desired $8 \times 64 = 512$ channels for each of the arms. The MCMs allow the setting of two trigger thresholds per channel: the high-gain output will in general be used to detect MIPs, whereas the low-gain branch will be used to identify larger depositions associated with showering particles. The ability to resolve MIPs in the showering layers is important (although not for triggering), as this MIP signal will be used for calibration. These issues are discussed in more detail in Sec. 3.1 above.

The digital signals from the SIFT are fed into a series of Large Field Programmable Gate Arrays (FPGA). The gate arrays are pre-loaded with the logic that will be applied in forming clusters. The trigger logic for each module is self-contained on each front end board – each front end board, therefore, will be capable of processing the signals for a given FPS readout sector.

3.7.2 Trigger Concepts and Constraints

The electron trigger is based on the observation of a large energy deposit in the layers behind the $2X_0$-thick converter, where the particles shower, which is spatially matched with a hit consistent with a MIP in the layers in front. The rejection of photons from π^0 decays exploits the fact that they are not detected before the converter. Charged pions are rejected because they tend not to shower, and hence most frequently deposit little energy behind the lead. A Monte Carlo event consisting of a single electron, generated by ISAJET and processed through DØ GEANT, is shown in Fig. 28. The energy deposition profile characteristic of an electron is visible. For comparison, Fig. 29 shows an analogous display for a neutral pion. Requirements analogous to those imposed for electrons in the showering layers are implemented for photon identification; it is required here, however, that there be no energy deposited in the MIP layers in front. Additional handles for triggering include the requirement that the energy deposited by electron (and photon) candidates be isolated, and that the preshower deposition spatially match to an electromagnetic tower above threshold in the calorimeter. The latter has been shown to be an especially powerful tool for rejecting background [6].

The dominant backgrounds for electron signatures are photons from π^0 decays that convert before the FPS and charged hadrons that either shower early or overlap spatially with a photon. The presence of an underlying event (resulting from the hadronization of spectator quarks) and of additional minimum bias interactions that occur in the crossing of interest further compound the challenge of electron identification at both the trigger level and in the reconstruction: the additional π^0 and $\pi^{\pm}$ that are produced translate directly into an increased probability that an underlying QCD interaction will fake an electron or isolated photon. In the pseudorapidity range covered by the FPS ($1.5 < |\eta| < 2.5$) there is no independent tracking information that can be used for triggering. The preshower is therefore intended to augment our electron identification capability in this region beyond that which would be possible by using the calorimeter alone.

3.8 Level 1 Electron Trigger Studies

The Forward Preshower geometry has been developed and integrated into the DØ Upgrade GEANT Monte Carlo. Preliminary results of studies performed with single particle e^- samples to simulate the signal, and dijet events used to simulate the background, are summarized below. A more complete set of signal and background events – W and Z decays to electrons, semi-electronic b

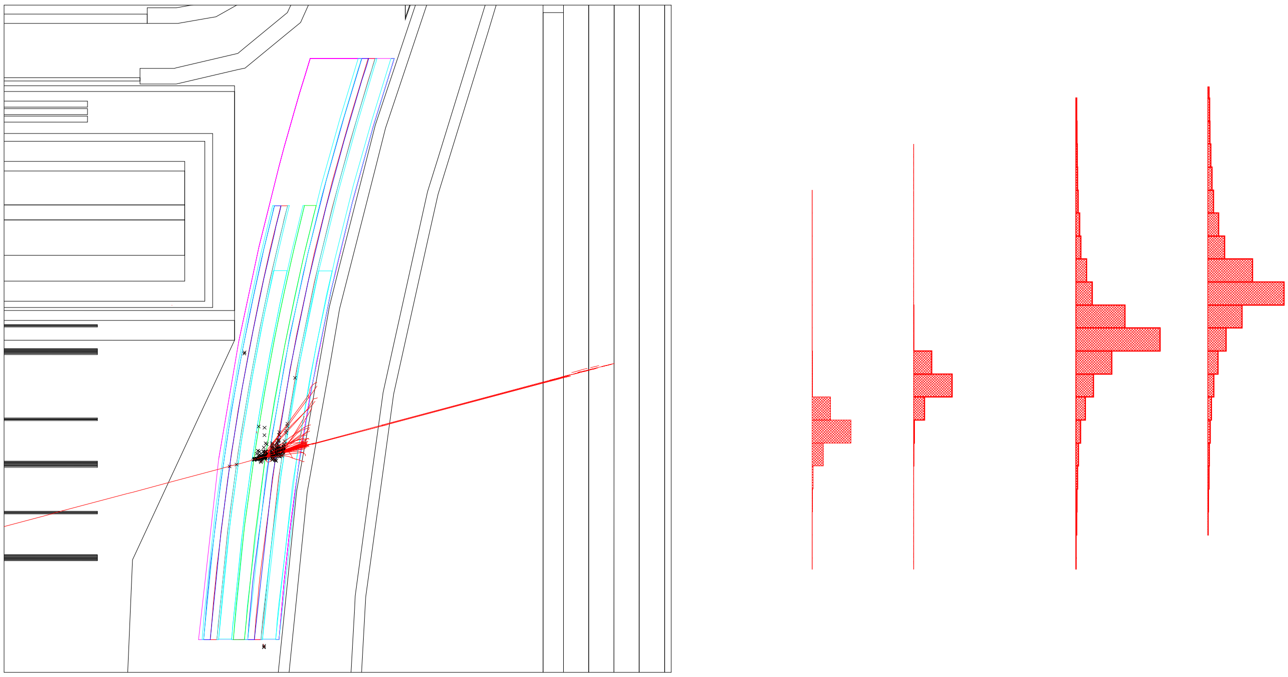

Figure 28: (Left) Side view of Monte Carlo-generated electron, passed through DØ GEANT, traversing the FPS. (Right) A schematic representation of the energy distribution in the four layers.

decays, J/Ψ, and minimum bias events over a broad range in p_T – are in the process of being run through GEANT, which will allow more complete studies of efficiencies and rejections. A photon trigger is also in the process of being developed.

3.8.1 Level 1 Electron Algorithm

A L1 algorithm has been developed that integrates the digital nature of the output from the discriminator in the SIFT. We assume the availability of two trigger thresholds for each channel. We required:

- At least one hit in one of the layers in front of the converter. The strip must have an energy above 1/4 of a MIP signal (≈ 0.3 MeV).
- A deposition of ≥ 10 MeV measured in a single strip in the layers behind the lead. This deposit is required to match the upstream hit in ϕ as well as (separately) in η. The size of the η window is determined from Monte Carlo electron events, which were used to produce a lookup table: for a given η bin in front of the lead, all strips behind the lead that, with a probability of greater than 1%, contain e^- shower energy are considered. The effect of the finite width of the z-vertex position ($\sigma_z = 30$ cm) has also been taken into account.

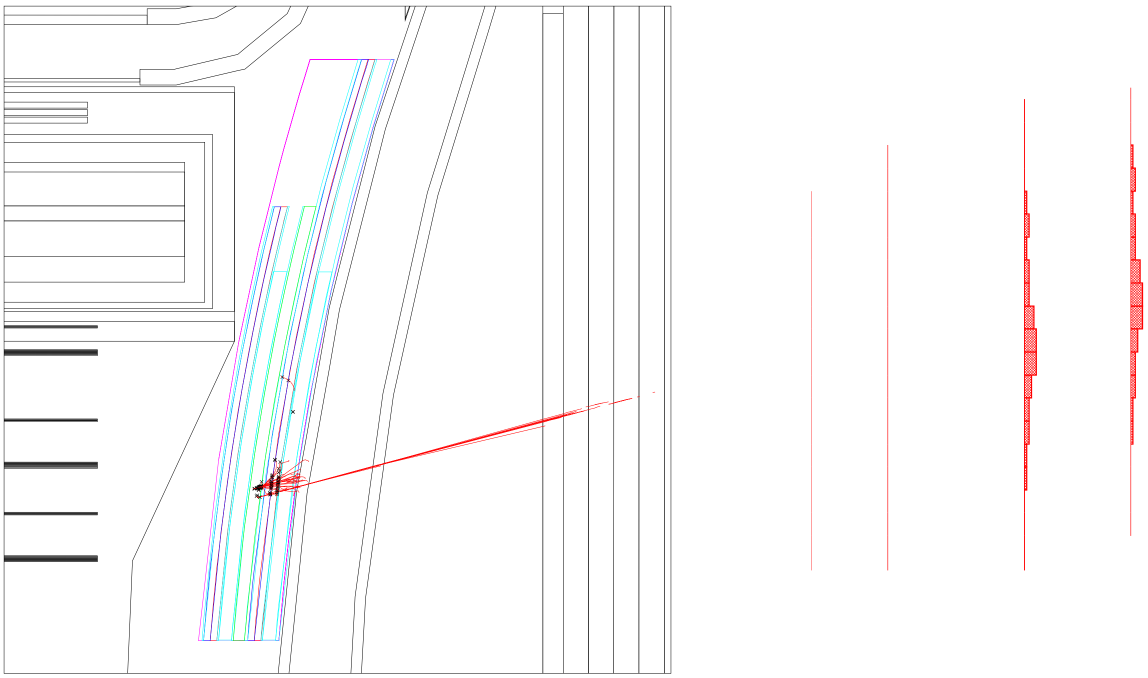

Figure 29: (Left) Side view of Monte Carlo-generated pi-zero, passed through DØ GEANT, traversing the FPS. (Right) A schematic representation of the energy distribution in the four layers.

- An isolation cut. Little energy ($\leq$ 3.5 MeV) is required in the fourth strips on either side of the segments that satisfied the energy requirement.

3.8.2 Single Particle Efficiency

The selection efficiency for electrons using only the energy requirements (no spatial match) as a function of p_T is shown in Fig. 30. There is no isolation criterion applied for the data shown in this plot. More than 90% of electrons are detected for $p_T \geq 10$ GeV. The pion rejection is also displayed on the same plot. The relatively large amount of material before the detector is responsible for a 30% decrease in the π^0 rejection rate, as the photons from π^0 decay have a substantial probability of converting upstream of the detector. This leads to a single track selection-efficiency-to-rejection ratio of $e^-/\pi^0 \approx 2.5$.

The effects of the isolation criteria can be seen by comparing the left- and right-hand plots in Fig. 30. We note that the high-p_T electron selection efficiency is very sensitive to the isolation threshold: the 3.5 MeV cut used does not appreciably effect the electron selection efficiency, but does provide a measurable increase in rejection. We are in process of optimizing this isolation cut, keeping in mind the limitations in dynamic range and the number of trigger thresholds that will be available at the trigger level.

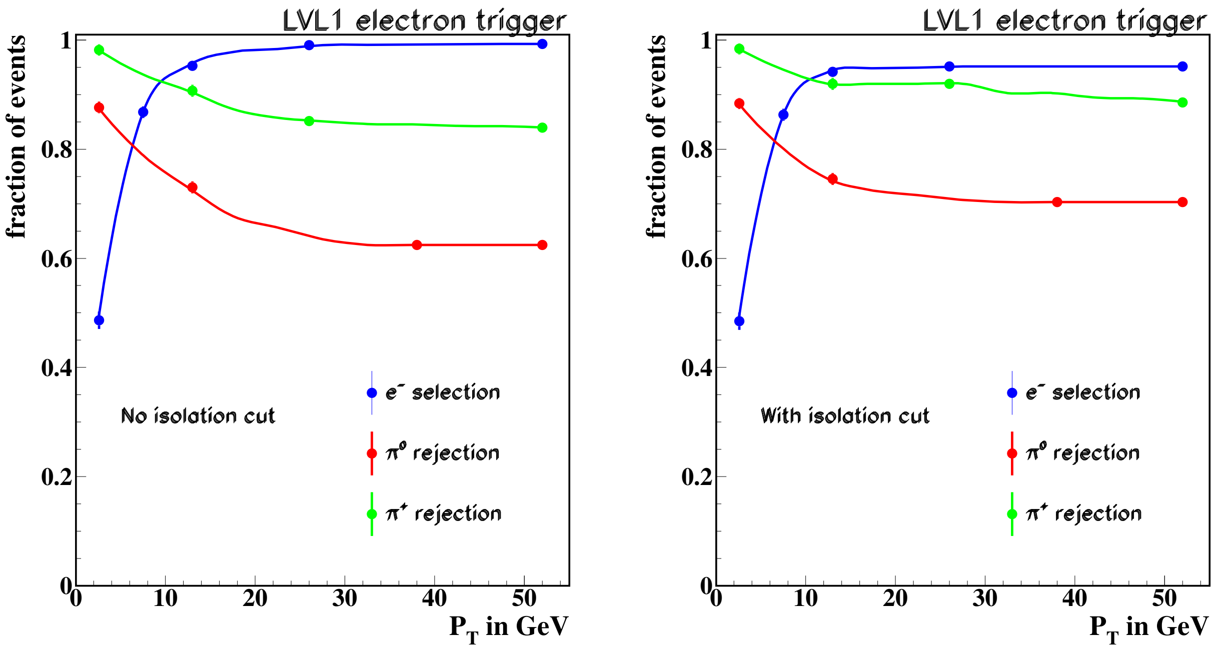

Figure 30: Electron efficiency and pion rejection as function of transverse momentum. These numbers have been calculated for single tracks events with no underlying events added. Figure on right (left) has (has not) had the 3.5 MeV isolation cut applied.

3.8.3 Occupancy

The occupancy was determined by using dijet events with $5 < p_T < 500$ GeV to which one additional underlying interaction has been added. The probability that an energy of 0.3 MeV or more has been deposited in the layers in front of the lead converter is shown in the left-hand plot in Fig. 31. The occupancy for these front layers is below 1.2% for all η. The occupancy for the layers behind the lead as a function of three energy cuts is shown on the right in Fig. 31. They are seen to be negligible – $\leq 0.2\%$ – for a threshold of 5 MeV or greater.

3.8.4 Level 1 Trigger Timing

It is expected that one crossing (132 ns) will be needed to get the information through the VLPC $\Rightarrow$ SIFT $\Rightarrow$ Programmable Logic Device readout chain at L1. It will then take 2 to 4 crossings to form clusters in each layer, reconstruct tracks from the clusters, map the tracks from (u,v) to (η,ϕ), and forward the candidates to the FPS L1 Manager. The L1 Manager will then require 1 to 4 crossings to sort the front end data, and form and send the appropriate trigger terms to the L1 trigger framework. A conservative estimate of the time needed to make a decision at this level is 9 crossings, or 1.2 μs, which is compatible with the upper limit of the amount of time we expect will be available. This upper limit is 4.2μs, and is dictated by dead time considerations.

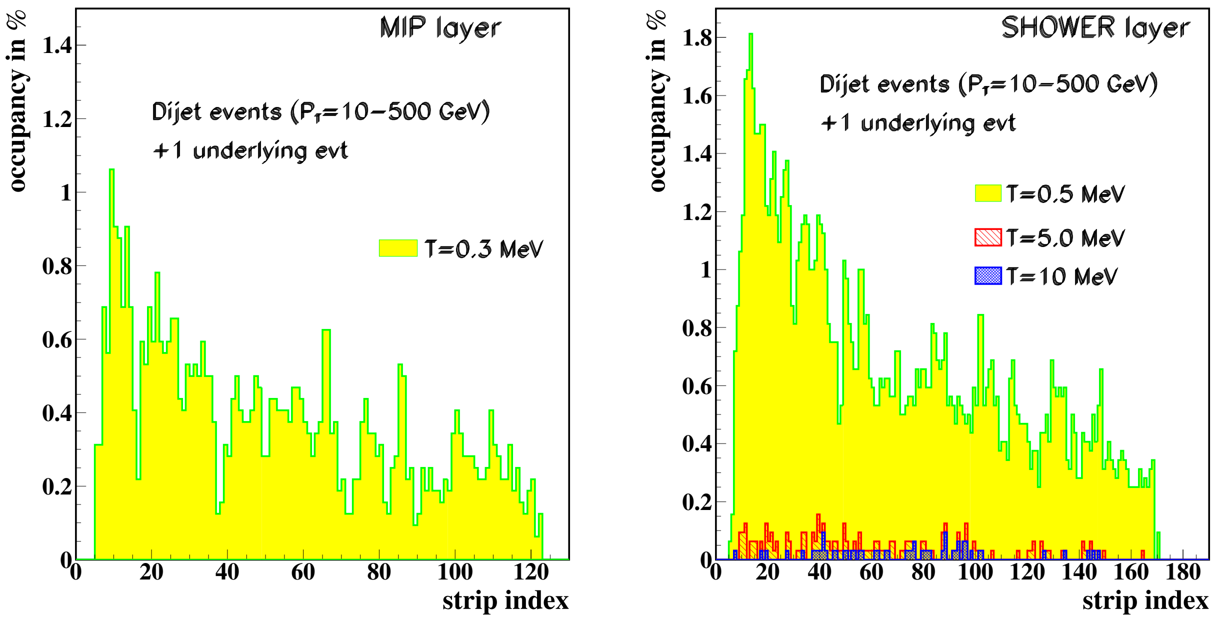

Figure 31: (Left) Occupancy in the FPS for the layers in front of the lead. (Right) Corresponding plot for the rear layers. One MeV is approximately equal to one MIP. Low (high) strip number corresponds to high (low) $|\eta|$.

As mentioned previously (see Sec. 3.7.2), much of the rejection that the FPS will provide will result from matching the FPS candidate cluster to EM towers in the end calorimeters. Even a coarse match between the FPS and the calorimeter would be useful at Level 1; we are currently investigating the possibility of doing this. Preliminary discussions with those designing the L1 trigger framework [28] indicate that the E_T sum of the electromagnetic trigger towers in each of the four quadrants of the calorimeter endcaps should be able to be made available for matching with FPS clusters at L1 within five crossings. We are currently studying the rejection rates that such matching will provide.

3.9 Level 2 Electron Trigger

The global L2 trigger decision operates upon the information coming from both the calorimetric towers and the FPS information. The EM calorimetric trigger is based on the transverse energy deposition in the trigger towers covering 0.2×0.2 in $\Delta\eta \times \Delta\phi$ measured at L1. A specific pre-processor (L2CALpp) will be devoted to selecting the electromagnetic candidates by using the η and ϕ position of the seed towers from the L1 trigger. The resulting information will be sent to the global L2 trigger. This system is being designed to send electron and photon candidates to the global L2 within 100μs. We are currently in the process of studying how best to apply and integrate the FPS information at L2 for both electrons and photons, and are actively pursuing the development of a unified approach for applying information for both the Central and Forward Preshower detectors at Level 2.

4 Project Organization

We briefly discuss the institutional responsibilities in the FPS project, and present an outline of the construction schedule.

4.1 Institutional Responsibilities

The institutions participating in the construction of the Forward Preshower are Brookhaven National Laboratory, State University of New York at Stony Brook, University of Illinois at Chicago, University of Notre Dame, and Fermilab. The lead institution in the construction of the FPS is Brookhaven National Laboratory. Jonathan Kotcher (BNL) is the Subproject Manager. The detector fabrication is centered at Brookhaven, with BNL taking on responsibility for the detector design and construction, module assembly, construction, and testing, detector pre-assembly and alignment, and delivery of the detector to Fermilab and subsequent installation at DØ. Brookhaven is also taking on the responsibility of establishing the proper detector geometry in the calibration and alignment databases, as well as in the Monte Carlo.

SUNY Stony Brook is taking on the responsibility of establishing the lengths and the routing of both the wavelength-shifting fibers (WLS) and the clear fiber waveguides. They will also oversee the preparation of the WLS fibers, and the cutting and polishing of the fiber/connector interfaces, which will be done by Fermilab and the University of Notre Dame (see below). Stony Brook is also designing and implementing the LED calibration system. This will be developed in tandem with the overall detector design being pursued at BNL. Stony Brook is also taking on the primary responsibility for establishing the FPS triggering and reconstruction.

The cutting and polishing of the WLS fiber/connector interfaces, and the polishing and silvering of the WLS fiber ends, will be done by and at Fermilab. The cable lengths will be supplied by Stony Brook, who will also oversee the procedure. The fiber/connector interfaces at both ends of the clear fiber bundles (the VLPC and WLS fiber ends) will be cut and polished by the University of Notre Dame. The clear fiber bundling itself will be done at the University of Notre Dame as well. The lengths of the clear fiber bundles, their routing, and the methods by which the bundles and super-bundles will be strain relieved along their path from the FPS connectors to the VLPCs below the platform will be established by Stony Brook, Brookhaven, and Fermilab.

4.2 Schedule

We list in Table 3 below the anticipated target dates for the design and construction of the FPS:

Milestone	Target Date
Design complete	30-Jan-1998
Forward Preshower TDR submitted	02-Feb-1998
Scintillator procurement complete	24-Apr-1998
Begin connector assembly (detector side)	30-Mar-1998
Connector assemblies complete (detector side)	21-Jul-1998
Module fabrication begun	13-Apr-1998
First module complete	01-Jun-1998
Modules 50% complete	03-Nov-1998
Module fabrication complete	09-Apr-1999
FPS-South detector complete	14-Apr-1999
FPS-North detector complete	18-Aug-1999
FPS-South installed/hooked up	06-Aug-1999
FPS-North installed/hooked up	10-Dec-1999

Table 3: Schedule milestones for the construction and installation of the FPS.

5 Summary

Many measurements that we intend to carry out in Run 2 will be greatly enhanced by increasing the acceptance for electrons (and photons). In order to fully exploit the capabilities of the DØ detector – and, in particular, the high-resolution forward electromagnetic calorimeters – we must be able to trigger on and reconstruct forward electrons. The Forward Preshower has been introduced in order to enhance our coverage for both high- and low-p_T processes, containing final-state electrons and photons, during Run 2.

We have described the design, construction, assembly, installation, and various aspects of the readout of the FPS in this report. A detailed scheme has been developed for the construction of the detector, which is scheduled to begin in February of 1998. The R&D program we embarked on for building the prototypes for the Summer 1997 beam test at Fermilab provided us with invaluable experience. A systematic, reproducible means of fabricating accurate modular active elements has been developed. These elements were tested with electrons, and they performed as expected. A complete design of the attendant support structure has been developed, in which the 1 mm alignment goal that we are after has been respected. The logic and hardware for the module assembly, support frame alignment and assembly, support of the lead aborber, module installation and testing, layer alignment and installation, and detector mounting and alignment have all been presented. Outlines of the cable routes, calibration system, readout scheme, and triggering issues have also been presented. Studies on these topics are continuing.

We feel we have developed a solid scheme by which the FPS will be constructed, and our understanding of how it will be used continues to mature. We look forward to continuing on with the construction phase of the detector in the coming months.

A Appendices

A.1 Stress Analysis of Lead Absorber

We include on the following four pages the results from a stress analysis of the 6% antimony-doped lead absorber. We studied the larger (lower) piece of the lead in two configurations: in the first configuration (Figs. 32 and 33), the lead was held vertically, suspended at its two outermost points, and rotated in ϕ to the final position in which it will be installed. In the second (Figs. 34 and 35), it was laid on a flat surface – we felt it worthwhile to study this geometry, as it is possible we may have to work with the absorber briefly on a flat table of some kind. For each of these configurations, both the resulting stress (in psi) and deflection (in inches) are shown. The absorber was also pre-shaped to its final $\approx$ 100" bending radius for these studies as well.

We note for reference that the yield strength, or the elastic limit, is σ_y = 2,800 psi. In both cases, the resulting stress on the lead will not cause any difficulties, and the deflections are small – within $\approx$ 8 mils. We note that the stresses will be spread out over the ribs and, to a lesser extent, the outer rings, in the final detector, further sharing the potential load on any of the support elements.

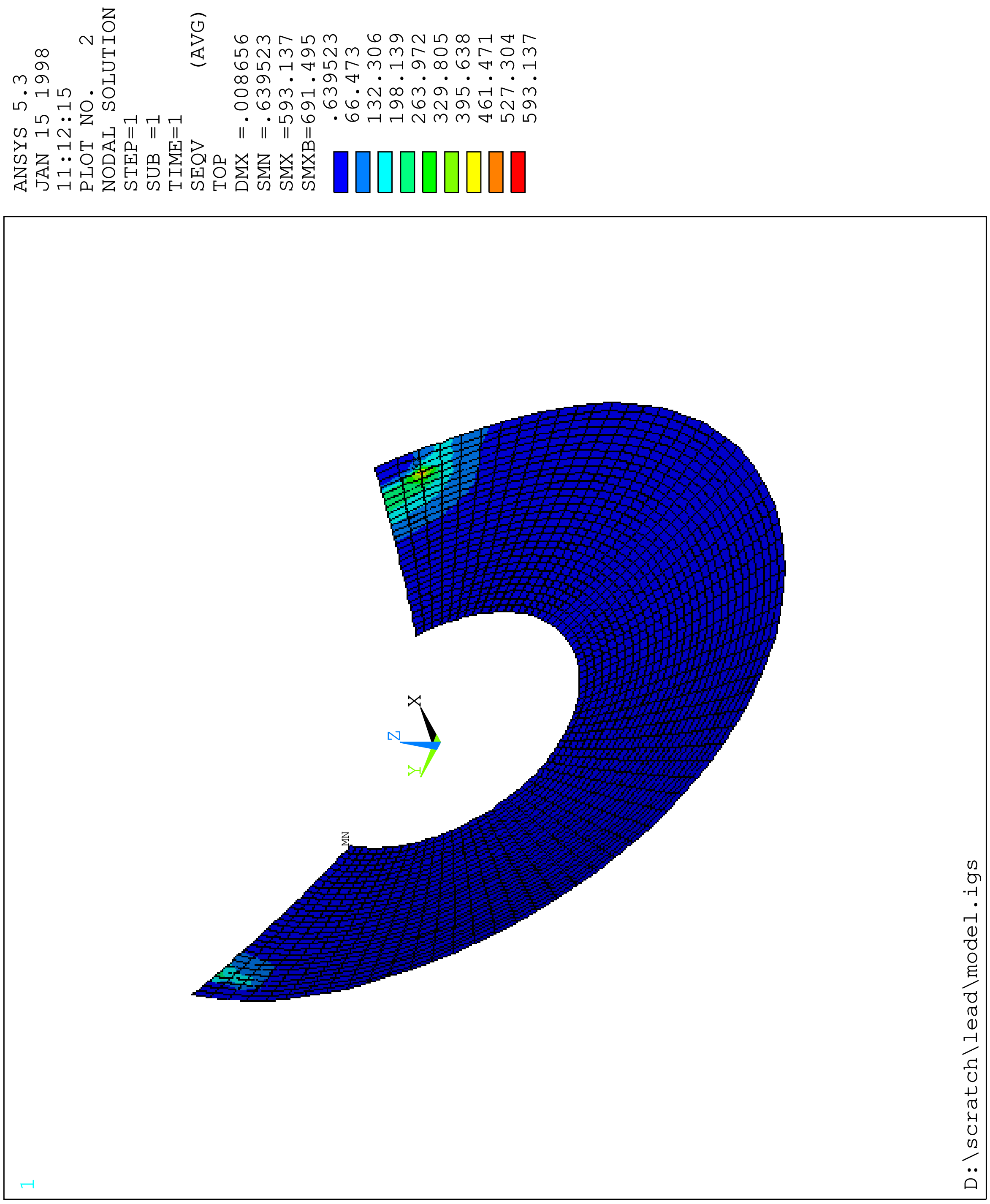

Figure 32: Stresses on the lower half of the lead absorber when vertically suspended at its two outermost points and rotated by 11.25° degrees from the vertical, as in the final detector.

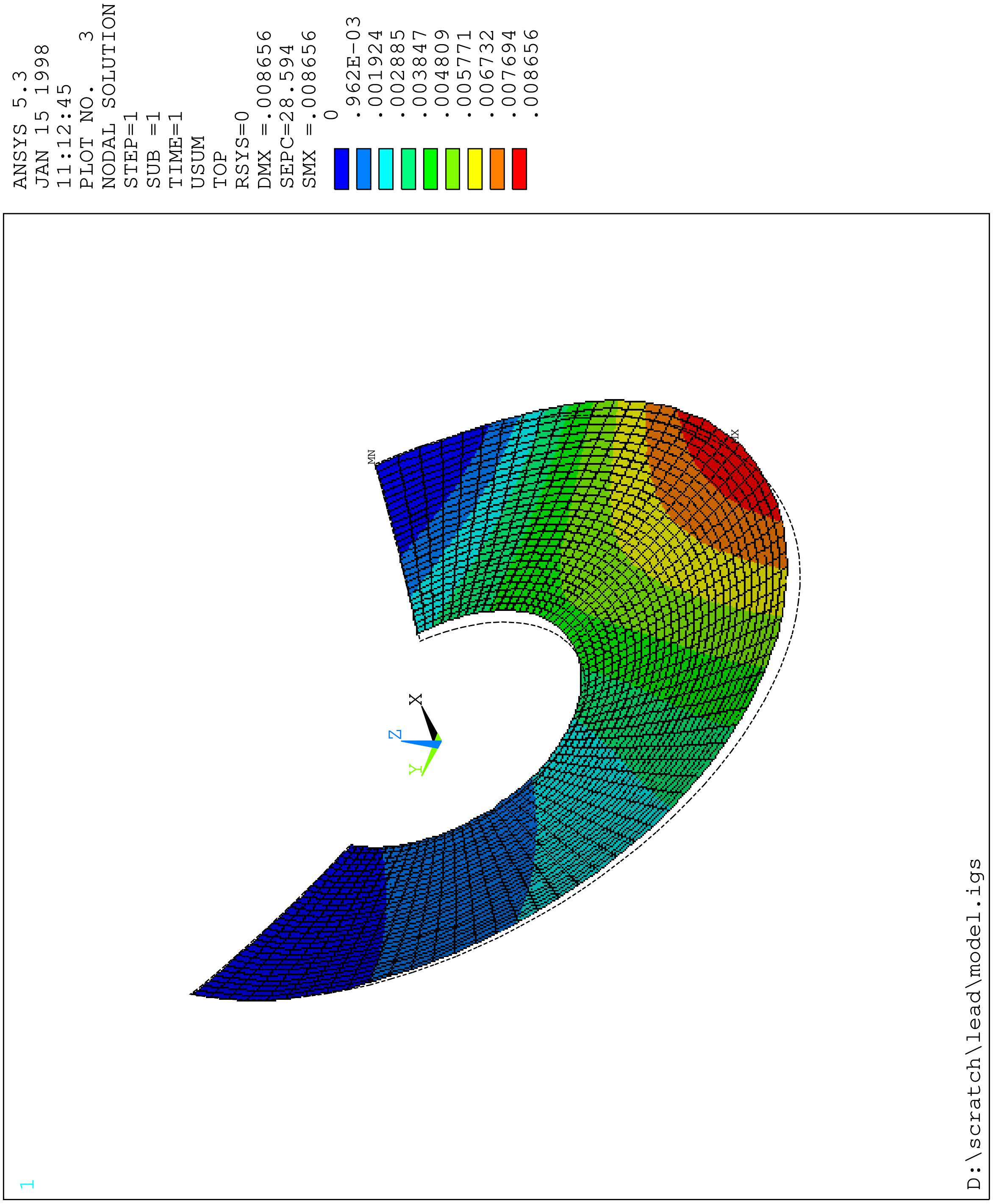

Figure 33: Same as Fig. 32, but showing the deflections in the structure.

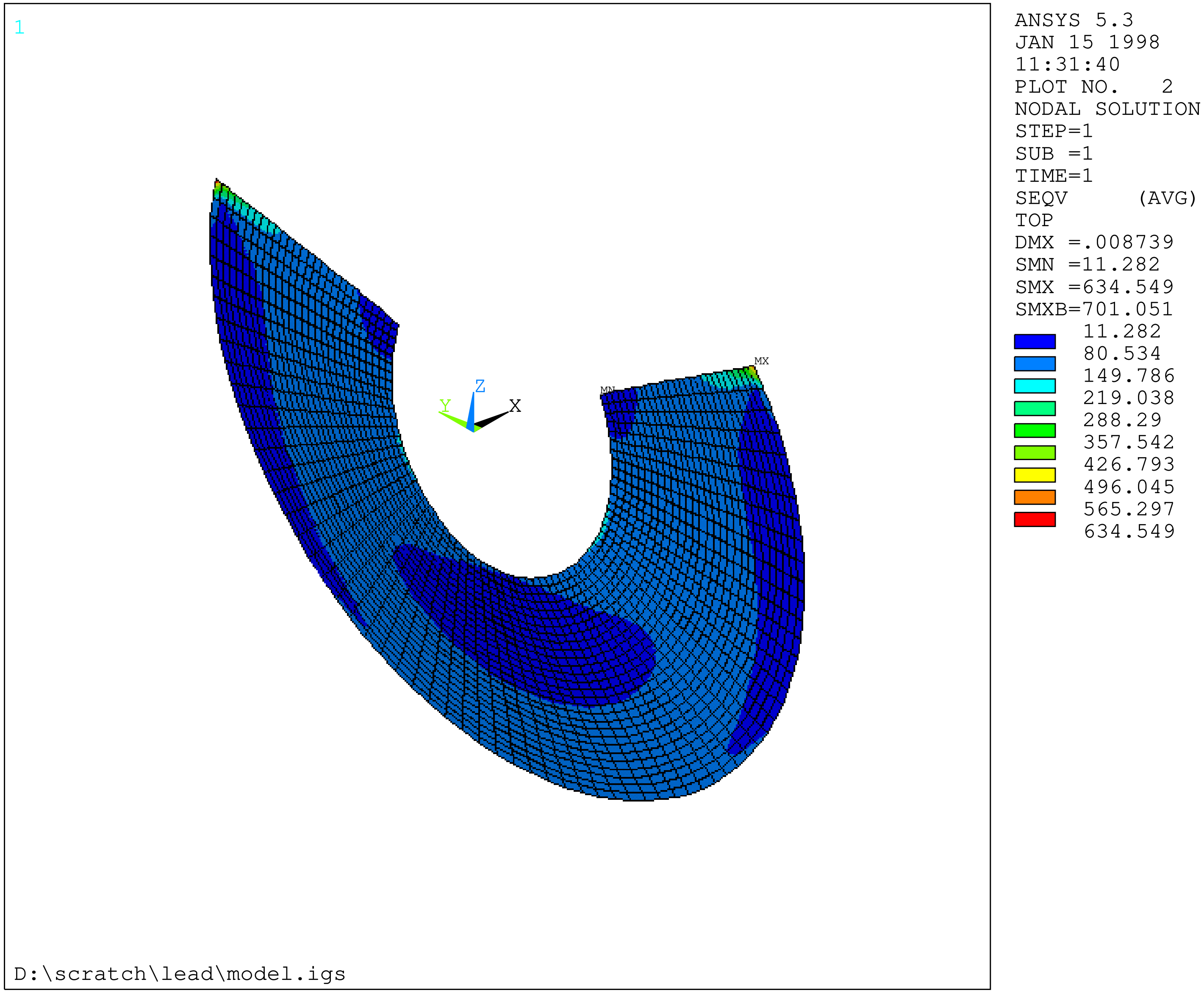

Figure 34: Stresses on the lower half of the lead absorber when lying on a flat surface.

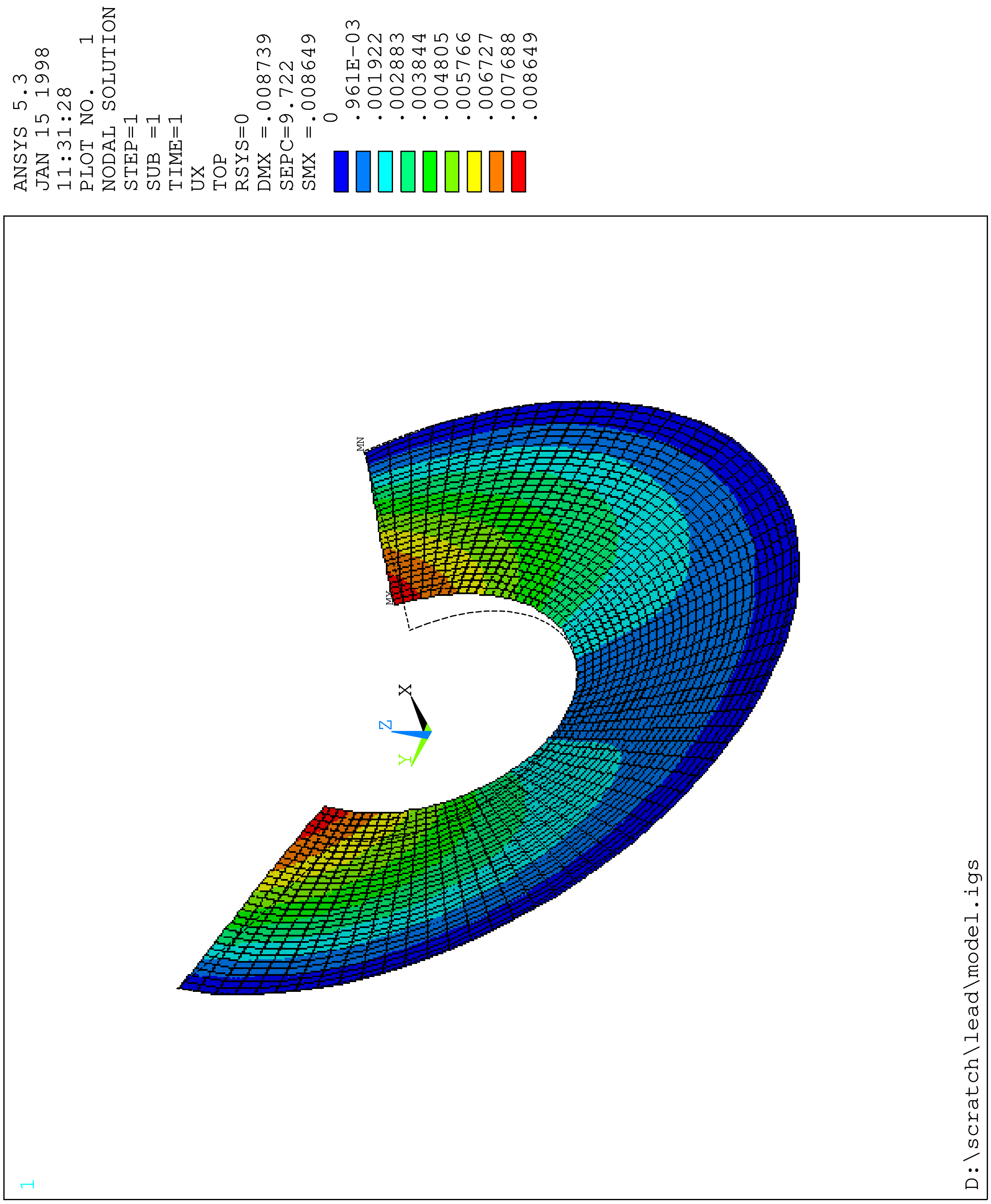

Figure 35: Same as Fig. 34, but showing the deflections in the structure.

A.2 Summer 1997 FPS Test Beam Results

We include below some plots resulting from the analysis of the beam test of the prototype at Fermilab from June through September, 1997. We note that a full DØ Note describing this work has recently been released [23]. Comparisons between data and GEANT Monte Carlo of 50 and 70 GeV electron shower profiles are shown in Fig. 36 and Fig. 37, respectively. The plots for each are normalized by the corresponding MIP signal, as measured in the forward layers of the detector; the spectra are therefore plotted in units of MIPs. Since the normalization is done independently for the data and the Monte Carlo, the plots are a fair comparison of the shower shapes in each. The signals for the u and v module layers are plotted independently.

The integrated shower profile at each energy are shown in Fig. 38 and Fig. 39. In these plots, the first bin represents the fraction of the signal seen in the central strip, the second represents the fraction of the signal in the central strip plus that in its two adjacent neighbors, and so on. In general, the data is a bit broader than the Monte Carlo, but the Monte Carlo models the data reasonably well.

The MIP distribution for 125 GeV pions is shown in Fig. 40. This plot represents an event-by-event sum of the two adjacent strips in the u layer of the FPS that have been traversed by the minimum ionizing pion. The characteristic Landau shape of the pulse height distribution is evident.

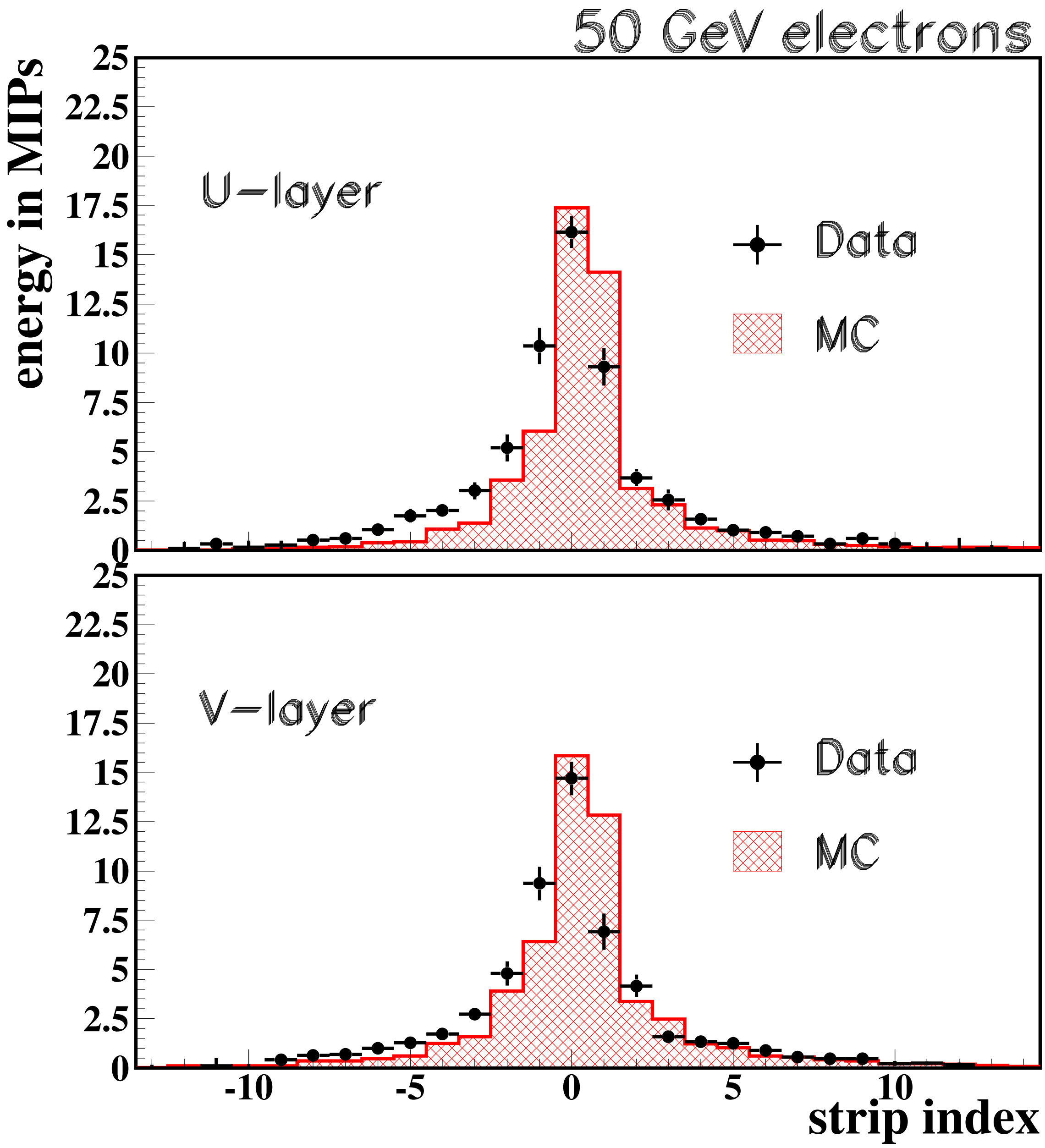

Figure 36: Comparison between data and Monte Carlo of the shower profile of 50 GeV electrons in the FPS for both the u and the v module layers. The spectra are plotted in units of MIPs (see the text). Data were taken during the beam test at Fermilab in the summer of 1997.

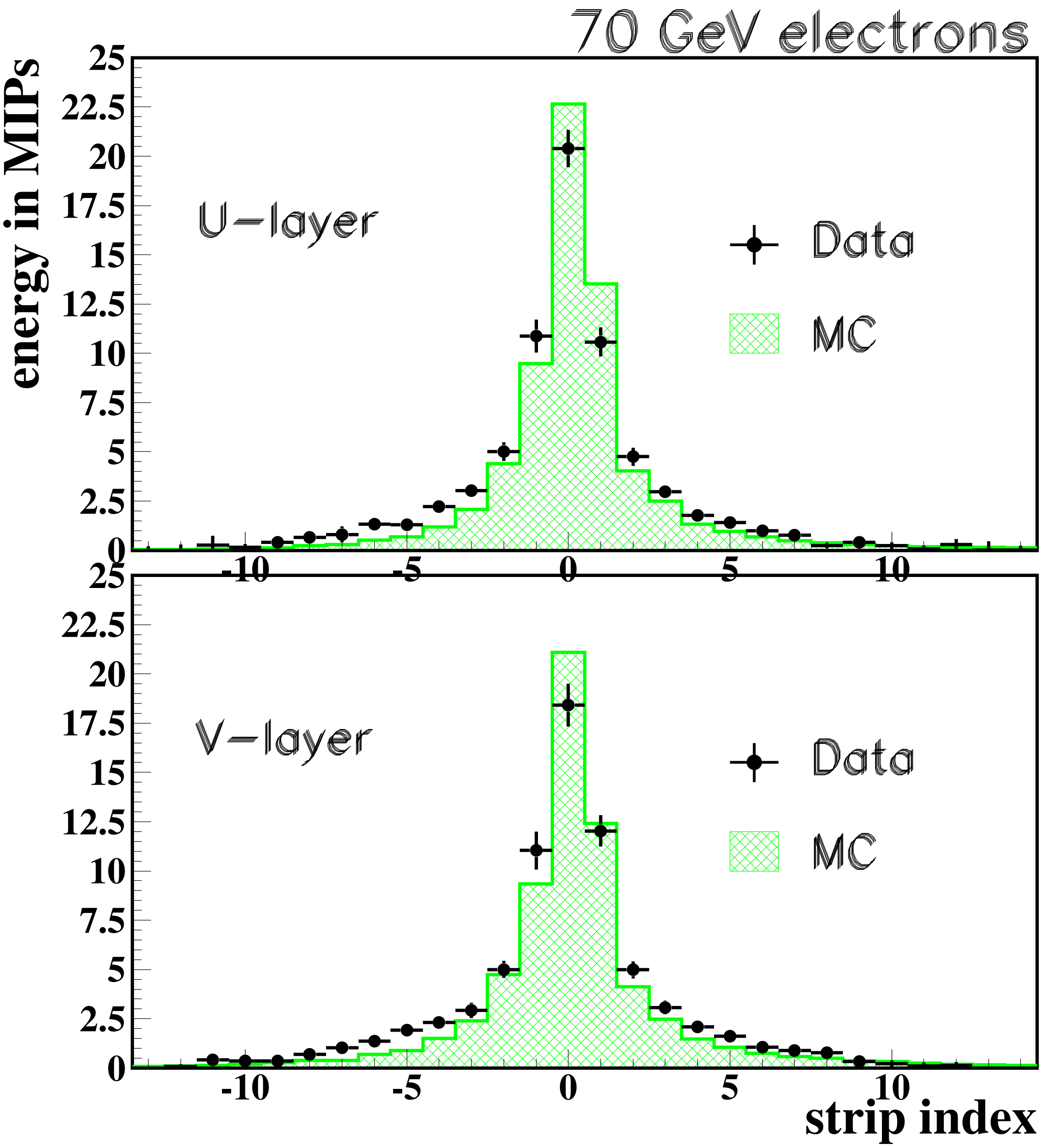

Figure 37: Same as Fig. 36, but for 70 GeV electrons.

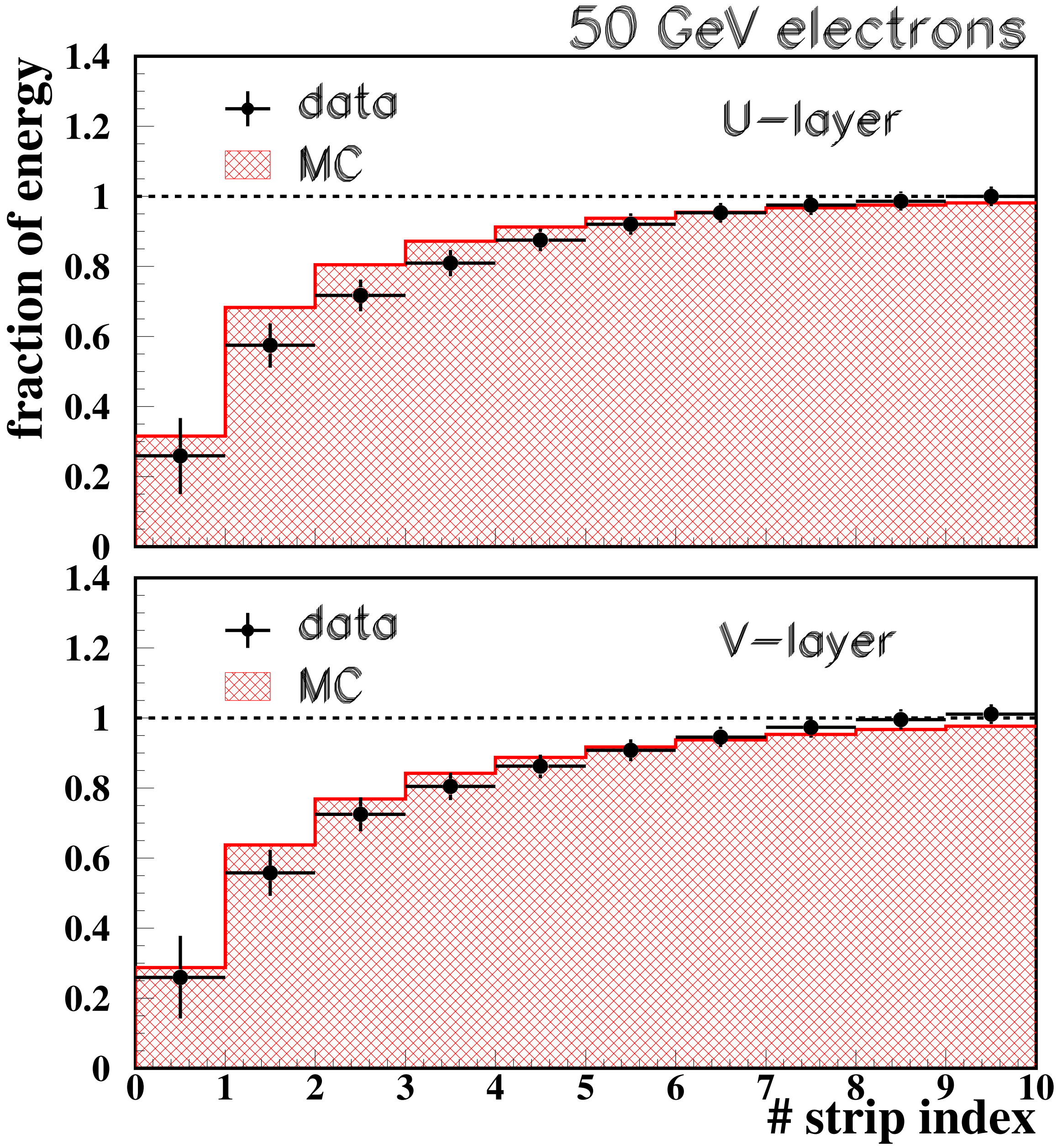

Figure 38: Integrated shower profile for both data and Monte Carlo for 50 GeV electrons. Description of the plots is in the text.

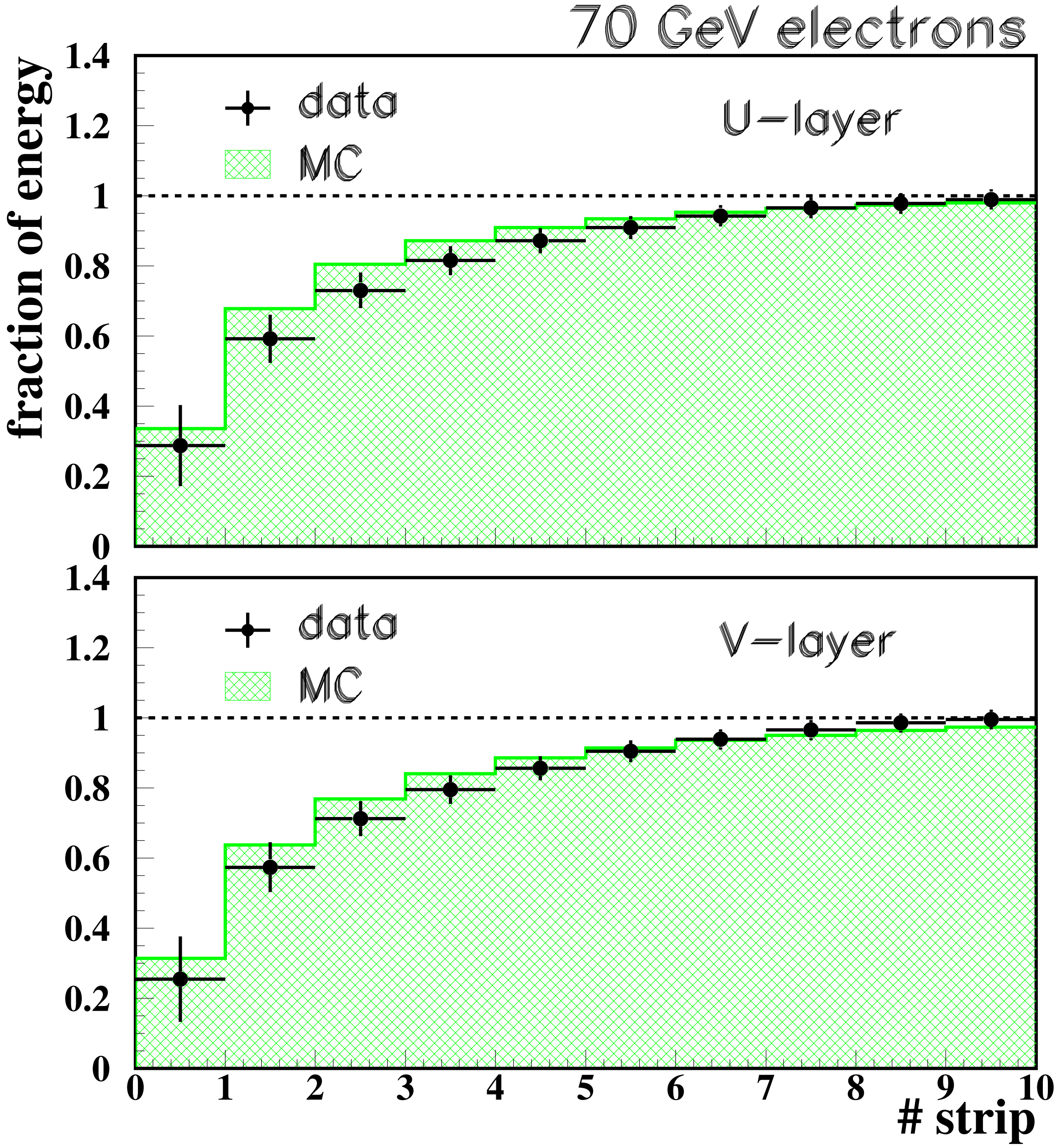

Figure 39: Same as Fig. 38, but for 70 GeV electrons.

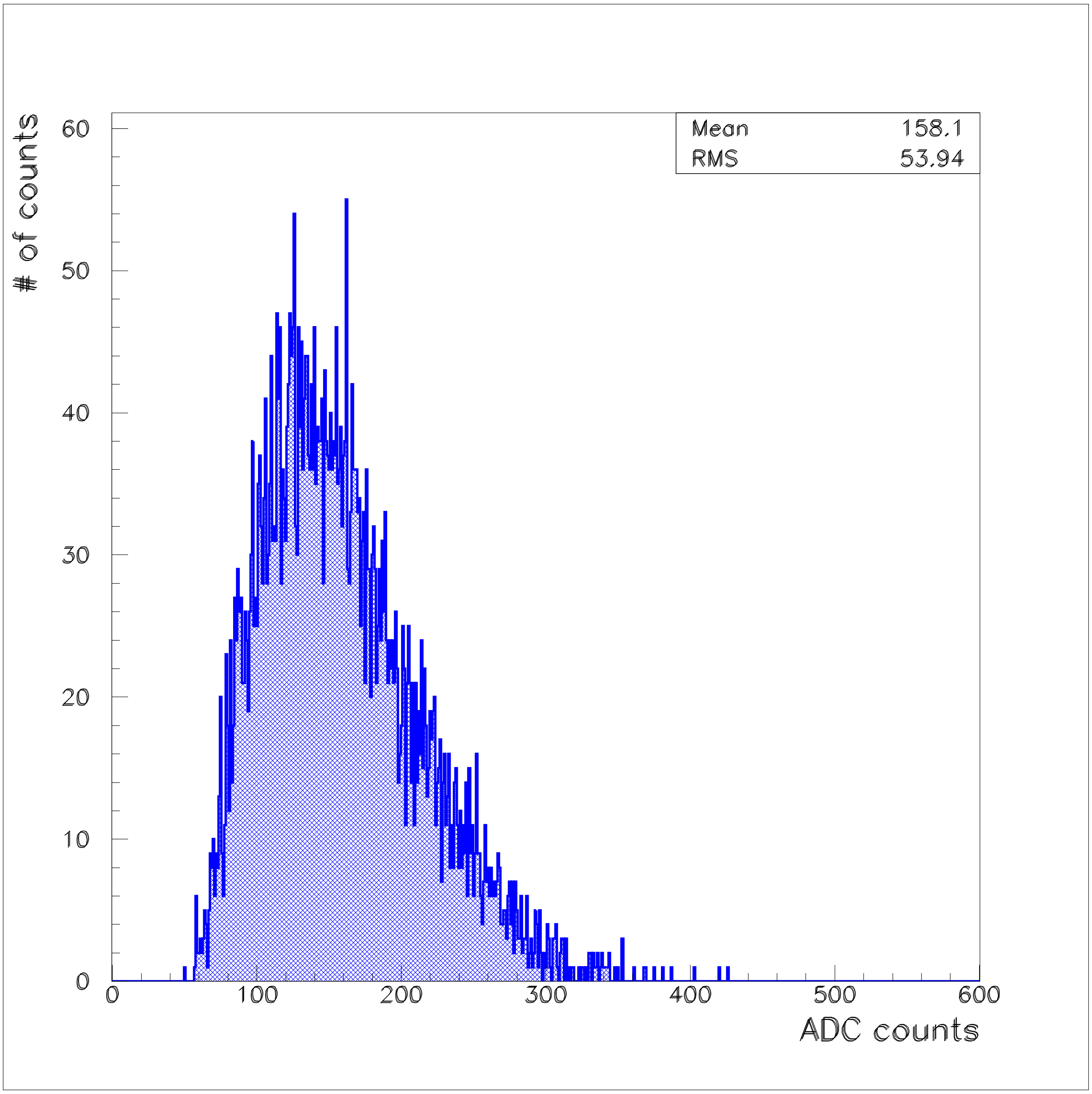

Figure 40: The MIP spectrum for 125 GeV pions traversing the u layer of the forward FPS module. The spectrum is an event-by-event sum of the two adjacent hit strips.

References

[1] R. W. Brown et al., Phys. Rev. **D20**, 1164 (1979); K. O. Michaelian et al., Phys. Rev. Lett. **43**, 746 (1979).

[2] G. Landsberg, DØ note 2709.

[3] M. Adams *et al.*, "A Detailed Study of Plastic Scintillating Strips with Axial Wavelength Shifting Fiber and VLPC Readout", Nucl. Instrum. Methods **A366**, 263 (1995).

[4] M. Adams *et al.*, "A New Detector Technique Using Triangular Scintillating Strips to Measure the Position of Minimum Ionizing Particles", Nucl. Instrum. Methods **A378**, 131 (1996).

[5] DØ Collaboration, "The DØ Upgrade: The Detector and Its Physics", July 30, 1996.

[6] DØ Collaboration, "The DØ Upgrade: Forward Preshower, Muon System and Level 2 Trigger", DØ note 2894.

[7] S. Margulies and M. Chung, "Development of a multichannel fiber-to-fiber connector for the DØ upgrade tracker", Photoelectonic Detectors, Cameras, and Systems, eds. C.B. Johnson and E.J. Fenyves, Proc. SPIE 2551, pp. 10-16, 1995. M. Chung and S. Margulies, "Development of a multichannel fiber-to-fiber connector for the DØ upgrade tracker", 1995 IEEE Nuclear Science Symposium, Vol. 43, No. 3, June 1996.

[8] M. Adams *et al.*, "Design Report of the Central Preshower Detector for the DØ Upgrade", DØ note 3014, Jan. 15, 1996.

[9] The diamond fly-cut tool for fibers and connectors was designed and made in the Physics Department, Fermilab, Batavia, IL 60510.

[10] General Electric VISC-600M; Polydimethylsiloxane, product of GE Silicones, General Electric Company, Waterford, NY 12188.

[11] Light transmission in connector channels was measured by the DØ UIC group using a green light-emitting diode and a photodiode. Complete description of the set-up appears in Ref. [7].

[12] Kuraray International, 200 Park Ave., New York, NY 10166, USA. Tel. +1 (212) 986-2230.

[13] Nichia America Corp., 1006 New Holland Ave., Lancaster, PA 17601, USA. Tel. +1 (717) 399-2119. The current blue LEDs that are being used are Middle-Type (30 deg.) 3 mm lens-diameter NLSB310.

[14] S. Margulies and M. Chung, "Fabrication and Testing of clear lightguide fiber bundles for the DØ prototype fiber tracker cosmic-ray test", Scintillating Fiber Technology and Applications II, ed. E.J. Fenyves, Proc. SPIE 2281, pp. 26-34, 1994.

[15] Zippertubing Co., 13000 S. Broadway, Los Angeles, CA 90061.

[16] National Instruments Corp., 6504 Bridge Point Parkway, Austin, TX 78730, USA. Tel. +1 (512) 794-0100.

[17] A. Bross, private communication.

[18] J. Qian, private communication.

[19] D. Adams *et al.*,, FERMILAB-Conf-94/318-E; M. Atac *et al.*, *Nucl. Instr. and Meth.* **A314** (1992) 56; M.D. Petroff and M.G. Stapelblock, *IEEE Trans. Nucl. Sci.* **NS-36** (1989) 158; M.D. Petroff and M. Atac, *ibid.*, p. 163.

[20] "Characterization of the SVXIIb Chip", B. Abbott *et al.*, DØ Note 2842 (February, 1996).

[21] "Timing Resolution and Linearity Measurements for a Scintillating Fiber Detector Instrumented with VLPCs", A. Bross *et al.*, *Nucl. Instr. and Meth.*, to be published.

[22] "ATLAS Tile Calorimeter Technical Design Report", ATLAS/Tile Calorimeter Collaboration, CERN/LHCC/96-42, December 15, 1996. "Construction and Performance of an Iron-Scintillator Hadron Calorimeter with Longitudinal Tile COnfiguration", RD-34 Collaboration, CERN/LHCC 95-44, August 16, 1995.

[23] "Results from a Beam Test of the Forward Preshower Detector for the DØ Upgrade", M. Bhattacharjee and A. Lucotte, DØ Internal Note #3398, January, 1998.

[24] S. Margulies and M. Chung, "Fabrication and Testing of Clear Lightguide Fiber Bundles for the DØ Prototype Fiber Tracker Cosmic Ray Test", in *Scintillating Fiber Technology and Applications II*, E.J. Fenyves, ed., *Proc. SPIE* 2551, pp. 2-9 (1995).

[25] S. Margulies and M. Chung, "Estimation of Radiation Doses in the DØ Upgrade Scintillating Fiber Tracker and Central Preshower Counter", DØ Note 2394 (1994).

[26] Bicron Corporation, 12345 Kinsman Road, Newbury, OH, 44065-9677, USA. Tel. +1 (216) 564-2251.

[27] "NFS Proposal for a Muon Level-2 Preprocessor for D0" M. Fortner, D0 note in preparation.

[28] D. Owen, private communication.